



UNIVERSITAT<sup>DE</sup>  
BARCELONA

## Micromotors for Environmental Applications

Jemish Parmar



Aquesta tesi doctoral està subjecta a la llicència **Reconeixement 4.0. Espanya de Creative Commons.**

Esta tesis doctoral está sujeta a la licencia **Reconocimiento 4.0. España de Creative Commons.**

This doctoral thesis is licensed under the **Creative Commons Attribution 4.0. Spain License.**



UNIVERSITAT DE  
BARCELONA

Doctoral Thesis

**Micromotors for Environmental  
Applications**

Jemish Parmar

---

# Micromotors for Environmental Applications

Programa de doctorat en Nanociències

Autor: **Jemish Parmar**

Director: **Prof. Dr. Samuel Sánchez Ordóñez**

Tutor: **Prof. Dr. Josep Samitier Martí**



UNIVERSITAT DE  
BARCELONA

---



The research described in this thesis was carried out in the group ‘Smart nano-bio-devices’ at the Max Plank Institute for Intelligent Systems in Stuttgart, Germany, and at the Institute for Bioengineering of Catalonia, Barcelona, Spain.

---

# CONTENTS

CONTENTS.....	4
LIST OF ABBREVIATIONS .....	8
ABSTRACT.....	10
CHAPTER 1.....	14
INTRODUCTION .....	14
1.1. Water pollution .....	15
1.2. Wastewater treatment and Nanotechnology .....	16
1.3. Micromotors and motion at microscale .....	19
1.4. Mechanisms of propulsion for micromotors.....	23
1.4.1. Self-powered micromotors .....	24
1.4.2. Externally powered micromotors.....	27
1.5. Bubble propelled micromotors .....	31
1.5.1. Fabrication of bubble propelled micromotors .....	31
1.5.2. Mechanism of bubble propulsion .....	37
1.6. State of the art of micromotors in environmental field.....	40
1.7. Enhanced mixing by micromotors .....	46
CHAPTER 2.....	48
ORGANIC REMOVAL USING MICROMOTORS .....	48
2.1. Introduction.....	49
2.2. Results and discussion .....	50
2.3. Conclusions.....	64
2.4. Experimental section.....	65
2.4.1. Fabrication of the micromotors.....	65
2.4.2. Size effect and reusability experiments .....	66
2.4.3. Continuous swimming experiment and video recording .....	67
2.4.4. Surface characterization.....	67
2.4.5. Mechanical properties.....	68

CHAPTER 3.....	69
HEAVY METAL REMOVAL USING MICROMOTORS.....	69
3.1. Introduction.....	70
3.2. Results and discussions.....	71
3.3. Conclusions.....	81
3.3. Experimental methods .....	82
3.3.1. Materials and reagents .....	82
3.3.2. Fabrication of graphene oxide-based multilayer micromotors ...	82
3.3.3. Equipment used for the experiments. ....	83
CHAPTER 4.....	86
BACTERIAL DISINFECTION AND REMOVAL USING MICROMOTORS .....	86
4.1. Introduction.....	87
4.2. Results and discussion .....	88
4.3. Conclusions.....	99
4.4. Experimental methods .....	100
4.4.1. Materials and reagents.....	100
4.4.2. Equipment.....	100
4.4.3. Synthesis of AgNPs .....	101
4.4.4. Synthesis of Janus microparticles .....	101
4.4.5. Bacteria Culture .....	102
4.4.5. Experimental procedures .....	103
CHAPTER 5.....	105
MULTIFUNCTIONAL MICROMOTORS AND SCALABLE SYNTHESIS .....	105
5.1. Multifunctional photocatalytic micromotors .....	106
5.1.1. Introduction.....	106
5.1.2. Results and Discussions.....	107
5.1.3. Conclusions.....	115
5.1.4. Experimental methods .....	115
5.2. Template free synthesis of micromotors.....	120
5.2.1. Introduction.....	120
5.2.2. Results and discussion .....	121

5.2.3. Conclusions.....	129
5.2.4. Experimental methods .....	129
CHAPTER 6.....	132
CONCLUSIONS AND FINAL REMARKS.....	132
References.....	135
Resumen en español.....	148



## LIST OF ABBREVIATIONS

3,4-Ethylenedioxythiophene	EDOT
Advanced oxidative processes	AOPs
Bis-4 nitrophenyl phosphate	b-NPP
Cobalt ferrite micromotors	CFO micromotors
Diethyl chlorophosphate	DCP
Dimethyl sulfoxide	DMSO
Electron energy loss spectroscopy	EELS
Energy dispersive X-ray spectroscopy	EDX
Ethyl-paraoxon	EP
Fe <sub>2</sub> O <sub>3</sub> /SiO <sub>2</sub> -MnO <sub>2</sub> micromotors	FeSiMnOx micromotors
SiO <sub>2</sub> -MnO <sub>2</sub> micromotors	SiMnOx micromotors
Gold nanowires	AuNWs
Graphene oxide based micromotors	GOx micromotors
Inductively coupled plasma spectrometry	ICP-OES.
Iron/Platinum micromotors	Fe/Pt micromotors
Membrane bioreactors	MBR
Metal–organic frameworks	MOF
Methyl-paraoxon	MP
Molecular beam epitaxy	MBE
Physical vapor deposition	PVD
Poly(3,4-ethylenedioxythiophene)	PEDOT

## List of abbreviations

Polycarbonate template	PC template
Polypyrrole	PPy
Reynolds number	Re
Rhodamine 6G	R6G
Rhodamine B	RB
Scanning electron microscopy	SEM
Self-assembly monolayers	SAM
Silver nanoparticles	AgNPs
Sodium dodecyl sulfate	SDS
Tetracycline	TC
Transmission electron microscope	TEM
X-ray diffraction	XRD
X-ray photoelectron spectroscopy	XPS

## ABSTRACT

Scarce supply of clean water and rising water pollution are key global challenges for water sustainability. Much of the wastewater generated by human agricultural and industrial activity is left untreated. Nanotechnological materials and systems have emerged as new tools for improving the efficiency of water treatment. Among those, self-propelled micromotors have shown several advantageous characteristics. Micromotors are autonomously propelled systems which either use chemical energy present in their environment or are propelled via external force fields. Diverse designs, materials composition and mechanisms of propulsion are reported for micromotors found in the literature. Among them, bubble-propelled micromotors, which move due to the generation and release of gas bubbles from their surface, are the main type of motors used for water remediation applications. In addition to the motion in fluids, the bubbles generated by the motors, also contribute with additional mixing of the fluid and enhance the mass transfer between active material and pollutant at the microscale. Micro-mixing has an important influence on the apparent kinetics of fast chemical reactions, in which the velocity of the reaction is often limited by diffusion. Additionally, the structure of micromotors can be modified to target a wide variety of pollutants, almost on demand. The micromotors that we synthesized during the research work for this thesis can remove organic and heavy metal pollutants, as well as exhibit bactericidal activity.

We studied Iron/Platinum (Fe/Pt) micromotors for their reusability, effect of sizes, swimming behaviors and catalytic properties. These micromotors were fabricated by spontaneous roll-up of iron and platinum nanomembranes, deposited on the pre-fabricated patterns of a photoresist substrate. The relaxation of internal strain present in the nanomembranes, upon etching of sacrificial layer, led to rolling-up of the membranes into tubular structures of micromotors. The iron layer present as the outer surface of these micromotors can degrade organic pollutants via Fenton-like reaction and the inner platinum layer acts as the engine decomposing hydrogen

peroxide to oxygen for bubble propulsion. We observed that Fe/Pt micromotors can swim continuously for hours, and can be stored for weeks before reuse, without sacrificing much of their activity. They can be easily extracted from the water after cleaning process because of their magnetic properties. The results of our experiments on the analysis of micromotors' surface, nanoindentation study and iron release suggested that Fe/Pt micromotors act as a heterogeneous catalyst due to in situ generated iron oxide species on the surface, without leaching high concentration of iron in the media.

We developed graphene oxide-based micromotors (GOx-micromotors) for heavy metal removal, consisting of nanosized multilayers of graphene oxide, nickel, and platinum. These micromotors can capture, transfer, and remove heavy metals (i.e. lead) from contaminated water. GOx-micromotors are synthesized by electrodepositions of electro-reducible graphene oxide, nickel and platinum layers in the polycarbonate porous templates. Tubular micromotors are obtained after dissolving porous polycarbonate template. The outer layer of graphene oxide captures lead on their surface, and the inner layer of platinum provides self-propulsion in hydrogen peroxide, while the middle layer of nickel enables external magnetic control of the micromotors. We observed that the mobile GOx-micromotors can remove lead 10 times more efficiently than non-motile GOx-micromotors, cleaning water from 1000 ppb down to below 50 ppb in less than 60 min. These micromotors can be recycled and reused after the recovery of the heavy metal from their surface by using acidic media for desorption of metal ions. We have demonstrated control of their motion and directionality in a proof of concept microfluidic system.

Silver nanoparticles (AgNPs) decorated Janus micromotors were designed for disinfection and remove of *Escherichia coli* (*E. coli*) bacteria from contaminated water. The Janus micromotors were synthesized by coating one side of the magnesium microsphere with iron and gold layers. The gold layer was subsequently decorated with AgNPs. Magnesium present in the micromotors functions as both,

the template for the spherical shape and propulsion source by producing hydrogen bubbles while in contact with water. The inner layer of iron provides functionality for the magnetic remote guidance, and an outer AgNP coated gold layer facilitates adhesion of bacteria and gives bactericidal properties to the micromotors. We observed that the AgNPs-coated Au cap of the micromotors shows dual capabilities, capturing bacteria and killing them. After the disinfection process, the micromotors can be collected along with the attached bacteria, leaving water with no biological contaminants.

In our efforts to develop multifunctional micromotors and scalable synthesis methods, we developed two types of micromotors. (i) Mesoporous silica-based micromotors with manganese dioxide ( $\text{MnO}_2$ ) layer on the inner surface and coated with  $\gamma\text{-Fe}_2\text{O}_3$  nanoparticles ( $\text{FeSiMnO}_x$  micromotors). These micromotors can remove both organic and heavy metal pollutants, and they are synthesized using only template-assisted chemical methods. The degradation of organic pollutants is accomplished due to Fenton-like and photocatalytic reactions catalyzed by  $\text{Fe}_2\text{O}_3$  nanoparticles and their propulsion is driven by  $\text{MnO}_2$  and partly  $\text{Fe}_2\text{O}_3$  nanoparticles that catalyze the decomposition hydrogen peroxide. These micromotors are one of the fastest micromotors reported using a non-noble catalyst for  $\text{H}_2\text{O}_2$  decomposition. (ii) Cobalt ferrite micromotors (CFO micromotors) synthesized by template-free chemical synthesis approach. They are made up of aggregated cobalt ferrite nanoparticles, which act as the catalyst for propulsion and for Fenton-like reactions. We qualitatively measured the generation of hydroxyl radicals by CFO micromotors and studied the effect of surfactants on the degradation efficiency of CFO micromotors.

We hope that such approach of synthesizing micromotors via relatively facile methods will push the use of micromotors towards commercially practical solutions for water treatment. Future efforts should be made towards further development of scalable synthesis methods and use of efficient and inexpensive materials in the structure of micromotors. Overall, our results show that the multifunctional self-

propelled micromotors have potential to become an effective tool for water remediation in future.

# CHAPTER 1. INTRODUCTION

## 1.1. Water pollution

Water scarcity is becoming one of the major global issues, since many people live in areas with low water availability and a few cities are running out of clean drinking water<sup>1</sup>. The situation is worsening due to deforestation, global warming and climate changes, leading to a rise in temperature and affecting the rainfall in many regions<sup>2</sup>. Apart from that, anthropogenic wastewater discharge is polluting the water bodies and threatening aquatic life, as well as human health. It is predicted that by 2030, half of the world population will live in areas with high water stress<sup>3</sup>.

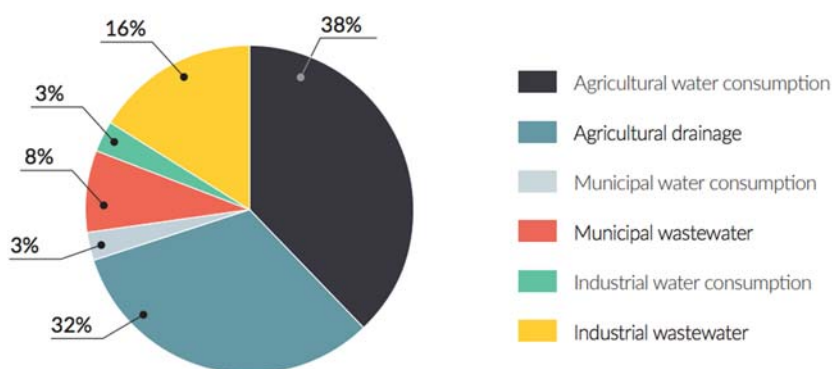


**Figure 1. Global consumption of freshwater, and wastewater production by major use sectors<sup>4</sup>.**

The demand for water is also expected to rise in the coming years, due to population increase and further development of society. Furthermore, drinking water accounts for only a small percentage of the current global demand of the freshwater, and the requirement of clean water for industrial and agricultural activities is much higher (Figure 1)<sup>4</sup>. The use of various chemicals and pesticides in industrial processes and agriculture sector severely contaminates the water and renders it toxic for overall living systems. Recent data compiled by UN suggests more than 95% of the freshwater ends up being wastewater and agricultural drainage (Figure 1). The reuse of the wasted water is crucial to create a sustainable cycle of water supply.

Development and use of efficient wastewater technology can help to alleviate the issues related to clean water scarcity and pollution.

## 1.2. Wastewater treatment and Nanotechnology

The centralized treatment of wastewater started in the late 19th century, in the United Kingdom, and was slowly adopted all over the world. Water treatment plants became essential for areas with a dense population, to provide clean drinking water to the entire population. However, these treatment plants require significant infrastructure and continuous maintenance, and for these reasons not all the wastewater generated all over the globe is treated before release. In fact, even in high-income countries, about 30% wastewater is released untreated, while in the low-income countries this number is higher than 90% (Figure 2)<sup>4</sup>.

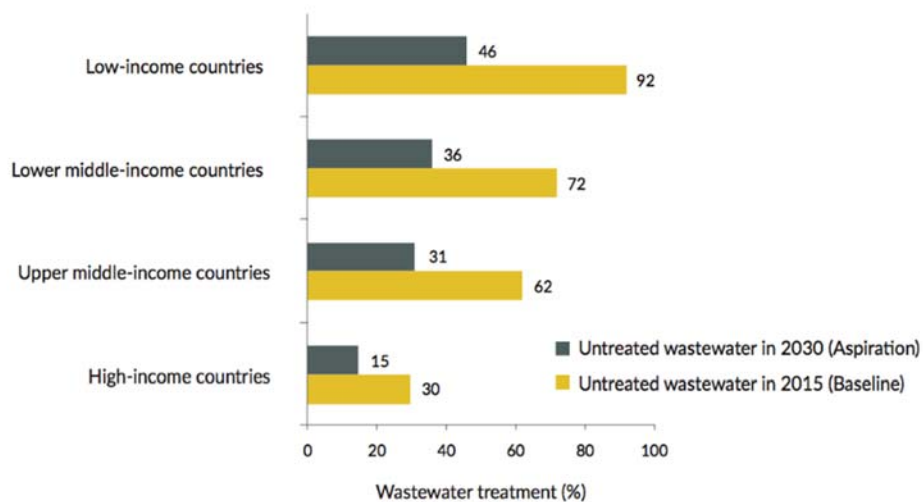


Figure 2. Percentage of wastewater left untreated in countries with different income categories<sup>4</sup>.

Untreated wastewater is comprised of municipal wastewater, which is relatively easy to treat, and industrial wastewater, which can be challenging depending on its origin and the type of contaminants it possesses. Industrial wastewater is often much more toxic compared to the municipal wastewater, due to the presence of the chemicals used in the industrial processes.

Municipal wastewater mostly contains organic contaminants of biological origin, which are treated in sewage treatment plants. In such plants, the water is treated by physical, biological and chemical methods. The physical methods, namely sedimentation and filtration, are used to remove large insoluble contaminants while biological methods are primarily focused on the removal of dissolved organic pollutants by bacteria. Biological treatments are generally based on activated sludge method, in which specially bred colonies of bacteria are fed on the pollutants, leading to the decomposition of chemicals, thus cleaning the water. Moreover, ultrafine pollutants present in wastewater are removed using chemical methods, which provoke precipitation and flocculation of the pollutants to facilitate their removal. Industrial wastewater is also treated using similar methods in the industrial wastewater treatment plants before it is released into the municipal wastewater sewage or water bodies. However, biological methods are often not enough to remove industrial pollutants, due to either low biodegradability or their toxicity to bacteria responsible for the cleaning processes<sup>5,6</sup>. Some of the pollutants, such as inorganic heavy metals require different techniques than organic pollutant removal. The advances in understanding the harmful effects of various organic and inorganic pollutants led regulatory authorities, especially in high-income countries, to make stringent guidelines for the quality of the wastewater that is released into water bodies. The need of environmental protection and overall societal health drove an increase in research and development of water treatment technologies.

In the past decades, various technologies have been developed for the improvement of water treatment. Other than advancement in the biological methods, such as the development of membrane bioreactors (MBR)<sup>7</sup>, non-biological methods such as advanced oxidative processes<sup>8</sup> and filtration technologies are being developed for the removal of refractory organic and inorganic pollutants. In the recent years, a major focus has been on the use of nanotechnology for the further enhancement of wastewater treatment technologies<sup>9,10</sup>. Special characteristics of nanomaterials, such as higher surface area and improved catalytic properties have been explored for the development of more effective systems<sup>11</sup>. The advanced oxidative processes (AOPs)

such as Fenton-like reactions and photocatalytic reactions can be made more efficient by using iron-based nanoparticles and nano-photocatalysts. Besides, some of the drawbacks of homogeneous catalysis can also be avoided using such heterogeneous catalysts designed using nanotechnology. These advanced oxidative processes produce highly oxidative radicals, that can decompose organic pollutants into less harmful products and even mineralize them into non-toxic compounds, such as carbon dioxide and water. While, Carbon-based nanomaterials such as carbon nanotubes, graphene, nanoscale metal oxides and nanofibers provide excellent properties, such as high surface area, for adsorption of various inorganic and organic pollutants. Insoluble fine organic pollutants, inorganic pollutants and biological contaminants, such as viruses and bacteria can also be removed from the wastewater by nanofiltration processes in which membranes with nano-pores can filter out the pollutants. Again, graphene, carbon nanotubes and other materials like nano-zeolite can be used for the development of such membranes. Instead of removing biological threats, a step further can be taken, and these can even be neutralized taking advantage of enhanced efficiency of nano-photocatalysts and bactericidal materials such as nano-silver.

Most of the efforts on the use of nanotechnology for water treatment are made towards the development of new materials or engineering combinations of nanomaterials to improve the catalytic, adsorbent or other relevant properties. Moreover, synthesis of nanomaterials with different shapes and sizes has also been studied for the effect on the removal of pollutants. However, apart from the intrinsic functional properties of the material, other parameters such as mass transfer and fluid mixing also play a key role in the kinetics of pollutants removal. In this doctoral thesis, I will discuss the results obtained by studying the removal of various pollutants when the functional nanomaterial responsible for the pollution is motile. To study the effect of motion along with the development of efficient nanomaterials for removal of organic, heavy metals and bacterial pollutants, micromotors have been developed as the self-propelled active materials. The self-propelled micro-nanomotors are newly developed nanotechnology-based devices

that can autonomously swim in a fluid media and provide several functions such as cleaning<sup>12</sup>, sensing<sup>13</sup>, concentrating<sup>14</sup> etc.

### 1.3. Micromotors and motion at microscale

The conceptual foundation of nanotechnology was based on the famous speech of Richard Feynman. He speculated in 1959 in his lecture “There’s Plenty of Room at the Bottom” that in future we would be able to manipulate matter at atomic and molecular levels, and even be able to make tiny machinery. During the last decade, his thought experiment of “swallowing a surgeon”, using tiny machines that can be swallowed and perform surgeries for treating diseases, became an inspiration for the development of nano-micromotors. Alongside, the sci-fi epic movie of 1966 “Fantastic Voyage” also explored this idea. In this movie, a crew and their ship were miniaturized and injected into the blood circulation of a patient, aiming at removing a blood clot and save the patient’s life. The movie itself also became an inspiration for scientists working on the development of micro-nanomotors.

The pioneering work on artificially fabricated nano machines was done by Stoddart and Feringa’s groups<sup>15,16</sup>. The molecular machines fabricated by these groups are stimulated externally, using stimuli such as heat or light. The stimuli induce conformational changes in the molecular structure, that produce mechanical movement. Stoddart’s group designed a molecular ring able to move along a molecular axel and with motion controllable by heat (**Figure 3A**). The molecular rotors designed by Feringa’s group were stimulated by UV light (**Figure 3B**). Feringa proposed that the rotary motion of these kind of molecular motors can be used to develop nanocars, capable to move forward due to the molecular engines (**Figure 3C**). Both scientists were awarded Nobel Prize of Chemistry in 2016, for their contribution in the development of the molecular machines.

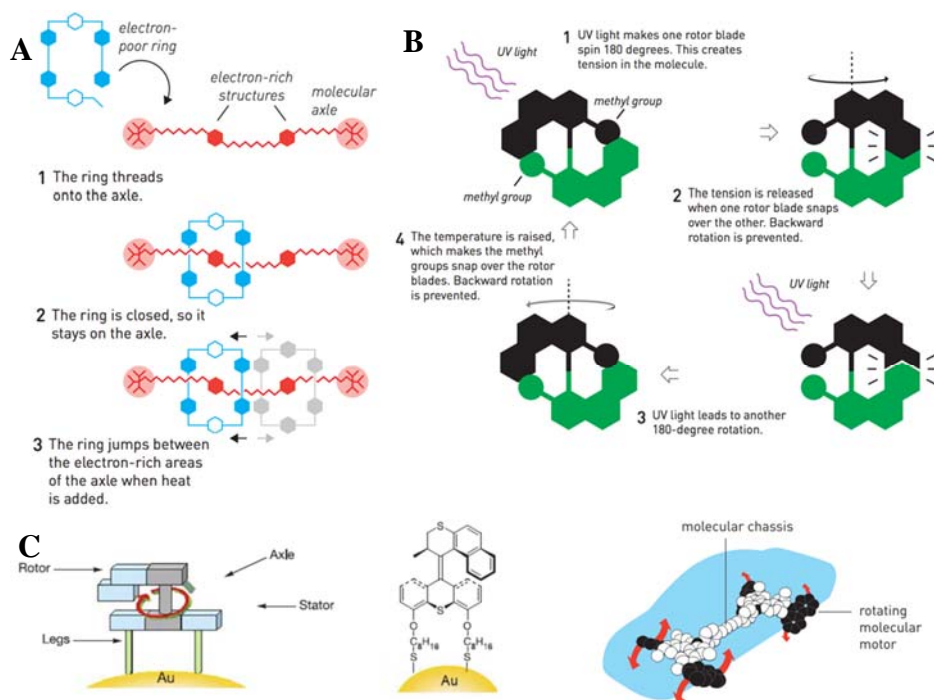


**Figure 3. Designs of molecular machines.** (A) Controlled movement of a molecular ring on a molecular chain. (B) One sided rotation of a UV light powered molecular system. (C) Rotary motion of a molecular motor on a molecular axel, such systems can functional as the engine and wheels of a nanocar. (Adapted from<sup>17</sup> Copyright © Johan Jarnestad/The Royal Swedish Academy of Sciences)

Despite the advances in nanotechnology and simple molecular machines developed, techniques to manipulate molecules and atoms according to Feynman vision are still lacking. The design of molecular machines and their functionality to manipulate other molecules or to perform predefined tasks is still difficult nevertheless nanoscale systems consisting of few billion atoms or molecules became widely accessible to fabricate and manipulate, because of the rapid advancement in nanofabrication methods of photolithography, physical vapor deposition, chemical vapor deposition, surface modification and chemistry of nanoparticles synthesis. In the last decade, these fabrication techniques have been used to develop wide variety of nano- and micromotors.

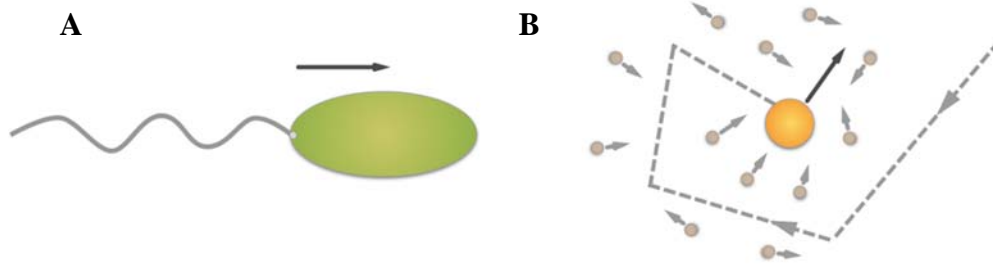


**Figure 4 Motion under the microscope.** (A) A bacterium swimming using flagella. (B) A microparticle experiencing Brownian motion due to collisions of solvent molecules.

However, swimming is a challenging task at the length scale at which micromotors operate. The first challenge is to overcome Brownian motion, a type of continuous random motion experienced by micro-and nanoscale particles in fluids. This motion behavior was initially observed by Robert Brown, a botanist, in the year 1827, while he was studying pollen in water under a microscope<sup>18</sup>. He initially thought that the particles were moving because they were alive, like bacteria (**Figure 4A**), but he observed similar motion with particles from dead plants, confirming that the movement was without influence of any living systems. Brownian motion is a manifestation of the collision of millions of solvent molecules with the particle (**Figure 4B**) due to their kinetic energy related to thermal fluctuations in the system. This mechanism was proposed by Einstein, and his theory also projected Brownian motion as the indirect proof of the physical existence of atoms and molecules, which were only theorized at that time. Physicist Jean Perrin experimentally confirmed Einstein's theory of Brownian motion, hence proving physical reality of these molecules and making it an important milestone in science.

To achieve significant directional motion, a particle must overcome the Brownian diffusion. Microorganisms, such as bacteria do it by using their cellular appendages, as flagella or cilia to swim. The physical principles describing the motion of microorganisms in fluids were described by E. M. Purcell in the year 1977<sup>19</sup>, where he explained the challenges of directional motion at the nanoscale. He used Reynolds number ( $Re$ ) to compare and describe challenges for the motion of

microorganisms with respect to motion of larger animals, like humans or whales swimming in water (Figure 5).

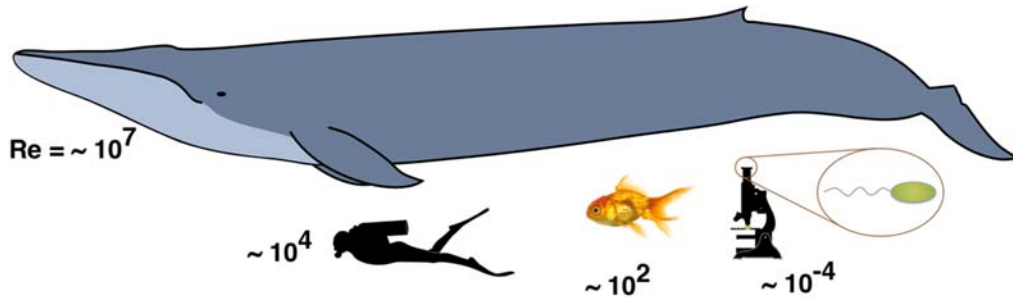
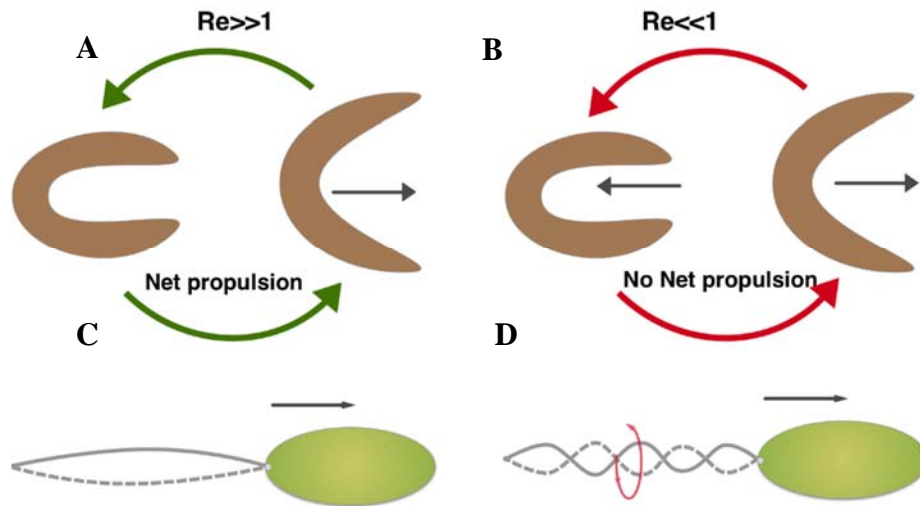


Figure 5. Comparative Reynolds number for different living things swimming in the water.

Reynolds number is a dimensionless number, defined as the ratio of inertial to viscous forces acting on an object in a fluid and is given by,

$$Re = \rho V \frac{l}{\mu} = \frac{\text{Inertial Forces}}{\text{Viscous Forces}} \quad (1)$$

where  $\rho$  is the density of the fluid,  $V$  and  $l$  are the velocities and the characteristic length of the object, respectively, while  $\mu$  is the viscosity of the fluid. Objects with very small size, such as bacteria swim at low Reynolds number where the viscous force dominates the inertial force. For example, a bacterium would stop moving forward within few microseconds after it stops using the appendages for swimming. It reaches the terminal velocity so quickly, that the distance it would travel in these microseconds time would be no more than the size of an atom. While for the bigger beings, such as humans or whales, inertial force can easily overcome the viscous force and a net momentum can be transferred to the fluid. Due to this momentum transfer at high Reynolds number (*i.e.*  $Re \gg 1$ ), non-continuous reciprocal work can be enough to achieve continuous forward motion. However, at the size scale of microorganisms, continuous non-reciprocal work is required for the continuous motion, since these systems quickly reach terminal velocity.



**Figure 6. Illustration of scallop theorem.** (A) A scallop can achieve net propulsion by reciprocal motion of opening and closing at high Reynolds number. (B) The same reciprocal motion of the scallop does not lead to net propulsion at low Reynolds number. At low Reynolds number propulsion can be achieved by (C) flexible non-reciprocal motion or by (D) corkscrew like motion.

Purcell explained this in the “Scallop Theorem”, by using an example of the motion of a scallop, which is invariant in time reversal and leads to the net propulsion since it operates at high Reynolds number. However, such reciprocal motion can only produce back and forth motion (Figure 6 A, B) at low Reynolds number. Bacteria generate continuous propulsion forces by corkscrew-like motion of their flagella or, by alternative ways such as flexible bending (Figure 6 C, D). The movement of biological cellular appendages is powered by cellular machineries developed over the course of many years of evolution.

#### 1.4. Mechanisms of propulsion for micromotors

To swim at low Reynolds number, artificial micromotors must continuously produce thrust to outrun Brownian diffusion, as the case of biological swimmers. Different mechanisms based on chemical reactions that harvest free energy present on the environment, or external stimuli have been investigated to continuously power these nano-micromotors, including mimicking the motion of bacterial

flagella. Important mechanisms that govern the propulsion of artificial nano-micromotors are briefly discussed here.

### 1.4.1. Self-powered micromotors

Self-powered micromotors convert chemical energy from their surrounding environment to kinetic energy, via chemical reactions<sup>20,21</sup>. The chemical decomposed in the reaction is commonly referred as “fuel” for the micromotors. The fuel is added in the aqueous media, where micromotors are to swim. The most common mechanisms are self-electrophoresis, self-diffusiophoresis and bubble propulsion.

#### Self-electrophoretic micromotors

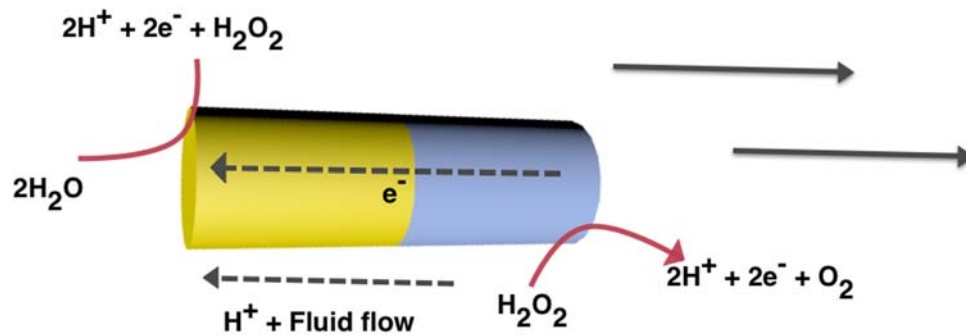
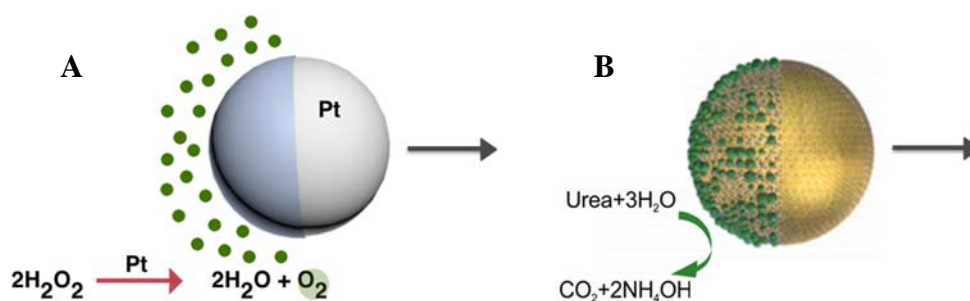


Figure 7. Mechanism of Self-electrophoretic bimetallic rod micromotors swimming in hydrogen peroxide fuel<sup>12</sup>.

Catalytic self-propelled micromotors were first reported by Paxton *et al.* in 2004<sup>22</sup>. These micromotors were made up of a stripped metal nanorod, fabricated by template assisted electrodeposition method. One side of this rod was made up of platinum and the other side was made of gold. An electrokinetic mechanism of their motion was later described by the same group<sup>23</sup>. This electrokinetics is induced due to catalytic reaction on the surface of nanorods when they were placed in solutions containing hydrogen peroxide ( $\text{H}_2\text{O}_2$ ). The platinum side of the nanorods catalytically oxidizes  $\text{H}_2\text{O}_2$  into protons, electrons and oxygen. The electrons

generated during this reaction travel to the other end (gold) of the rod, because of the conductive nature of both platinum and gold (**Figure 7**) and these electrons drive a reduction reaction. The redox reactions on opposite ends of the rod along with the flow of electrons create a self-generated electric field, which drives ion current from the platinum end to the gold end in the solution. The fluid flows generated along with the ion current propels the micromotors towards the direction of platinum end via electrophoretic motion.

### Self-diffusiophoretic micromotors



**Figure 8. Mechanism of a self-diffusiophoretic micromotors swimming in solutions containing fuel. (A)  $\text{H}_2\text{O}_2$ <sup>12</sup> and (B) urea<sup>24</sup> as fuel.**

Similarly, to self-electrophoretic micromotors, self-diffusiophoretic micromotors need to have a chemical reaction on their surface to achieve self-propulsion. However, this mechanism does not require the micromotors to be conductive. As suggested by the mechanism's name, this kind of micromotors is propelled by the diffusion of the solvent molecules and the chemical species produced during the reaction on the motors surface<sup>25</sup>. However, influence or ionic effects and even involvement of self-electrophoretic mechanism was suggested by some researchers<sup>26,27</sup>. The important condition for this kind micromotors is an asymmetry on the reaction that takes place on the surface of the motors. Typically, platinum half coated silica or polystyrene particles exhibit this mechanism of propulsion when placed in solutions containing  $\text{H}_2\text{O}_2$  (**Figure 8A**). Such particles are called Janus particles, inspired by the name of a two-faced Greek god. These micromotors are mostly fabricated either by physical vapor deposition (PVD) of platinum on a

monolayer of spherical particles made up non-conductive materials such as silica. In  $\text{H}_2\text{O}_2$  solutions, platinum decomposes  $\text{H}_2\text{O}_2$  into oxygen, electrons and protons. The protons and electrons further react with  $\text{H}_2\text{O}_2$  to produce water molecules, while the oxygen solute drives the self-diffusiophoresis reaction. The asymmetric chemical reaction on the surface of the particles causes a higher solute concentration on one of the sides, which quickly starts diffusing from the surface. This creates a flow field around the motors surface that propels the motors. Since all the product species generated during the reaction are neutral, this mechanism is considered neutral self-diffusiophoresis. Instead of inorganic metallic catalysts, enzymatic catalysts can also be used for propulsion. In the recent reports from Sanchez group, enzymatic reactions have been used to propel Janus micromotors using urea or glucose as fuel sources (Figure 8B)<sup>24</sup>. Same group recently reported that Janus structure is not necessary for propulsion of enzymatic micromotors, since other asymmetries originated from synthesis or functionalization methods, such as asymmetric distribution of enzymes can be enough for propulsion<sup>28</sup>. Nevertheless, in the case of enzymatic propulsion, the mechanism is not very clear, as propulsion can be due to a combination of multiple factors, such as enzyme conformational changes or diffusion of charged product species.

### Bubble propelled micromotors

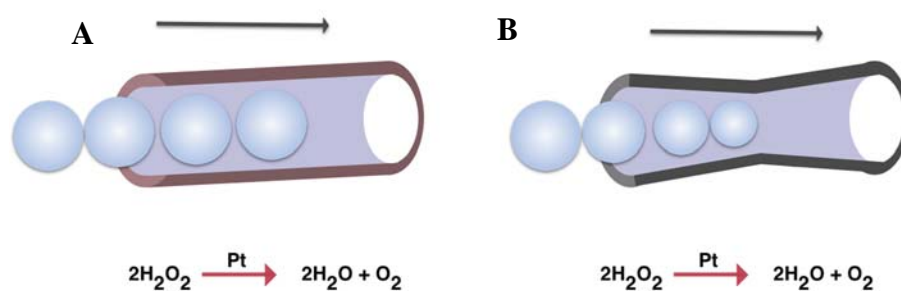


**Figure 9. Scheme of the designs of micromotors propelled by oxygen bubbles generated during the decomposition of  $\text{H}_2\text{O}_2$  fuel<sup>12</sup>.** (A) The micromotors are fabricated by roll-up technology and (B) the biconical micromotors are synthesized by template assisted electrochemical methods.

Bubble propelled micromotors typically contain a cavity where gas molecules generated during a chemical reaction can accumulate and grow into bubbles. The first report of bubble propelled micromotors was published by Mei *et al.* in 2008<sup>29</sup>. These micromotors were fabricated by rolling nanomembranes fabricated by lithography and PVD techniques into a tubular structure (**Figure 9A**). Such tubular micromotors typically contain a catalyst, such as platinum or silver, in the inner wall of the tubular structure. When this kind of micromotors are placed in solutions of H<sub>2</sub>O<sub>2</sub>, the inner platinum layer rapidly decomposes H<sub>2</sub>O<sub>2</sub> into water and oxygen gas. The quick release of the oxygen bubbles from one end of the micromotors leads to the propulsion the micromotors in the opposite direction of bubble release. Pumera's team presented a clean room free approach for fabrication of roll-up micromotors by using a TEM grid as a template, instead of a mask aligner typically used for photolithography<sup>30</sup>. Joseph Wang's team developed electrochemical-based template assisted deposition techniques to make tubular micromotors without the need of photolithography<sup>31</sup> (**Figure 9B**). The tubular structure of these motors facilitates bubble growth and migration which, in turn, facilitate propulsion. However, this structure is not an absolute requirement for bubble mechanism to work. Spherical shaped micromotors can also propel by this mechanism, if the rate of bubble generation and detachment is significant to generate a sufficient net force for propulsion<sup>32,33</sup>.

### 1.4.2. Externally powered micromotors

Externally propelled micromotors typically do not use chemical energy present in their environment, and mainly rely on an external energy source such as magnetic fields, light, ultrasound or electrical stimulation. Often, the speed and the direction of externally powered micromotors can be controlled using the same external actuation.

### Magnetically driven micromotors

Magnetic field is non-invasive and can penetrate biological tissues. This is a key motivation for the development of magnetically powered micromotors, since they can be propelled without the need of any chemical fuel or catalyst. The micromotors designed to be propelled in magnetic field have at least one magnetic material present in the structure. Upon applied magnetic field, the magnetic material aligns itself with the geometry of the applied field. The magnetically propelled micromotors are usually driven and controlled by using oscillating or rotating magnetic fields<sup>34</sup>.

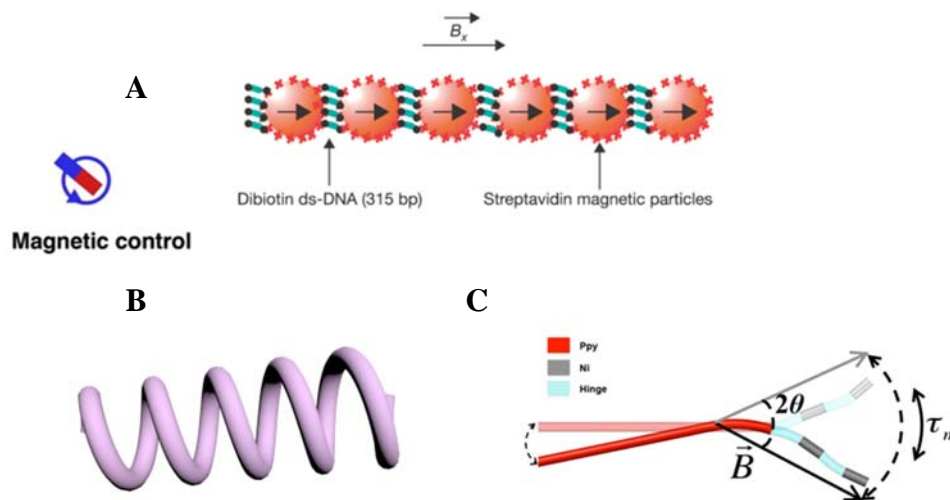


**Figure 10. Designs of magnetically actuated micromotors.** (A) Chain of magnetic beads propelled by oscillating magnetic field<sup>35</sup>. (B) Helical artificial flagella like micromotors propelled under rotating magnetic field<sup>36</sup>. (C) Flexible micromotors propelled by oscillatory magnetic field<sup>37</sup>.

The designs of magnetic micromotors are inspired by biological swimmers. In one of the earliest reports of magnetic propellers, Dreyfus *et al.* designed a flexible chain of magnetic microparticles attached by DNA linkers (Figure 10A)<sup>35</sup>. This flexible flagellum-like structure is propelled by an oscillating magnetic field. Oscillating magnetic field is normally used to drive micromotors with flexible or hinged structures with multiple segments. In the oscillating magnetic field, these structures exhibit non-reciprocal movement which can lead to swimming at low

Reynolds number<sup>37</sup> (Figure 10C). The pioneering work on the development of helical micromotors driven by rotation magnetic field was done by Nelson's group<sup>38</sup>, who designed micromotors inspired by the rotating helical flagella of the bacteria (Figure 10B). The helical shape of the micromotors does not move in homogeneous magnetic field, but upon applied rotating magnetic field, the helix orients with field leading to corkscrew-like movement. This flagella-like rotational movement makes it possible to propel helical micromotors at low Reynolds number.

### Light driven micromotors

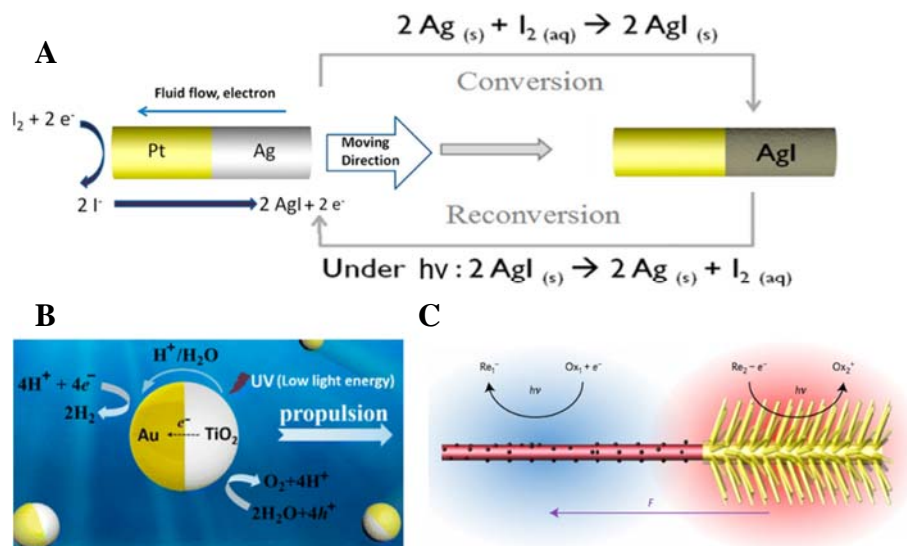


**Figure 11. Light harvesting micromotors designs.** (A) Self-electrophoretic Ag/Pt micromotors swimming in iodine containing media<sup>39</sup>. (B) Self-electrophoretic mobility of Au-TiO<sub>2</sub> microspheres in the presence of UV light<sup>40</sup>. (c) TiO<sub>2</sub>-silicone nanowire micromotors propelled by light mediated redox reaction<sup>41</sup>.

Light-propelled micromotors use light as the source of the energy, unlike catalytic self-propelled micromotors that catalyze the chemical fuel present in their environment without any input. The photocatalyst present on the structure of light-powered micromotors can generate electron-hole pairs to drive chemical reactions in their environment for self-propulsion<sup>42</sup>. The mechanism of the motion for the light-powered micromotors is similar to catalytic self-propelled micromotors. For example, Ag-Pt micromotors swimming in the presence of ultra violet (UV) light in

iodine containing media<sup>39</sup> (Figure 11A), Au-TiO<sub>2</sub> spherical micromotors<sup>40</sup> powered by UV light (Figure 11B), multi-wavelength responsive Au/Black-TiO<sub>2</sub> micromotors<sup>43</sup> and micro tree-like silicon nanowires<sup>41</sup> (Figure 11C) powered by visible are reported to propel via self-electrophoresis. Apart from that, surface plasmon resonance induced self-electrophoretic propulsion was also reported for nanocap-like motors by Sanchez group<sup>44</sup>. The nano tree-like structures developed by Dai *et al.* can even be programmed for positive or negative phototaxis, by surface modifications that control the zeta-potential.

#### Acoustic driven micromotors

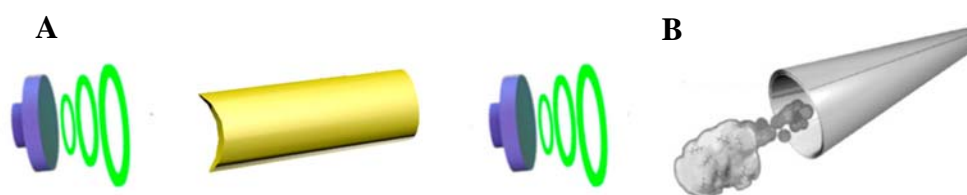


**Figure 12. Acoustically driven micromotors.** (A) Nanowire with a concave side propelled by localized generated pressure gradient under acoustic field<sup>45</sup>. (B) Tubular micromotors filled with perfluorocarbon propelled by quick vaporization of perfluorocarbon by ultrasound waves<sup>46</sup>.

Ultrasound waves are widely used for medical diagnostic purposes. The micromotors driven by acoustic fields are propelled by a localized pressure gradient acting asymmetrically on the micromotor. The micromotors are designed to generate these self-induced pressure gradients under the acoustic field. For example, in the first proof-of-concept of this propulsion mechanism, Mallouk's team fabricated nanowires by template assisted electrodeposition method, with concave shape on the one side of the wire (Figure 12A)<sup>45</sup>. The pressure generated at the concave side under the influence of external ultrasound waves leads to directional propulsion of the nanowires. Besides being used as source of propulsion, acoustic field has also been used to propel micromotors by activating on-board fuel. Wang's group designed tubular micromotors loaded with perfluorocarbon, which acts as the on-board fuel and quickly vaporizes upon exposure to ultrasound waves (Figure 12B)<sup>46</sup>. The release of vaporized perfluorocarbon propels the micromotors

extremely quickly. Apart from above mentioned propulsion mechanisms, thermophoresis<sup>47</sup>, electric field driven propulsion<sup>48</sup>, as well as bio-hybrid motors propelled by sperm<sup>49</sup> or bacteria<sup>50</sup> were also developed. Not all the mechanisms of motion and designs of micromotors reported in the literature are discussed here, since this thesis is focused on environmental applications of micromotors. However, readers can find further information on this topic in these reviews<sup>20,21,34,51</sup>.

### 1.5. Bubble propelled micromotors

Among above-mentioned mechanisms, bubble propulsion is a quite robust mechanism of propulsion. For example, the motion of self-diffusiophoretic micromotors and self-electrophoretic micromotors can severely be affected by the presence of salt or other ionic species in the media, while bubble propulsion is only affected if the catalyst or active material is inactivated by chemical species present in swimming media. It is important for the micromotors designed for environmental applications to have robust propulsion mechanism, due to the need for the micromotors to interact with pollutants and other chemicals present in the contaminated water. Bubble propelled micromotors are reported to swim in complex viscous media due to the high efficiency of bubble propulsion<sup>52,53</sup>, which is another useful swimming property. Apart from that, bubble propelled micromotors are one of fastest swimming micromotors. We exploited these attractive properties to design environmental micromotors for removal of various pollutants from water. The results presented in this thesis are mainly related to the development of bubble propelled micromotors, therefore I will focus on the discussion of main fabrication approaches and some basic theoretical principles behind the bubble propulsion in the following section.

#### 1.5.1. Fabrication of bubble propelled micromotors

##### Rolled up tubular micromotors

Prinz *et al.* and Schmidt *et al.* discovered that nanomembranes with intrinsic strain gradient can spontaneously roll-up into tubular shape upon strain relaxation<sup>54,55</sup>. Such gradient between layers of membranes can be developed in variety of fabrication techniques. Nanomembranes of varied materials are deposited on the patterned substrate by using microfabrication techniques such as sputtering, electron beam (e-beam) deposition or the molecular beam epitaxy (MBE) can have internal mechanical stress accumulated. The origin of stress in the thin film is mainly due to constraining imposed by the substrate on which the film is deposited. In the deposition methods like MBE, strain gradient can be controlled very precisely by choosing materials according to their lattice constants. The internal force between the atoms is a function of the interatomic distance, so when the thin film grows epitaxially on the substrate with smaller interatomic distance than equilibrium distance of the material, the film accumulates compressive strain and, if the interatomic distance is larger than the equilibrium distance, the film accumulates tensile strain<sup>54,55</sup>. Staking up of these nanomembranes on each other lead to the strain gradient which drives the spontaneous spatial changes in nanomembranes. The control of the strain gradient between layers is an important parameter for controlling the roll-up process. Depending on the gradient across the thickness of the membranes, they bend or wrinkle. For example, larger strain gradient leads to bending and smaller gradient leads to wrinkling of the membranes. Controlled bending of the membrane is used for their rolling up into tubes. The diameter of the tubes fabricated from the lattice mismatched epitaxial layers can be predicted analytically with a good agreement between the experimental radius and the calculated theoretical radius<sup>56</sup>. Roll-up nanotubes fabricated from strained heteroepitaxial nanomembranes with very small diameter were first reported for the fabrication of nanomotors.

However, MBE method is not always a suitable technique, especially for the fabrication of metallic and dielectric or hybrid tubes. Thin films of metal and dielectric materials are mostly deposited by sputtering, e-beam or the thermal evaporation methods<sup>57</sup>. The growth of such thin film is non-epitaxial and

amorphous or polycrystalline, but there is always inherent strain present in the thin film deposited by these non-epitaxial methods<sup>58</sup>. That strain is produced due to the growth kinetic process itself and can originate from various mechanisms, such as stress at the grain boundary, thermal expansion coefficient between films, void regions and phase transformation. The deposition parameters, such as deposition pressure, the temperature of the substrate and deposition geometry, can greatly influence the amount of strain generated due to the wide range of mechanisms involved in the process<sup>59</sup>. The strain gradient in the non-epitaxial film is not as predictable as the epitaxial film although it can be controlled by the evaporation rate of the material and the oblique angle. Thickness of the film is also important because the diameter of the tubes varies depending on this thickness. It is important to keep the parameters precisely constant in order to obtain highly reproducible results with non-epitaxial thin film in each process.

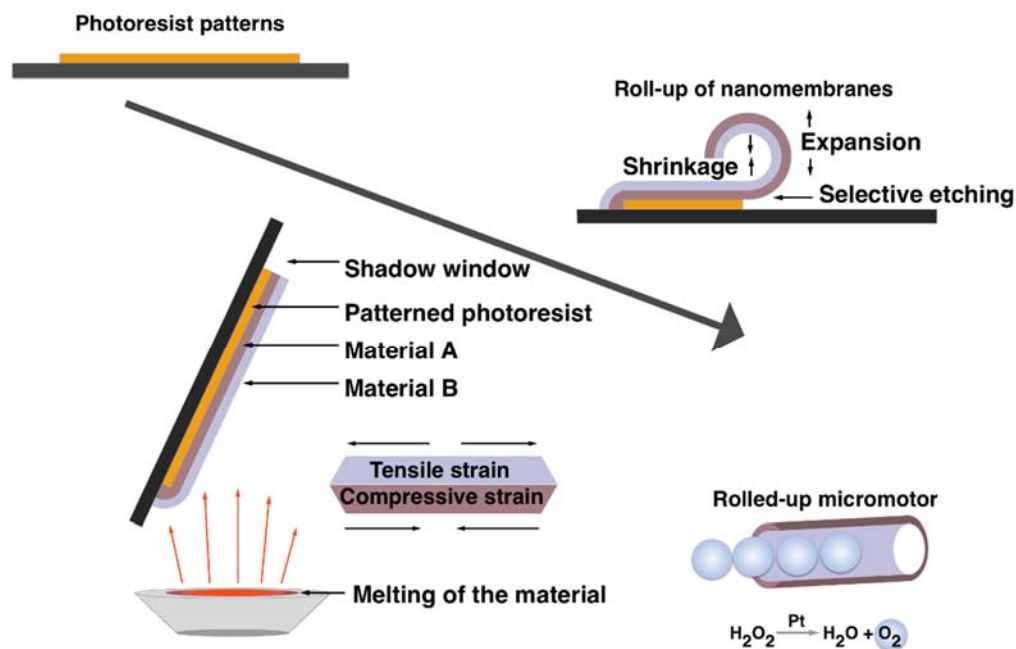


Figure 13. Spontaneous roll up process for fabrication of micromotors from nanomembranes<sup>60</sup>.

Overall, the rolling process consists of several steps (Figure 13). First, the sacrificial layers are patterned as substrate using photolithography techniques. The thin films

are then deposited with an oblique angle between the incident vapor flux and the patterned substrate to create shadowed window, where the materials are not deposited on the sacrificial layer. Such shadowed window permits the selective etching of the sacrificial layer from one side of the pattern. Etching process of the sacrificial layer release previously deposited strained multilayers, which then undergo stress relaxation process. During this process, lower layer expands and the upper layer shrinks. By tuning the etching time and the layer thickness, among other parameters, the diameter of micromotors can be effectively controlled<sup>29</sup>. Ideally, the multilayer membranes deposited with strain gradient across their thickness can be rolled up with many revolutions. The pattern size can be easily tuned by designing different photomasks applicable for photolithography. In this way, microtubes from 25  $\mu\text{m}$  up to 1 mm have been successfully reported in the literature, showing a large variability of lengths for various purposes.

### **Electrochemically synthesized tubular micromotors**

Electrochemical deposition techniques are known since more than 200 years and widely used for electroplating of metals in many industrial processes. Only in recent years electrochemical synthesis have been used for synthesis of nanomaterials and supramolecular systems. Template assisted electrochemical synthesis is commonly used approach for the synthesis of nanomaterials to precisely control the geometry of the nanostructures. The synthesis of electrodeposited catalytic micromotors has been first demonstrated by Wang's group in 2010<sup>31</sup>.

In a typical synthesis process (Figure 14), porous polycarbonate membranes are used as the templates to obtain the tubular shape of the micromotors. The membranes are not conductive, and conductivity is a necessary property for successful electrochemical synthesis, therefore a layer of carbon paste or thin film of gold is sputtered on one side the membrane to make that side conductive. The membrane is then assembled in an electrochemical cell for the synthesis process. The conductive part of the membrane is connected as the working electrode and an inert material, usually platinum, is connected as the counter electrode. A reference

electrode can be used in the same electrochemical cell to monitor the progress of the synthesis process.

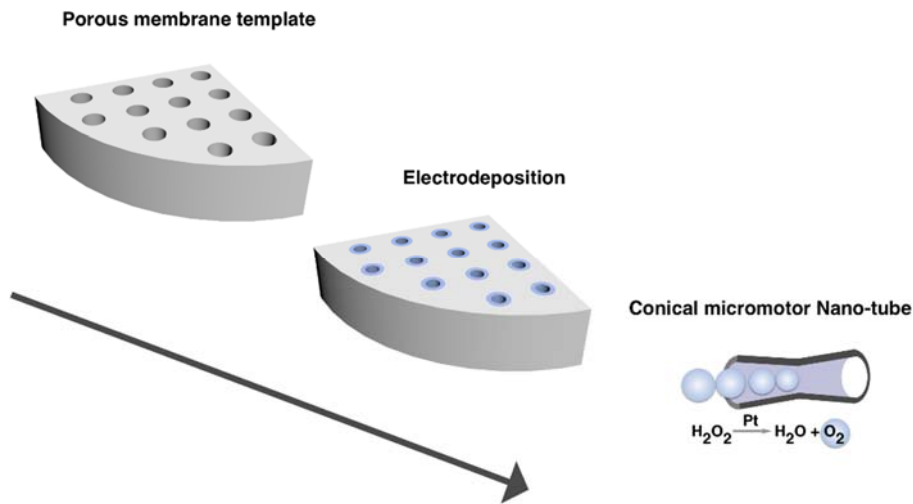


**Figure 14. Electrochemical synthesis of micromotors using porous membrane template.**

The structure is electrochemically grown from the electrochemical bath containing monomers of electro polymers or metal salts and other supporting chemicals. The electrodeposition of the materials starts from the conductive material previously deposited on the membrane. The synthesis protocol is designed to quickly deposit the precursor molecules on the conductive material and subsequently on the newly electrodeposited material. This fast deposition leads to complete deposition of the precursor molecules from the surrounding of the exposed conductive material before available molecules diffuses to the deposition location from the neighboring region. Because of this diffusion limited deposition process, the materials only grow on the walls of the polycarbonate template, leaving the core hollow. If the deposition is done slowly, the whole pore can be filled to synthesize rod like structures. After electrodeposition, the carbon or sputtered gold layer is completely removed polishing with alumina slurry and the membrane is dissolved by immersing it in methylene chloride solution to release the microtubes. In addition to the deposition of the basic bilayer of a polymer such as PEDOT, EDOT or PPy and Platinum (Pt), the deposition protocol can be tailored to include different functional

materials like graphene as outer layer and Nickel (Ni) and Gold (Au) layers for their magnetic guidance and facile functionalization (*i.e.* with receptors), respectively. These micromotors present intrinsically conical shape due to the shape of the templates used for the electrodeposition.

### Spherical micromotors

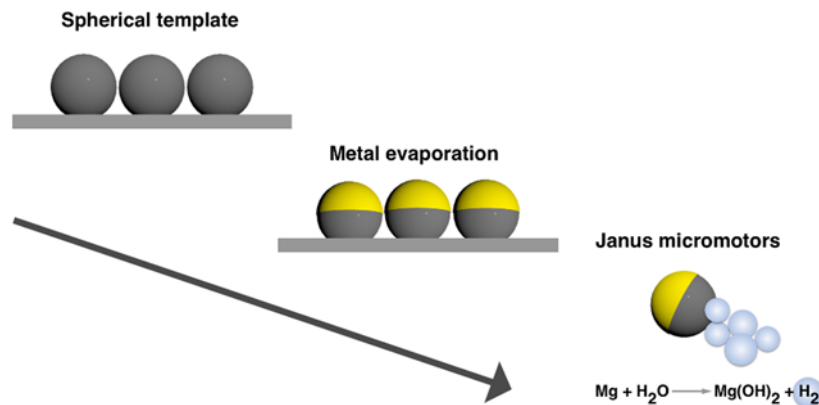


**Figure 15.** Fabrication of micromotors using monolayer of spheres as the template for asymmetric design of micromotors.

Spherical micromotors are fabricated by using solid spheres on which a layer of a material is deposited by physical vapor deposition techniques to make Janus particles. The solid spheres and the deposited material can be catalytic or non-catalytic depending on the target application of the Janus micromotors. The Janus microparticles with a catalyst coating are propelled by so-called diffusiophoresis mechanism or bubble propulsion mechanism depending on the size of the micromotors<sup>25</sup>. For example, the lack of confinement for bubble growth leads to diffusiophoretic motion for platinum coated Janus micromotors smaller than 10  $\mu\text{m}$  while bigger micromotors can move via bubble propulsion<sup>32</sup>. The non-catalytic micromotors used for environmental applications usually contain magnesium, which reacts with water to produce hydrogen gas ( $\text{H}_2$ ) for bubble propulsion<sup>61</sup>.

### 1.5.2. Mechanism of bubble propulsion

The mechanism for the motion of bubble propelled micromotors is associated with the production and release of bubbles by the micromotors. A few theoretical models are proposed to explain the thrust generated during the bubble propulsion and associated hydrodynamics. A model based on the bubble nucleation and ejection is described by Manjare *et al.*<sup>32,62</sup>. In this model, the bubble growth inside the tube and its ejection from one end of the micromotors are described as the main parameters responsible for the movement. Several other parameters are also described in this model, such as the concentration of the H<sub>2</sub>O<sub>2</sub> fuel, oxygen flux, rate of the bubble generation, frequency of the bubble ejection, radius of the micromotor and average speed of the micromotors during the bubble growth. However, some parameters such as the migration of bubbles generated at any other point of the tube are not considered. Since bubbles have been observed to form at various points of inner walls of micromotors, those steps could also be involved in the propulsion mechanism. In another theoretical model proposed by Li *et al.*, the bubbles and the tubes are separately considered for the explanation of the mechanism<sup>63</sup>. In this model, it is assumed that the micromotors and the bubble stop at the same time when they are separated by the distance of the micromotors diameter. Since after the separation both the micromotors and the bubbles may have different dynamics and possibly are not associated anymore, this model is controversial. Because of the importance of the geometry in the performance of these micromotors, a model which considers the non-uniform shape of the catalytic micromotors is described by Fomin *et al.* In this model authors have combined the time dependent hydrodynamics of the bubble growth and migration within the asymmetric shape of the micromotors<sup>64</sup>. The migration of the bubble in the micromotors creates the net force which pushes forward the micromotors. Authors have also compared their model with the other models proposed previously. They put forward the hypothesis that not the geometrical parameters, but the asymmetries are important for the jet effect and the motion of a perfectly symmetric micromotors as observed in the experimental results. It can be assumed that with the time, the volume of a growing

bubble increases in the asymmetric micromotors. It can be denoted by the following equation,

$$V(t) = kS_{cat}t. \quad (1)$$

Here,  $k$  is the rate of the oxygen production from a unit surface area and  $S_{cat}$  is the catalytic area. The fluid pumping induced by the bubble migration, along with recoil propel the tube. Authors proposed a simplified preliminary model for the mechanism with an assumption that relaxation of the micromotors momentum occurs at a finite rate in the surrounding fluid. The description of the fluid dynamics produced by the bubble motion in a micromotors rigorously indicates that a time-dependent hydrodynamic analysis is required. A momentum transfer to the fluid occurs because of the motion of the bubble in an asymmetric micromotors. The momentum transfer generates a motor force ( $F_{motor}$ ) on the micromotors,

$$F_{motor} = \frac{M*dVt}{dt} \quad (2)$$

where  $M$  is the mass of the tube and  $V_t$  is the velocity. On the other hand, swimming in the fluid creates the linear drag force that is acting on the micromotors.

$$F_{drag} = -2\eta\pi L \left[ \ln\left(\frac{L}{R_{max}}\right) - 0.72 \right]^{-1} * v_{tube} \quad (3)$$

and the balance of the forces ( $F_{drag} + F_{motor} = 0$ ), the tube instantaneous speed can be described as

$$v_{tube} = \frac{F_{motor}}{2\eta\pi L} \left[ \ln\left(\frac{L}{R_{max}}\right) - 0.72 \right] \quad (4)$$

and the average speed as

$$\langle v_{tube} \rangle (t) = \frac{1}{t} \int_0^t v_{tube}(\tau) d\tau \quad (5)$$

Micromotors with well-controlled velocities can be fabricated by considering different forces acting on it. For example, by controlling the shape and diameter of

the micromotors, well-defined velocities can be achieved because of the strong dependence of the velocities on the micromotors diameter. However, a separate analysis of the hydrodynamics of the fluid around the micromotors is still required.

## 1.6. State of the art of micromotors in environmental field

Even though initial reports on micromotors were focused on understanding the underlying mechanisms, the vision to develop real world applications of these tiny artificial motors for was always there since Feynman proposed the idea of swallowing a surgeon. There have been many early proof of concept applications reported for biomedical application of micromotors<sup>65,66</sup>. However, there are several issues related to biocompatibility that need to be addressed before micromotors can be used for biomedical applications. Whereas, biocompatibility is not an issue for many environmental applications and certain chemicals used as the fuel for micromotors are already being used in chemical processes for environmental remediation (e.g. H<sub>2</sub>O<sub>2</sub>). In this section, I will discuss important research on the environmental applications of micromotors published prior, or in the early days, of the commencement of my thesis work. A comprehensive discussion on the literature can be found in this review<sup>12</sup>.

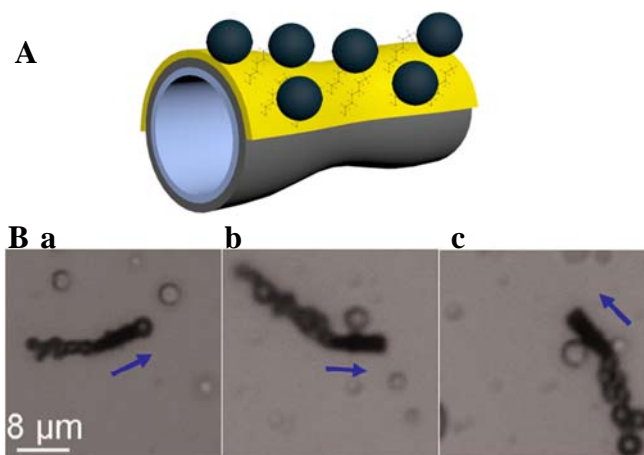


**Figure 16. Capture and transport of oil droplet by micromotors functionalized with alkanethiols chains<sup>67</sup>.** (A) Tubular micromotor with inner platinum core and our gold surface functionalized with hydrophobic chains. (B) Optical images of (a) micromotors moving towards a droplet (b) capturing it (c) and transporting it.

The first example of micromotors performing removal of oil pollutants was reported by Guix *et al.* in 2012<sup>67</sup>. They synthesized PEDOT/Pt tubular micromotors by

electrodeposition method in PC template and then, one side of their long axis was coated with a gold film (Figure 16A). These micromotors, powered by catalytic decomposition of  $\text{H}_2\text{O}_2$  by their inner platinum layer, were functionalized on their gold external surface with superhydrophobic n-alkanethiols chains with different lengths. The thiol group of the n-alkanethiols molecules assembles into self-assembly monolayers (SAM). The presence of long carbon-chains renders a hydrophobic surface, which can attract oil droplets molecules via hydrophobic interactions. Authors noted that longer chains (C12) were more efficient for capturing oil droplets than smaller chains (C6). Also, it was observed that the speed of the micromotors with the oil droplet on their surface decreased up to 10 times from the original speed. These results established that it is possible to capture pollutants “on the fly” via superhydrophobic surface modifications of micromotors. In the follow-up work, the same group designed Janus micromotors using magnesium microparticles propelled by bubbles of hydrogen gas generated during the reaction of magnesium with water<sup>68</sup>. These spherical micromotors have Janus structure with a gold layer sputtered on one half and functionalized with dodecanethiol molecules.

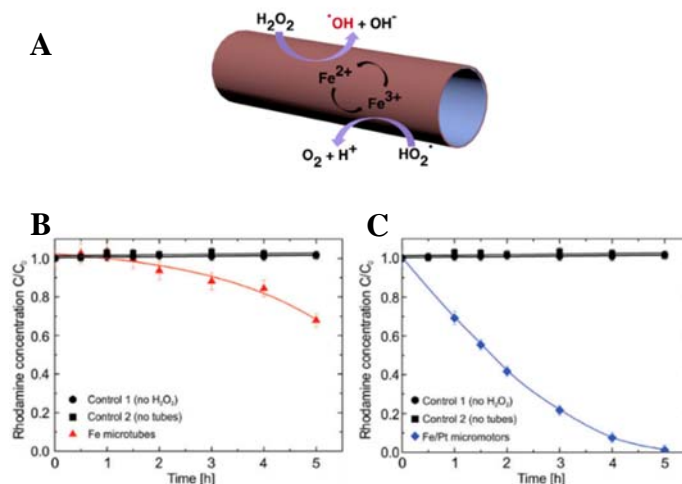


**Figure 17.** Fenton like oxidation reactions catalyzed by iron containing micromotors in  $\text{H}_2\text{O}_2$  fuel<sup>69</sup>. (A) Schematic (B) degradation of rhodamine dye by static iron tubes (C) enhanced degradation of rhodamine by self-propelled micromotors.

Removal of organic pollutants using micromotors was reported by Soler *et al.* in 2013<sup>69</sup>. These micromotors were fabricated by rolling up of the iron and platinum nanomembranes into tubular structures (Figure 17A). The iron layer present on the outer surface of the micromotors react with  $\text{H}_2\text{O}_2$  added as the fuel to carry out Fenton-like oxidation reaction and generate  $\text{HO}^\bullet$  radicals. The authors demonstrated degradation of rhodamine 6G (R6G), as a model pollutant of xanthene dyes via Fenton-like reaction using the micromotors. The total degradation of R6G was achieved after 5 hours of swimming of micromotors while the static Fe/Pt tubes only achieved around 50% degradation (Figure 17B, C). In addition, it was observed that the efficiency of the R6G degradation was dependent on the thickness of the iron layer on the micromotors, pH, and concentration of  $\text{H}_2\text{O}_2$ .

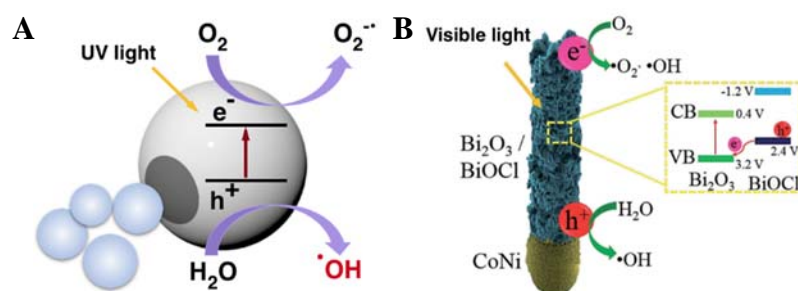


**Figure 18. Photocatalytic micromotors for removal of warfare agents and dye pollutant.** (A)  $\text{TiO}_2/\text{Mg}$  micromotors propelled by hydrogen generated during the reaction of Mg with sea water<sup>70</sup>. (B) Magnetically actuated photocatalytic  $\text{Bi}_2\text{O}_3/\text{BiOCl}$  micromotors for removal of dye<sup>71</sup>.

Photocatalytic reactions also generated highly oxidative radicals capable of degrading organic pollutants. In the presence of UV light,  $\text{TiO}_2/\text{Mg}$  micromotors can developed by Li *et al.* are demonstrated to oxidize methyl-paraoxon (MP) and ethyl-paraoxon (EP), highly toxic organophosphate nerve agent, by the generation of reactive oxygen species on their surface<sup>70</sup> (Figure 18A). Janus activated carbon/Pt microspheres reported by Jurado-Sánchez *et al.* can also remove MP, apart from the removal of lead ions and other organic molecules, also by its absorption on the activated carbon. Mushtaq *et al.* designed  $\text{Bi}_2\text{O}_3/\text{BiOCl}$ -based hybrid micromotors activated by UV-visible irradiation and controlled by an

external magnetic field instead chemical self-propulsion for the efficient removal of rhodamine B (RB) (**Figure 18B**)<sup>71</sup>. These hybrid micromotors were synthesized using a sequential template-assisted electrodeposition in two different shapes, micropillars, and microhelices which consist of a ferromagnetic segment followed by a bismuth-based photocatalytic segment. They exhibited 90% efficiency for removal of RB, being a good example of biocompatible, low-cost and wirelessly powered micromotors for water cleaning treatments.

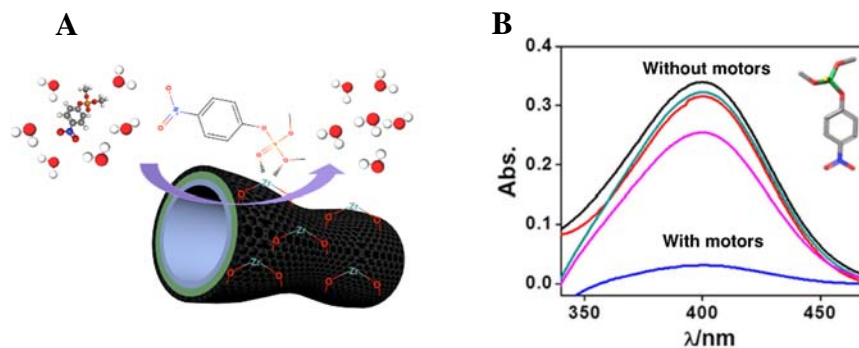


**Figure 19. Removal of organophosphates nerve agents by adsorption using micromotors**<sup>72</sup> (A) Zirconia functionalized micromotors. (B) Adsorption spectra of removal of methyl paraoxon with and without micromotors.

Singh *et al.* reported zirconia (ZrO) functionalized tubular micromotors to remove multiple extremely toxic organophosphate compounds (**Figure 19A**)<sup>72</sup>. In their design, they electrochemically synthesized tubular micromotors with platinum as the inner layer and ZrO was immobilized on the outer surface by electrochemical reduction of zirconium chloride. The results showed a significant role of ZrO for the effective removal of methyl paraoxon (MP), ethyl paraoxon (EP), and bis-4 nitrophenyl phosphate (b-NPP) *via* acid–base Lewis interaction of negatively charged oxygen atoms present in OP with the electronically deficient zirconia. These micromotors showed 91, 70, and 58% removal of MP, EP, and NPP, respectively, after 5 minutes in presence of H<sub>2</sub>O<sub>2</sub>. The removal was much faster by the self-propelled micromotors compared to static motors (**Figure 19B**). Sarin, another organophosphorus ester compound, is a potent toxic for the nervous system and a chemical warfare agent usually employed during chemical attacks. To remove

this potent toxic, multifunctional silver-exchanged zeolite micromotors have been designed to catalytically degrade diethyl chlorophosphate (DCP), a sarin simulant<sup>73</sup>.

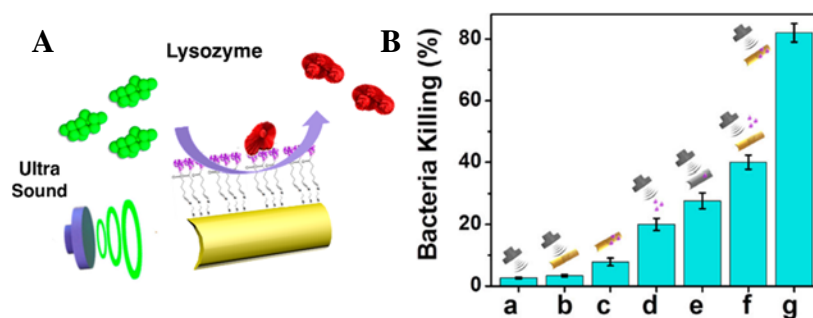


**Figure 20. Lysozyme based bactericidal micromotors<sup>74</sup>.** (A) Schematic of ultrasound propelled gold nanorod micromotors functionalized with lysozyme. (B) Comparison of bactericidal effects of ultrasound propelled micromotors (g) with various control experiments (a-f).

Micromotors focused on the removal of pathogenic bacteria from contaminated water, integrate on their structures several bactericidal materials or molecules such as enzymes, polymer, and metals. Micromotors can be designed for the selective isolation and destruction of bacteria by the modification of their structure with aptamers, antibodies, protein receptors and target enzymes. Campuzano *et al.* developed the first work to capture and isolate bacteria using micromotors by electrosynthesized Au-polyaniline-Pt tubular micromotors subsequent modified with lectin<sup>75</sup>. Once the micromotors were placed in H<sub>2</sub>O<sub>2</sub> solution, they selectively bind to the *E. coli* surface by antibody-antigen interactions and capture *E. coli* while swimming. Later, the same research group developed the first work to kill bacteria using nanomotors. They performed porous gold nanowires (p-AuNWs) propelled with an external ultrasound (US) source and functionalized on their surface with lysozyme, an antibacterial peptidoglycan-hydrolase (muramidase activity) enzyme that specifically damage the protective wall of bacteria<sup>74</sup> (Figure 20A). The p-AuNWs were fabricated using template electrosynthesis of different metal layers: (i) Ag sacrificial layer, (ii) Au layer and (iii) Au-Ag layer. The surface was chemically modified with lysozyme enzyme. Two kinds of bacteria, *M. lysodeikticus* and *E. coli*, were rapidly destroyed by these named “nanofighters” efficiently in

comparison with various controls, including static lysozyme-AuNWs and free lysozyme (Figure 20B).

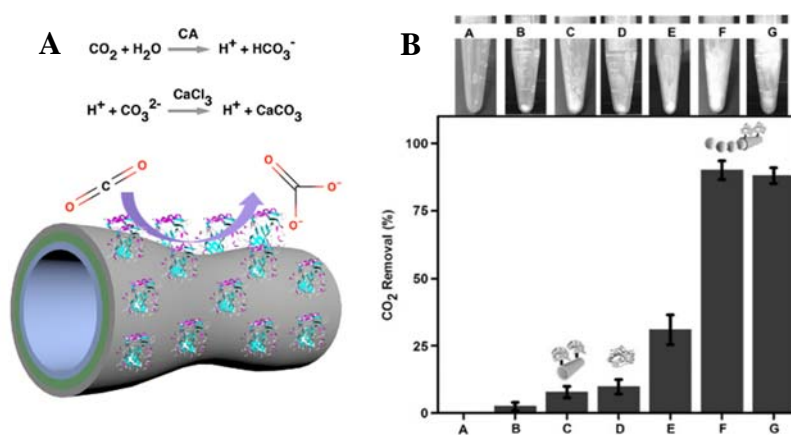


**Figure 21. Carbon dioxide sequestration by micromotors<sup>76</sup>.** (A) Carbonic anhydrase modified micromotors with platinum core (B) Precipitation of calcium carbonate by free enzyme, static micromotors and self-propelled micromotors

Micromotors are also demonstrated for enhanced carbon dioxide (CO<sub>2</sub>) sequestration. CO<sub>2</sub> emissions and its further accumulation are directly related to the climate change and global warming. Uygun *et al.* Reported an approach to capture CO<sub>2</sub> using micromotors modified with anhydrase (CA) on their surfaces for CO<sub>2</sub> sequestration in water and storage as solid carbonate salts<sup>76</sup>. These templates electrodeposited (COOH-polymer/Pt) tubular micromotors have been modified with CA using carbodiimide cross linker chemistry for the activation of carboxylic groups on the micromotors surface (Figure 21A). The CA- modified micromotors were able to convert CO<sub>2</sub> to bicarbonate ions (HCO<sub>3</sub><sup>-</sup>) while they swim in presence of H<sub>2</sub>O<sub>2</sub>. To avoid the CA equilibrium between CO<sub>2</sub> and bicarbonate species, CaCl<sub>2</sub> was added to the solution for carrying out the precipitation of HCO<sub>3</sub><sup>-</sup> in form of calcium salt (CaCO<sub>3</sub>) and activating the equilibrium of the conversion of CO<sub>2</sub> to HCO<sub>3</sub><sup>-</sup>. The motile CA functionalized micromotors were 5 times more efficient in removing CO<sub>2</sub> compared to static micromotors with the same functionalization (Figure 21B).

## 1.7. Enhanced mixing by micromotors

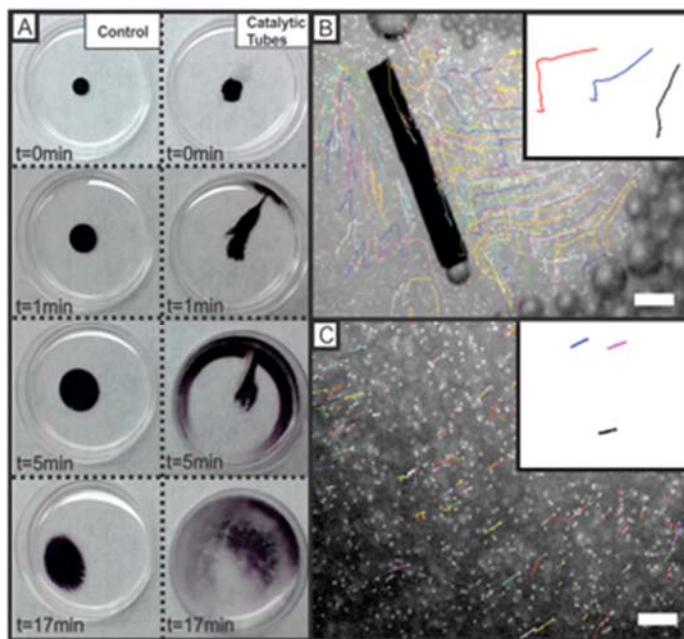


**Figure 22. Enhanced fluid mixing demonstrated by bubble propelled micromotors by tracking the tracer particles<sup>69</sup>.**

The accelerated removal of pollutants by micromotors is claimed to be due to activity induced improved mixing and mass transfer in the fluid while they are swimming. Mixing has a significant effect on the apparent kinetics of a chemical reaction, especially in the case of fast reactions. The intrinsic kinetics of a fast reaction are difficult to achieve, since many physicochemical steps that are involved in the reaction are limited by slow mass transfer of the reactants and products. Efficient mass transfer at the macro and mesoscale are relatively easy to achieve by using turbulence mixing or dispersion. However, it is quite challenging to achieve micro-mixing at low Reynold numbers because, at that scale, the flows are inherently laminar. These laminar flows and diffusion-related slow mixing can easily be observed in microfluidic systems. The transport phenomena involved in chemical or biological processes often occur at low Reynolds numbers. For example, in a heterogeneous catalysis or enzymatic catalysis process, the transport

of chemical species involved reaction (adsorption of the substrate and release of the product) has a significant effect on the overall reaction rate. The micromotors can enhance mass transfer and improve micro-mixing in the system where they are swimming. Soler *et al.* and Orozco *et al.* studied the transport of tracer particles by micromotors to explain the mixing effect imparted by the swimming micromotors in fluids (**Figure 22**)<sup>69,77</sup>. The results reported by Orozco *et al.* clearly demonstrated that the transport of tracer particles was significantly enhanced by bubble propelled PEDOT-Pt tubular micromotors compared to diffusiophoretic SiO<sub>2</sub>-Pt micromotors and electrophoretic Au-Pt micromotors. Apart from mixing effect induced by the motion of micromotors, in the case of bubble-propelled mechanism, bubbles can create additional mixing along with the three-dimensional swimming of the micromotors<sup>78</sup>. This could explain the accelerated rate of many pollutant removal processes by swimming micromotors described in the applications section. The work presented in this thesis deals with designing various bubble propelled micromotors for removal of different pollutants, as well as the exploration of the mixing effects of the bubbles generated. Besides, bubble propulsion is also one the fastest swimming mechanism, making them an ideal choice for chemical reactions used in environmental applications, where their active swimming and role in the mixing can be useful.

## CHAPTER 2.

### ORGANIC REMOVAL USING MICROMOTORS

**The results described in this chapter are published in the following article.**

Parmar, J.; Vilela, D.; Pellicer, E.; Esqué-de los Ojos, D.; Sort, J.; Sánchez, S. Reusable and Long-Lasting Active Microcleaners for Heterogeneous Water Remediation. *Adv. Funct. Mater.* **2016**, 26 (23), 4152–4161.

## 2.1. Introduction

Catalytic, self-propelled micro-motors use chemical fuel such as H<sub>2</sub>O<sub>2</sub>, hydrazine<sup>79</sup> or acetylene<sup>80</sup> for propulsion. Amongst them, H<sub>2</sub>O<sub>2</sub> is being most widely used as a fuel in combination with the platinum catalyst for propulsion<sup>81</sup>. Iron-containing micromotors swimming in H<sub>2</sub>O<sub>2</sub> can degrade organic pollutants *via* Fenton-like reaction<sup>69</sup>. The degradation rate of organics is much higher when motile micromotors are deployed compared to degradation using non-motile iron-containing tubes. H<sub>2</sub>O<sub>2</sub> is the main reagent in Fenton reaction, which is already in use for many commercial water treatment procedures<sup>82</sup> and it is also considered as a green reagent for sustainable chemistry because it is usually degraded into water and oxygen gas without producing any toxic chemicals<sup>83,84</sup>. The classical Fenton reaction generates hydroxyl radicals when Fe<sup>2+</sup> reacts with H<sub>2</sub>O<sub>2</sub>, as follows<sup>82,85–88</sup>.



During the reaction chain, Fe<sup>2+</sup> oxidizes to Fe<sup>3+</sup> and Fe<sup>2+</sup> regenerates back from Fe<sup>3+</sup> (equations 6 and 7). One of the main disadvantages of the classical Fenton reaction is that at the end of the treatment iron ions need to be removed from the solution by usually precipitation. The precipitation reactions require a high amount of chemicals and produce a large amount of sludge. Furthermore, sludge removal is an expensive process and requires a lot of energy. In addition, non-reusability of iron salt as a catalyst and energy requirement for mixing results in extra cost for the treatment. To overcome the disadvantages of classical homogeneous Fenton reaction, significant efforts have been made to develop heterogeneous Fenton catalysts<sup>89</sup>.

Towards the development of practical use of micromotors and to overcome the limitation of Fenton reaction, we studied the reusability, continuous swimming behavior and effect of long term storage on the reuse efficiency of Fe/Pt

micromotors, as well as iron release into the solution. The effect of different micromotors sizes on the organic dye degradation rate, surface chemical composition after the cleaning cycles and mechanical properties of micromotors were also studied to understand the system thoroughly. The micromotors used for this study were fabricated by nanomembranes roll-up method.

## 2.2. Results and discussion

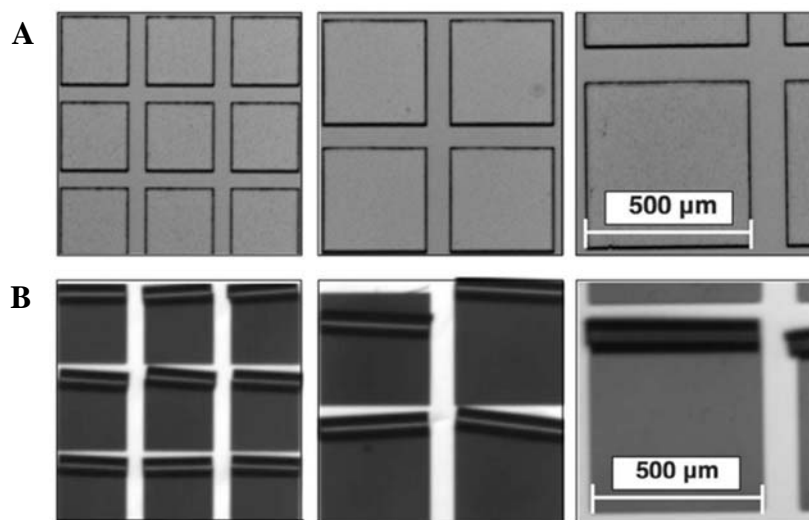


**Figure 23. Fabrication of micromotors.** A) 200  $\mu\text{m}$ , 300  $\mu\text{m}$ , and 500  $\mu\text{m}$  square photoresist patterns with e-beam evaporated Fe/Pt nanomembranes on it. B) Fe/Pt nanomembranes rolled up into 200- $\mu\text{m}$ , 300- $\mu\text{m}$ , and 500- $\mu\text{m}$  long micromotors with an approximate diameter of 40 to 60  $\mu\text{m}$ .

Pre-strained nanomembranes of iron and platinum were sequentially evaporated by e-beam on photoresist squared patterns of different sizes. The nanomembranes were selectively lifted off from the glass substrate by chemical etching and rolled up into micro tubular micromotors. The effect of size of the Fe/Pt micromotors on the degradation rate was studied using three different sizes of micromotors. For all sizes, equal area of previously designed photoresist patterns was deposited to keep the amount of catalytic material same in each experiment even though total number of tubes were different. Three sizes of micromotors (200  $\mu\text{m}$ , 300  $\mu\text{m}$  and 500  $\mu\text{m}$  long) were fabricated by rolling up Fe/Pt nanomembranes (Figure 23 A and B) and

used for the degradation of dye. Experimental parameters for the dye degradation are presented in the experimental section.

The platinum layer present inside the Fe/Pt micromotors act as the engine to decompose  $\text{H}_2\text{O}_2$  into  $\text{O}_2$  and  $\text{H}_2\text{O}$ . The oxygen bubble trail produces thrust on the micromotors to propel it which additionally provide micro mixing and enhanced mass transfer<sup>63,64</sup>. The iron layer present outside the micromotors reacts with the  $\text{H}_2\text{O}_2$  to produce hydroxyl radicals via Fenton-like reaction that degrades the organic compound. The pH was adjusted to 2.5 using sulfuric acid (the reported optimum pH is between 2-3 for the Fenton reaction catalyzed by zero valent metallic iron<sup>90,91</sup>) and the initial concentration of malachite green was kept to 50  $\mu\text{g/ml}$  in all the experiments. During the dye degradation experiments, dye concentration was periodically measured by the UV-visible spectrometer and the micromotors were left swimming in the contaminated dye solution until steady state of degradation was observed after 60 minutes. **Figure 24A** shows the dye degradation curves for 200  $\mu\text{m}$ , 300  $\mu\text{m}$ , and 500  $\mu\text{m}$  micromotors and control experiments without micromotors. The micromotors degraded more than 80 % of malachite green in 60 minutes; furthermore, complete degradation can be achieved over longer time (not shown). One-way analysis of variance (ANOVA) was calculated for all measured data points for groups of different sizes of micromotors to verify the statistically significant difference between them. There was no significant difference found in the amount of dye degraded by the groups of three different sizes of micromotors at the  $P = 0.9850$  ( $n=5$ ) level. Keep in mind that amount of catalytic material was same in each experimental group of micromotors with different sizes while total number of tubes were different due to the difference in the sizes.

Clearly, Fe/Pt micromotors show higher degradation rate compared to the control experiments without the micromotors as **Figure 24A** shows. According to previous literature, Fe/Pt micromotors were shown to outperform various other control experiments with non-iron containing motors such as Ti/Pt micromotors and

immobilized Fe/Pt micromotors in the dye degradation rate proving that the self-propulsion improves the performance this catalytic degradation process<sup>69</sup>.

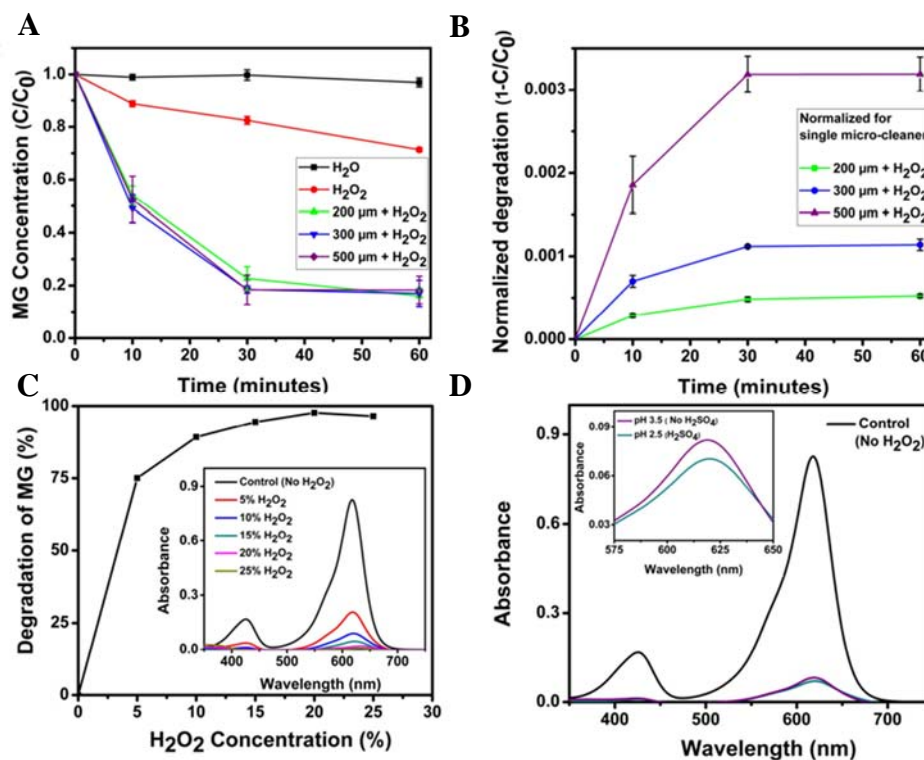


**Figure 24. Degradation of malachite green (MG) dye.** (A) Degradation of dye over time using different sizes of micromotors. (B) Dye degradation over time normalized for single micromotors (C) Degradation of malachite green at different concentrations of H<sub>2</sub>O<sub>2</sub> by 500 μm micromotors in 60 minutes (insert shows the light absorbance spectrum of malachite green at different pH concentrations). (D) Degradation of malachite green in 60 minutes, with and without the addition of H<sub>2</sub>SO<sub>4</sub> by 500 μm micromotors.

Figure 24B show normalized dye degradation by a single micromotor. This data is derived using total degradation by each size group and the number of micromotors present in that group, considering that all micromotors present in the solution contribute equally to the total degradation. The figure reveals that a larger micromotor of 500 μm is more effective than a 300 μm or a 200 μm micromotor. Provided that the amount of total rolled up catalytic material present in the solution is equal, i.e. 0.64 cm<sup>2</sup> in all cases, differences in the size of micromotors do not give added advantage and have limited effect on the degradation of dye in the studied

size range. The total amount of catalytic material plays a more important role than the size of the micromotors.

Since reusability of the catalyst is a crucial factor for cost effectiveness of the Fenton-based advanced oxidative processes, all three sizes of micromotors were studied for their reusability and to verify if the performance remains comparable in later usage cycles. In each cleaning cycle, micromotors were left swimming in the malachite dye contaminated water then collected using a permanent magnet and rinsed with ultrapure water before their reuse in subsequent cleaning cycles. The first five cleaning cycles were performed consecutively at 1 to 5 hours (each cycle is 60 min long), then next cycles were performed after 18 hours and 24 hours of storage of micromotors in sodium dodecyl sulfate (SDS) containing aqueous solution without H<sub>2</sub>O<sub>2</sub>. These experiments were designed to study the changes in the structure and degradation performance of micromotors after continuous reuse and short-term storage. Next sets of degradation cycles were performed after one week of storage interval between each cycle in order to capture effects of long term storage and reuse.

In the short-term reusability experiments, dye degradation by each size group of micromotors was between 68%-86% (**Figure 25A**). These results include continuous reusability from 1 to 5 hours without any time gaps (except short rising period between each cycle) and at 18 hours and 24 hours after short-term storage. After long-term storage (one week to five weeks), the degradation was slightly reduced to 56%-67%, as presented in **Figure 25C**. Percentages of degradation are in the similar range for group of varied sizes of micromotors in the different dye degradation cycles in short-term and long-term uses, which shows that the size of micromotors remains insignificant during reusability when the total amount of the catalytic material present is the same. Previously, iron layers were used for magnetic steering and guiding purpose<sup>92</sup>. Here, we exploited the ferromagnetic nature of the Fe layer as an added functionality to recover micromotors, along with Fenton reaction capability. Micromotors can be magnetically recovered and reused several times

without significant changes in the percentage of dye degradation efficiency, even after weeks of storage.

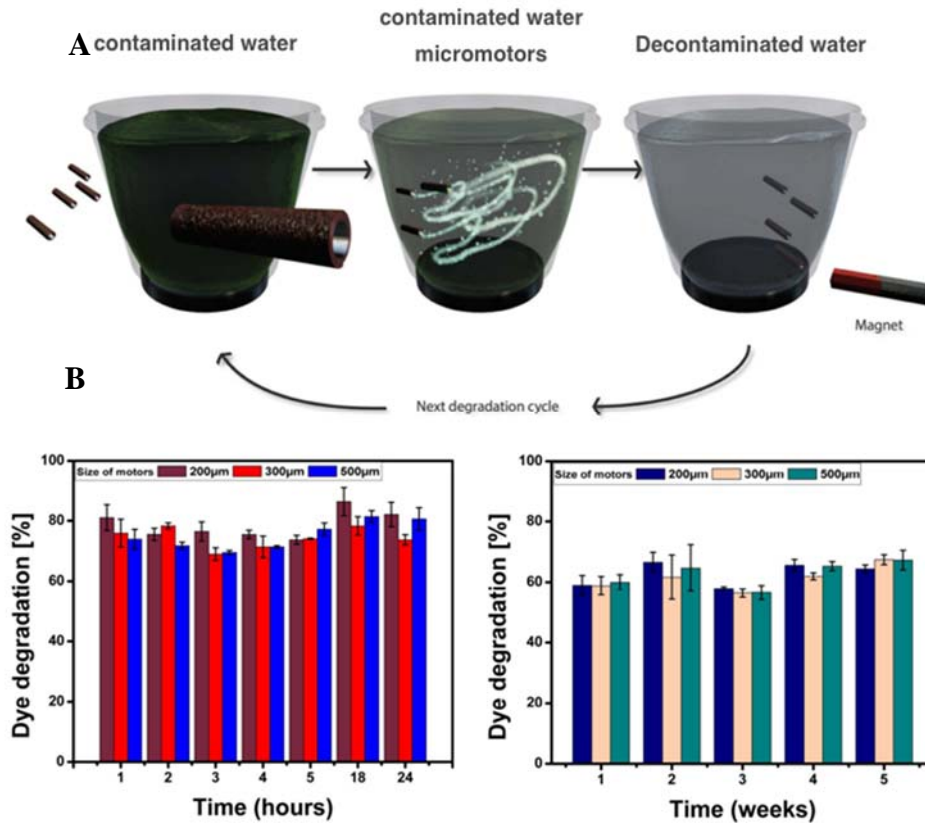


**Figure 25. Reusability of micromotors.** (A) Schematic diagram of reusability cycle of micromotors. Ferromagnetic micromotors were collected in a corner of the beaker and treated water was changed with Millipore water to wash the surface and the beaker itself. After cleaning the surfaces of the micromotors, new dye contaminated water was added for the next degradation cycle. (B) Reusability performance of different sizes of micromotors in 5 consecutive degradations during periods from 1 to 5 hours and at 18 hours and 24 hours after short-term storage. One degradation cycle is 60 minutes of swimming of micromotors in polluted water. (C) Reusability performance of micromotors in each cycle after 1 to 5 weeks of storage

After each reusability cycle, the swimming of the micromotors was observed under an optical microscope to assess the motility and bubble production activity. We noticed that the micromotors were still active after 5 weeks (including both short-term and long-term intermediate storage). The structural integrity was also observed

to be very good during initial cycles but in the later cycles, some longer micromotors were broken into two pieces or broken layers were visible while some shorter micromotors were broken in even smaller pieces without tubular geometry. Damage in the structure could be due to (i) multiples exposure of micromotors to the external magnetic field of a strong neodymium-iron-boron magnet during recovery process after every cycle and (ii) internal pressure of bubbles generated while swimming. Damage in the structural integrity could be one of the reasons for the observed decrease of dye degradation percentage in the later cycles after long-term storage (Figure 25C).

Apart from observing micromotors in each cleaning cycles, a separate experiment was carried out to observe them under them under the optical microscope while keeping them continuously swimming. All three sizes of micromotors were left swimming in H<sub>2</sub>O<sub>2</sub> (15% v/v) solution for 24 hours and swimming was observed periodically under the microscope. Figure 26 shows that all 200 μm, 300 μm and 500 μm micromotors were swimming even after 24 hours of continuous motion.

Although some micromotors were broken into smaller pieces after few hours of swimming, they were still active. Changes in the diameter were also observed after a few hours of swimming as in Figure 26. Namely, a decrease in the diameter is visible for longer micromotors in 24 hours images. An opposite effect was observed for 200 μm micromotors; some of them were opened up and broken into pieces. This difference is due to the presence of fewer numbers of windings in the micromotors fabricated from the smaller photoresist patterns. Since the same thickness of Fe/Pt nanomembranes rolled up from different sizes of photoresist patterns, similar diameters between 40 to 60 μm (and thus, different number of windings in the rolled up tubular micromotor structure) were achieved.

It is widely accepted that zero valent iron-mediated Fenton reaction is mainly a manifestation of ferrous ions generated from the iron surface in acidic pH. Fe<sup>2+</sup> ions leached from the surface in the solution play a key role in the reaction kinetics, which oxidizes into Fe<sup>3+</sup> ions during the Fenton reaction (equation 6). Regeneration

rate of  $\text{Fe}^{2+}$  ions from  $\text{Fe}^{3+}$  (equation 7) is a rate-limiting factor for classical Fenton reaction and the presence of metallic surface are believed to help the reduction of  $\text{Fe}^{3+}$  ion to  $\text{Fe}^{2+}$ , thus maintaining the Fenton reaction rate<sup>91</sup>.

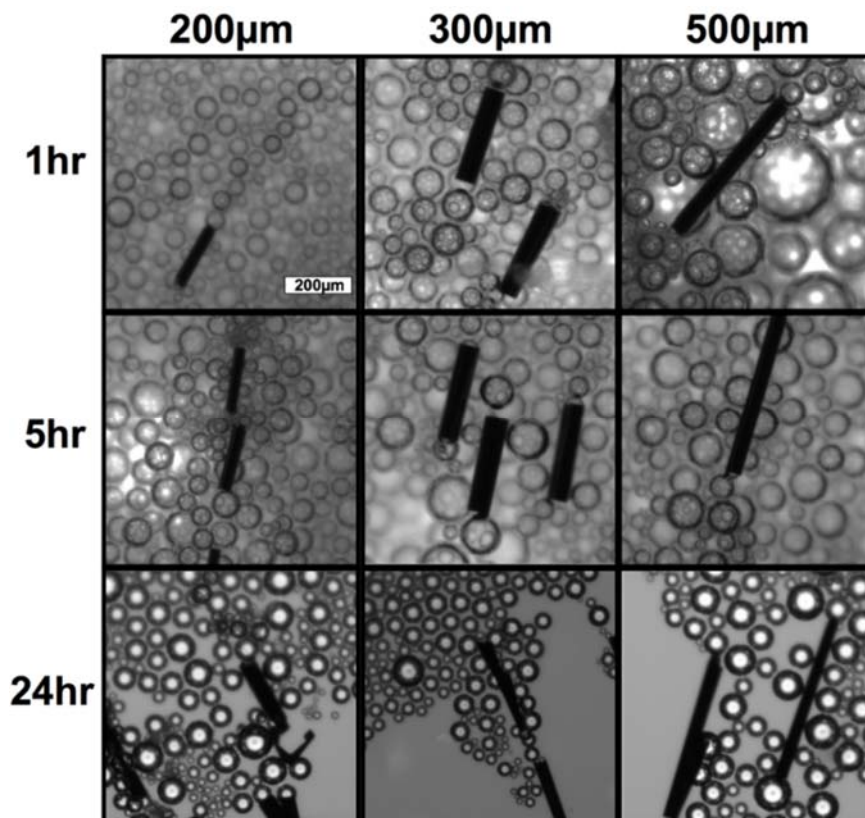


Figure 26. Micromotors of three different sizes (200  $\mu\text{m}$ , 300  $\mu\text{m}$  and 500  $\mu\text{m}$  long) swimming continuously at time intervals of 1 hour, 5 hours and 24 hours.

The iron released from the surface of micromotors in the solution was measured by inductively coupled plasma spectrometry (ICP-OES). Measurements were performed after 60 minutes of degradation cycle for up to 8 cycles. The measured iron concentrations for all three sizes of micromotors 200  $\mu\text{m}$ , 300  $\mu\text{m}$  and 500  $\mu\text{m}$  after the first cleaning cycle are ca. 2.10, 2.15 and 2.20  $\mu\text{g/ml}$  respectively. The similar concentration of iron in the solution for all sizes (Figure 27A) further proves a similar initial dye degradation rate for different sizes of motors (Figure 24A). In

the subsequent cycles, the concentration dropped sharply, and remained in a lower range, as shown in Figure 27A.

The initial ferrous ion concentration in the reaction mixture greatly affects the kinetics of the Fenton reaction. As reported by Hameed *et al.*, an iron concentration above 2  $\mu\text{g/ml}$  is sufficient to carry out classical homogeneous Fenton degradation of malachite green.<sup>93</sup> However, if the  $\text{Fe}^{2+}$  concentration in the solution is below 1  $\mu\text{g/ml}$ , the malachite green degradation rate should not be higher than the rate observed in the control experiment without  $\text{Fe}^{2+}$ . The dye degradation in first cycle can be attributed to the released iron from the surface of micromotors but from the second cycle onwards, the iron concentration was below 1  $\mu\text{g/ml}$ . Despite having the iron concentration lower than 1  $\mu\text{g/ml}$ , percentage of degradation only changes marginally. This result suggests a shift of the reaction pathway towards the heterogeneous Fenton reaction. There should be the formation of in-situ heterogeneous Fenton catalyst on the surface of the micromotors to achieve a dye degradation efficacy as in the first cycle. Also, the motion of micromotors can keep regenerating the active surfaces and increases the mass transfer to help maintaining the percentage of dye degradation.

To study surface changes occurred after Fenton reactions, micromotors were analyzed by X-ray photoelectron spectroscopy (XPS) using a PHI 5500 multitechnique system spectrometer, equipped with a monochromatic X-ray source. The micromotors before Fenton reaction, after Fenton reaction of 5 hours and after 5 weeks of storage were subjected to XPS analysis. The micromotors were washed with water and then dried in an ethanol- $\text{CO}_2$  critical point dryer before measurements (to dry without damaging the structure). Critical point drying is necessary to avoid the mechanical stresses generated due to the surface tension changes when the solvent on and around the micromotors is drying.

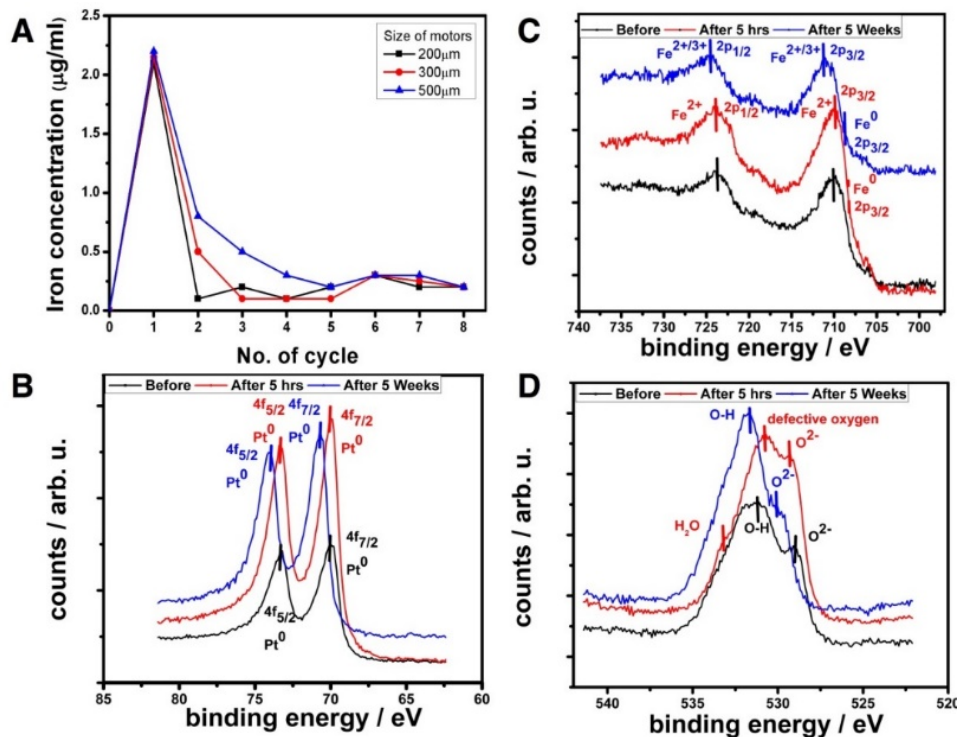


**Figure 27.** Iron release in the solution and the surface characterization of micromotors. (A) Iron concentration released in the solution after first cleaning cycle was above 2  $\mu\text{g/ml}$ , which decreased rapidly in the consecutive cycles and remained extremely low. (B, C, D) Fe 2p, Pt 4f and O 1s high resolution XPS spectra on the surface of micromotors before Fenton reaction after 5 hours of consecutive cleaning cycles and in the cycle after term storage of 5 weeks.

Fe is mostly present in an oxidized form at the outermost surface already before the Fenton reaction, as evidenced by the existence of a Fe2p doublet located at 709.8 and 723.9 eV, which can be assigned to Fe<sup>2+</sup><sup>94,95</sup> (Figure 27C). It is plausible to assume that the in situ generation of Fe<sub>x</sub>O<sub>y</sub> heterogeneous catalyst<sup>89</sup> at the surface of the micromotors reacts with H<sub>2</sub>O<sub>2</sub> to yield reactive oxidative species in the Fenton-like reaction after first use. In fact, the Fe 2p doublet is slightly shifted toward higher binding energies after 5 weeks of storage, indicating the presence of Fe<sup>3+</sup>. According to the literature, peak positions shift toward higher binding energies as the oxidation state of Fe increases<sup>96</sup>. Although the difference in binding energy between Fe<sup>2+</sup> and Fe<sup>3+</sup> oxidation states is very small (therefore, it is difficult to determine the relative amount of Fe<sup>2+</sup> and Fe<sup>3+</sup> in the micromotors), it is clear that

the surface becomes more oxidized. Notice also that the shoulder observed ca. 706 eV both before and after 5 hours of Fenton reaction and attributed to metallic Fe ( $2p_{3/2}$ )<sup>97</sup> weakens after 5 weeks. Hence, a complex mixture of iron oxides (FeOOH, Fe<sub>3</sub>O<sub>4</sub> or Fe<sub>2</sub>O<sub>3</sub>) is probably present at the surface of the micromotors after 5 weeks. Also, a slight shift in Pt 4f doublet is observed after 5 weeks of Fenton (**Figure 27B**). This might indicate oxidation of metallic Pt, but to a much less extent than Fe owing to the noble nature of Pt. Regarding the O 1s core-level spectra, a complex, broad signal with several maxima is observed (**Figure 27D**). After 5 hours of Fenton reaction the contribution from lattice O<sup>2-</sup> (529 eV) relatively increases, indicating again that the surface is more oxidized. Likewise, the peak at 530.7 eV has been attributed to non-stoichiometric oxides in the surface region (oxygen deficiencies)<sup>98</sup>. After 5 weeks, the O1s signal is dominated by the contributions from hydroxyl groups. Moreover, the Fe/Pt ratio markedly diminishes after Fenton reaction: 1.51 before Fenton; 1.37 after Fenton for 1 h; 0.90 after Fenton for 5 weeks, indicating that Fe undergoes leaching, in agreement with ICP analyses.

To assess the mechanical robustness and integrity of the micromotors, nanoindentation experiments were performed on the rolled tubular micromotors obtained from the 500 × 500 μm Fe/Pt flat films. Experiments were carried out (i) before Fenton reaction (ii) after 5 hours of Fenton reaction and (iii) after 5 weeks of storage.

**Figure 28** (A, left) shows the applied load (P) – penetration depth (h) indentation curve of a micromotor before the Fenton reaction (i.e., an unused micromotor). The test reveals a smooth loading behavior up to a load of about 0.1 mN, where a pronounced pop-in (i.e., sudden displacement burst) is observed. This displacement was associated to a cracking event of the material and was further verified through optical microscopy. **Figure 28** (A, center) shows the image of the tubular micromotor before indentation, while **Figure 28** (B, right) shows the same micromotor after indentation. Arrows in **Figure 28** (B, right) indicates a layer of micromotor that has been chipped away during indentation and, most likely, corresponds to the cracking event shown in **Figure 28** (A, left). A similar behavior, accompanied with a certain

barreling of the micromotors, was observed in all other investigated micromotors before Fenton reaction.

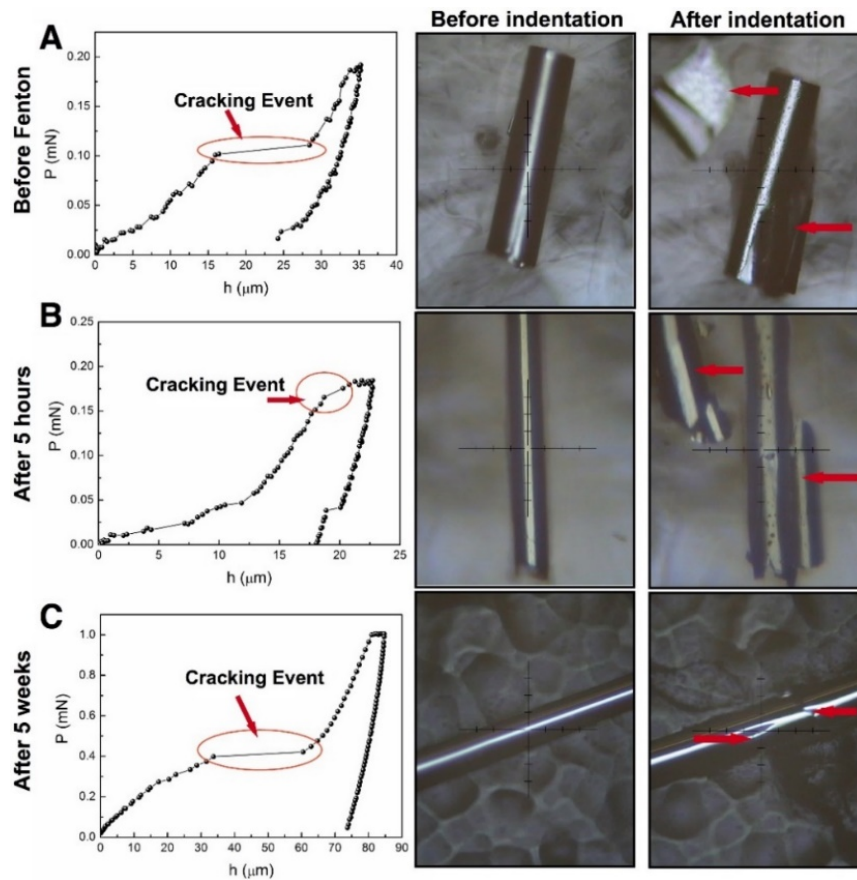


**Figure 28. Representative load ( $P$ ) – displacement ( $h$ ) curves and optical microscopy images of micromotors before indentation (center) and after indentation (right) corresponding to the micromotors. (A) before Fenton, (B) after 5 hours of Fenton and (C) after 5 weeks of storage. Arrows indicates chipped off layers and cracks of the micromotors that occurred during indentation and, most likely, associated to the cracking event shown in the respective load-displacement curve.**

A representative nanoindentation curve of the micromotors after 5 hours of Fenton reaction is shown in **Figure 28(B, left)**. The maximum penetration depth attained after Fenton reaction is smaller than before Fenton. Namely,  $h$  decreases from  $\sim 35 \mu\text{m}$  (before Fenton) to  $\sim 23 \mu\text{m}$  (after 5 hours), respectively. This means that the Fenton reaction induces an increase of the strength of the micromotors. Cracking events and exfoliation of the micromotors usually take place during indentation tests performed after Fenton reaction, although at loads typically close to  $0.2 \text{ mN}$  (see

**Figure 28**(B, center) and (B, right)). In summary, before Fenton reaction the micromotors appear to be more ductile, with higher attained penetration depths than for micromotors after Fenton reaction for a given value of maximum applied load (compare **Figure 28**(A) and 5(B)). Both, before and after 5 hours of Fenton reaction, indentation tends to cause a certain barreling of the tubes (particularly before Fenton reaction) inducing, finally, cracking and exfoliation of the outer shells of the tubes. As aforementioned, after 5 hours of Fenton reaction micromotors appear to be mechanically stiffer mainly because: (i) tightening up, reducing the diameter of the micromotor and increasing the number of layers (i.e., their thickness) and (ii) the formation of iron oxides at the outer surface of the micromotors as seen in the XPS analysis in **Figure 4**(C).

**Figure 28** (C) shows the results of nanoindentation on a micromotor after 5 weeks in storage. In this case, the penetration depth attained for an applied load of 0.2 mN is around 10  $\mu\text{m}$  and no cracking events were observed for this maximum applied load. In order to assess whether exfoliation of the micromotors takes place at higher loads, nanoindentation experiments were performed with  $P_{\text{Max}} = 1$  mN. As it can be observed in **Figure 28**(C, left), in this case a clear cracking event occurs at  $P \sim 0.6$  mN. This critical load for cracking is therefore higher than the one observed in **Figure 28**(A) and 5(B), suggesting an increase of mechanical resistance of the micromotors with usage. Typical optical microscopy images of these tubes before and after indentation with  $P_{\text{Max}} = 1$  mN are shown in **Figure 28**(C, center) and (C, right).

**Table 1.** shows the energy analyses performed during indentation of the micromotors for the three investigated conditions. Remarkably, the elastic recovery (i.e., the ratio between the elastic energy,  $U_{\text{el}}$ , and the total energy,  $U_{\text{tot}}$ ) after 5 weeks of storage is clearly larger than before Fenton or after 5 hours of usage. Hence, from a mechanical point of view, the tubes after Fenton are better than before Fenton, as fracture is clearly delayed and the elastic recovery is enhanced by more than a factor of 2 with respect to the as-prepared micromotors before Fenton.

**Table 1. Summary of the elastic ( $U_{el}$ ), plastic ( $U_{pl}$ ) and total ( $U_{tot}$ ) indentation energies for the micromotors. The ratio  $U_{el}/U_{tot}$  corresponds to the elastic recovery of the indented micromotors.**

Tube	Elastic energy $U_{el}$ (nJ)	Plastic energy $U_{pl}$ (nJ)	Total energy $U_{tot}$ (nJ)	$U_{el}/U_{tot}$
Before Fenton	0.97	2.71	3.68	0.26
After Fenton 5 hrs	0.46	1.83	2.29	0.20
After Fenton 5 weeks	2.13	1.67	3.80	0.56

Finally, nanoindentation finite element simulations were performed using the commercial software ABAQUS in order to shed further light on the mechanical performance of the micromotors.

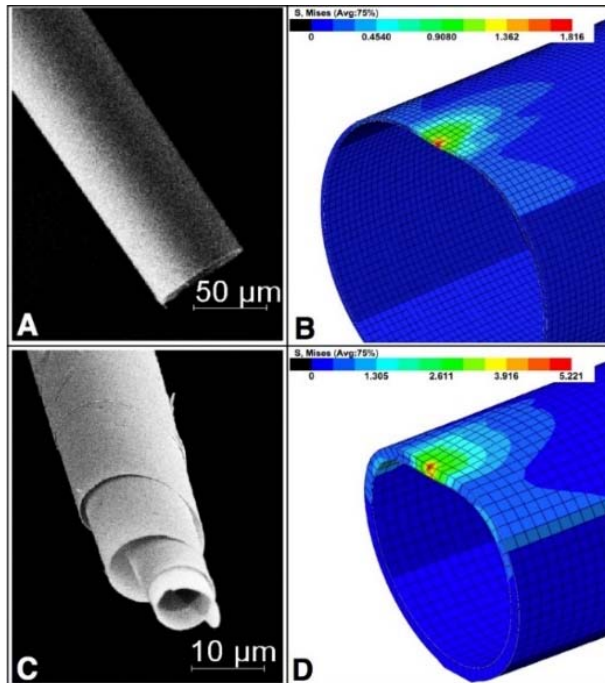


**Figure 29. Scanning electron microscopy images and Finite Element Modelling of (A) a micromotor before Fenton and (C) a micromotor after Fenton reaction, together with the simulated von-Mises stress distribution of indented micromotors with similar wall-to-thickness aspect ratios (B and D, respectively).**

The chosen geometry for the simulations was a cylinder with a wall-to-diameter aspect ratio similar to the investigated micromotors before and after 5 hours of

Fenton reaction. The mesh used during the simulations consisted of fully-integrated brick-shape elements, Berkovich indenter was considered as a perfectly rigid body and the cylinders perfectly elastic, with a Young's modulus equal to 200 GPa. Boundary conditions were such as to prevent the vertical displacement of the cylinder during indentation. The von Mises yield criterion was used to study the differences in the mechanical performance of the micromotors before and after 5 hours of Fenton reaction. The diameter of the micro clearers was decreased after the reaction (**Figure 29A** and **C**) due to the tightening of the layers, likely because of the pressure pulses generated during bubble development and release could promote the release of residual strains from the layers. The simulations reveal that the tube after Fenton reaction (**Figure 29D**) accumulates higher stress directly beneath the indenter tip for a given applied load than the tube before Fenton reaction (**Figure 29B**), indicating that it is mechanically harder. Concomitantly, for a certain applied load, the overall deformation of the tube before Fenton reaction is higher than in the simulated tube after Fenton. The results of this simple simulation (which does not take into account the multiwall structure of the micro-tubes) agree qualitatively well with the experimental observations.

In order to demonstrate the remediation capabilities of micromotors to other organic pollutants, we performed a degradation experiment for a phenolic compound (4-nitrophenol) using 500  $\mu\text{m}$  micromotors. 4-nitrophenol is one of the most common organic pollutant molecules present in industrial wastewater. Degradation of 4-nitrophenol is challenging using bacteria, yet hydroxyl radicals are capable of completely mineralizing it into carbon dioxide. **Figure 30** shows that using  $\text{H}_2\text{O}_2$  as oxidant alone cannot degrade 4-nitrophenol, while micromotors can degrade around 30% in 60 minutes.

## 2.3. Conclusions

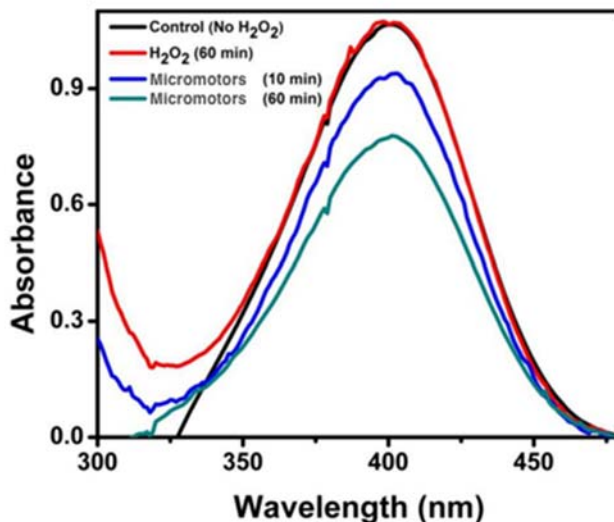


Figure 30. Degradation of 4-nitrophenol by  $\text{H}_2\text{O}_2$  control in 60 min (red), 500 $\mu\text{m}$  micromotors in 10 min. (blue) and 60 min. (cyan). Black line indicates control with  $\text{H}_2\text{O}$

The difference in the percentage of degradation for malachite green and 4-nitrophenol is due to the different reaction kinetics of hydroxyl radicals for different organic molecules. Micromotors degraded  $\approx 18 \mu\text{g}$  of 4-nitrophenol in 10 minutes and  $\approx 41 \mu\text{g}$  in 60 minutes from 3 mL of contaminated water containing  $150 \mu\text{g}$  of initial amount ( $50 \mu\text{g mL}^{-1}$ ). A longer duration is required to achieve complete degradation, but the addition of larger amounts of micromotors could achieve faster oxidation and even total degradation.

## 2.3. Conclusions

We demonstrated reusable, self-propelled Fe/Pt micromotors that can carry out a Fenton-like reaction with high activity and without the need for external mixing. We found that the variation in the length of micromotors does not affect the performance if the amount of catalytic material used is kept constant. The reusability results showed that the micromotors can be recovered using magnets and reused for multiple times within a short duration of less than a week without any decrease in their organic-degradation performance. Even longer-term storage for

several weeks is possible without sacrificing much of the activity. The micromotors can also be used for continuous swimming applications for at least 24 hours. Although the iron released into the treated water from the second cycle onwards was much less compared to that from the first cycle, the activity of the micromotors remained constant. We observed that the surface of the micromotors oxidized to produce in situ iron oxides that act as a heterogeneous catalyst. The formation of iron oxides along with the tightening of the rolled-up layers increased the mechanical strength of the micromotors after the Fenton reaction. Degradation experiments of 4-nitrophenol and malachite green proved the possibility of using micromotors for wide range of organic pollutants. The experiments presented here evidence the long-term reusability of very active micromotors, which will be beneficial towards lowering the cost of the water treatment using this advanced technology.

## 2.4. Experimental section

### 2.4.1. Fabrication of the micromotors

Micromotors were fabricated by rolling up the nanomembranes of iron and platinum metal deposited on square patterns of photoresist. Positive photoresist patterns (200  $\mu\text{m}$ , 300  $\mu\text{m}$  and 500  $\mu\text{m}$ ) were developed using standard photolithography techniques. Positive photoresist (ARP 3510) was spin coated (3500 rpm for 35 s) on previously cleaned glass wafers (18x18 mm) to make a layer with uniform thickness (2.4  $\mu\text{m}$ ) and exposed to the UV light under a chromium mask with the respective sizes of patterns confined in 1  $\text{cm}^2$  area by a mask aligner. Photolithographic patterns on glass substrates were developed (using 1:1 water/AR 300) and dried by blowing nitrogen before depositing the metal nanomembranes. A custom-built e-beam evaporator was used for the deposition. Two layers of iron (100 nm) were evaporated at different deposition rates (at 0.30  $\text{nms}^{-1}$  and 0.06  $\text{nms}^{-1}$  respectively); third layer of platinum (5 nm) was evaporated (at 0.02  $\text{nms}^{-1}$ ). All three layers were deposited at the glancing angle (65°), which leads to a non-deposited window at

each pattern. The photoresist walls, adjacent to the non-deposited windows, remain exposed which was required for the controlled directional rolling of nanomembranes. A mixture of dimethyl sulfoxide (DMSO) and acetone (1:1) was used to etch photoresist selectively from the exposed wall. The nanomembranes were rolled up from the side of the exposed wall to the unexposed wall in the shape of tubular micromotors.

### 2.4.2. Size effect and reusability experiments

Three different sizes of micromotors (200  $\mu\text{m}$ , 300  $\mu\text{m}$  and 500  $\mu\text{m}$  long with the diameter between 40-60  $\mu\text{m}$ ) were fabricated from the nanomembranes deposited on photoresist patterns that were confined in 1  $\text{cm}^2$  area on the glass substrate. The number of micromotors rolled up from a constant amount of catalytic material present in 0.64  $\text{cm}^2$  area including all square patterns were different for different sizes of patterns ( $\sim 1600$ ,  $\sim 729$ ,  $\sim 256$  respectively for sizes in increasing order). After rolling up, micromotors were first transferred into SDS water (0.5 % w/v) and then used for degradation experiments, carried out in a beaker containing total 3 ml of polluted water consisted of malachite green (50  $\mu\text{g}/\text{ml}$ ),  $\text{H}_2\text{O}_2$  (15% v/v) and SDS (0.5 % w/v) at the adjusted acidic pH (2.5). Dye concentration was measured by a spectrophotometer (Specord 250, Analytical Jena) at 0, 10, 30 and 60 minutes during the experiments to study the effect of sizes.

In a different batch, micromotors of all sizes were fabricated using the same parameters that were used for size effect experiments to study the reusability. All three sizes of micromotors were reused after short and long-term storage. Short-term experiments were carried out at varying time intervals; first five cycles were carried out at 1 to 5 hours continuously changing polluted water after the end of the 60 minutes of a degradation cycle. After the end of each cycle, micromotors were confined in a corner of the beaker using a strong neodymium-iron-boron hard magnet and the treated water was replaced with pure water (Millipore water) to clean the surfaces of micromotors, cleaning step is repeated twice and then polluted

water solution is added for the next cycle. Polluted water composition was kept same as in the size effect experiments. After 5 hours, micromotors were cleaned and stored in SDS water (0.5% w/v) before using in next cycles at 18 hours and 24 hours from the first cycle. In a similar fashion, long term storage experiments were carried out using the same micromotors after 1 week of intermediate storage between two cycles up to 5 weeks from the first cycle. Dye concentration after each cycle was measured by the UV-Vis spectrophotometer. After each cycle, treated water was collected and further analyzed by ion coupled plasma (ICP-OES) method to measure the iron concentration that was leached from the surface of micromotors.

### 2.4.3. Continuous swimming experiment and video recording

An upright microscope (Leica DFC3000G camera) was used to record rolling up videos for different sizes of micromotors while an inverted microscope (Leica DMI300B) was used to study the swimming behavior of micromotors after each cleaning cycle. A custom designed 3D printed microscope stage was fabricated to record the swimming of micromotors directly in the beaker where the degradation experiment was going on.

During the continuous swimming experiment, micromotors were observed under the inverted microscope at 1, 5 and 24 hours.

### 2.4.4. Surface characterization

X-ray photoelectron spectroscopy (XPS) analyses were carried out on a PHI 5500 Multitechnique System (from Physical Electronics) spectrometer, equipped with a monochromatic X-ray source ( $K_{\alpha Al}$  line with energy of 1486.6 eV and 350 W), placed perpendicular to the analyser axis and calibrated using  $3d^{5/2}$  line of Ag with a full width at half maximum (FWHM) of 0.8 eV. The analysed area was a 0.8 mm diameter disk surface for each sample. Charging effects were corrected by referencing the binding energies to that of the adventitious Cls line at 284.5 eV.

### 2.4.5. Mechanical properties

Micromotors were dried using an ethanol-CO<sub>2</sub> critical point dryer before doing the nano-indentation experiments. Typical load-displacement measurements were conducted on the micromotors before Fenton reaction, after 5 hrs of Fenton reaction and after 5 weeks. For the sake of simplicity, the micromotors obtained from the 500 x 500 μm Fe/Pt layers were selected for the mechanical tests. Experiments were performed in load-control mode, using a UMIS instrument from Fischer-Cripps Laboratories equipped with a Berkovich pyramidal-shaped diamond tip. Maximum applied load values ranged between 0.2 mN and 1 mN. To ensure statistically meaningful results, at least 10 indentations were performed for each type of micromotors and the representative average behaviour is reported. The elastic ( $U_{el}$ ) and plastic ( $U_{pl}$ ) energies during indentation were assessed from the areas enclosed between the unloading segment and displacement axis ( $U_{el}$ ), and between the loading and unloading segments ( $U_{pl}$ ). The total indentation energy is  $U_{tot} = U_{el} + U_{pl}$  and corresponds to the area enclosed between the loading segment and the displacement axis. The ratio  $U_{el}/U_{tot}$  denotes to the elastic recovery of the tubes after having been indented.

## CHAPTER 3.

# HEAVY METAL REMOVAL USING MICROMOTORS

**The results described in this chapter are published in the following article.**

Vilela, D.; Parmar, J.; Zeng, Y.; Zhao, Y.; Sánchez, S. Graphene-Based Microbots for Toxic Heavy Metal Removal and Recovery from Water. *Nano Lett.* **2016**, 16 (4), 2860–2866.

### 3.1. Introduction

Pollution in water from heavy metals such as arsenic, mercury, cadmium, chromium and lead, originates from various human industrial activities such as electroplating, mining, fabrication of batteries and microelectronics. It is a potential hazard to living systems; hence, it is essential to develop efficient and inexpensive materials and technologies to remove and recycle them from polluted water. Various methods are in use to remove and recover heavy metals such as chemical precipitation, adsorption, ion exchange and membrane filtration amongst which adsorption is considered an economical and effective strategy<sup>99</sup>.

Recent developments in nanotechnology have further increased the effectiveness of adsorbent materials providing innovative systems for improving environmental remediation<sup>10,100</sup>. Lately, numerous reports described the utilization of graphene and its composites as good adsorbents for the removal of dyes and heavy metal ions from aqueous solutions<sup>101-103</sup>. And, the synergy between active motion of micromotors and surface functionalization with active materials is exploited for various organic removal and environmental sensing applications, such as the detection of heavy metals<sup>104,105</sup>, pH<sup>106</sup> or other analytes<sup>107-109</sup>. However, the capture of heavy metals, their release in defined locations and the re-use of micro-motors for further cleaning was not reported. We presented the removal and recovery of heavy metals (lead) from contaminated water by using graphene oxide (GOx) based tubular micromotors, propelled by a catalytic reaction. The high adsorption of Pb (II) ions on the graphene oxide (GOx) nanosheets of the micromotors surface is a spontaneous process due to the strong surface complexation between the Pb (II) ions and the abundant oxygen moieties on the GOx. Moreover, due to the magnetic properties of these micromotors, they can be easily removed from the water using a magnet after successful lead decontamination. The adsorbed Pb(II) ions on the micromotors can be recovered *via* acid pH adjustment allowing them to be recycled and reused for further decontamination processes.

## 3.2. Results and discussions

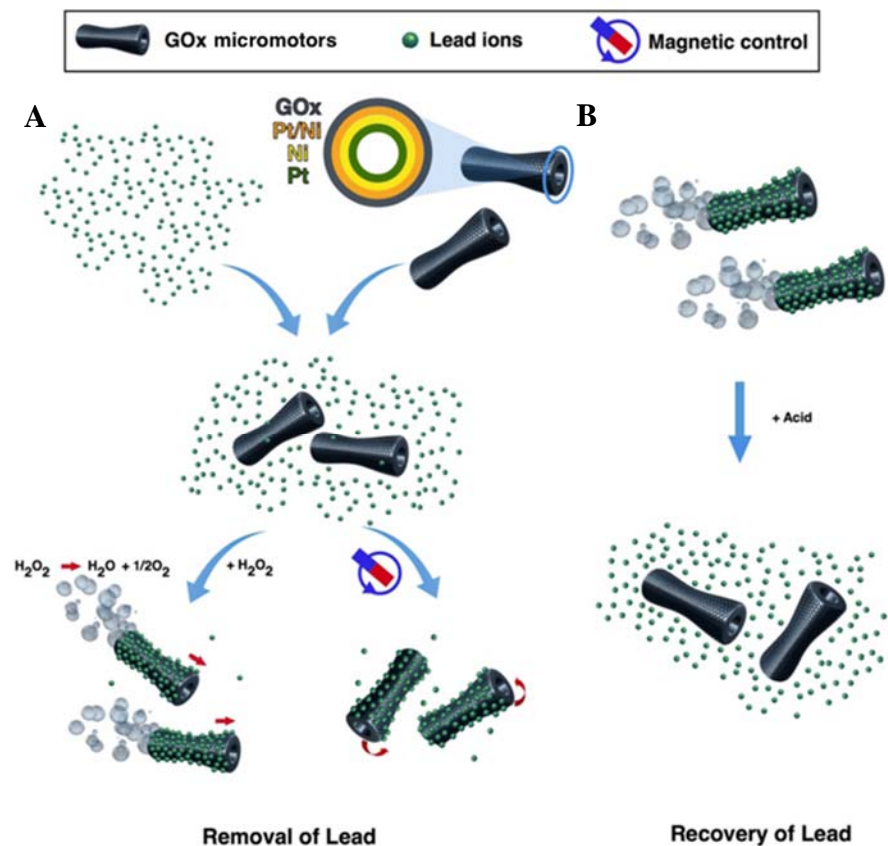


**Figure 31. Scheme of GOx-micromotors based approach for lead decontamination and recovery.** (A) Decontamination of polluted water using GOx-micromotors fabricated by electrodeposition of nanolayers of graphene oxide (GOx), Pt/Ni layer, Ni magnetic layer and Pt catalytic inner layer. (B) Recovery of lead ions from the GOx-micromotors in presence of acidic media.

As shown in **Figure 31A**, the micromotors structure consists of an outer graphene layer and a platinum inner layer. The platinum layer decomposes  $H_2O_2$  into water and oxygen microbubbles; and the ejection of microbubbles from one side of micromotors provides enough force for its self-propulsion. Between the Pt and GOx, layers of Pt/Ni and Ni were deposited to control and guide micro-bots motion by externally applied magnetic field. The detailed fabrication of conical, self-propelled tubular motors by sequential electrochemical deposition of nanolayers on

the inner wall of a polycarbonate membrane is described in the experimental section.

Taking advantage of the self-propulsion and magnetic properties of the micromotors, in combination with the GOx adsorption properties to attach Pb (II) ions, two approaches for the removal of lead were used (Figure 31A). In addition, the recovery of lead after its removal from wastewater was also carried out, as it is displayed in Figure 31B.

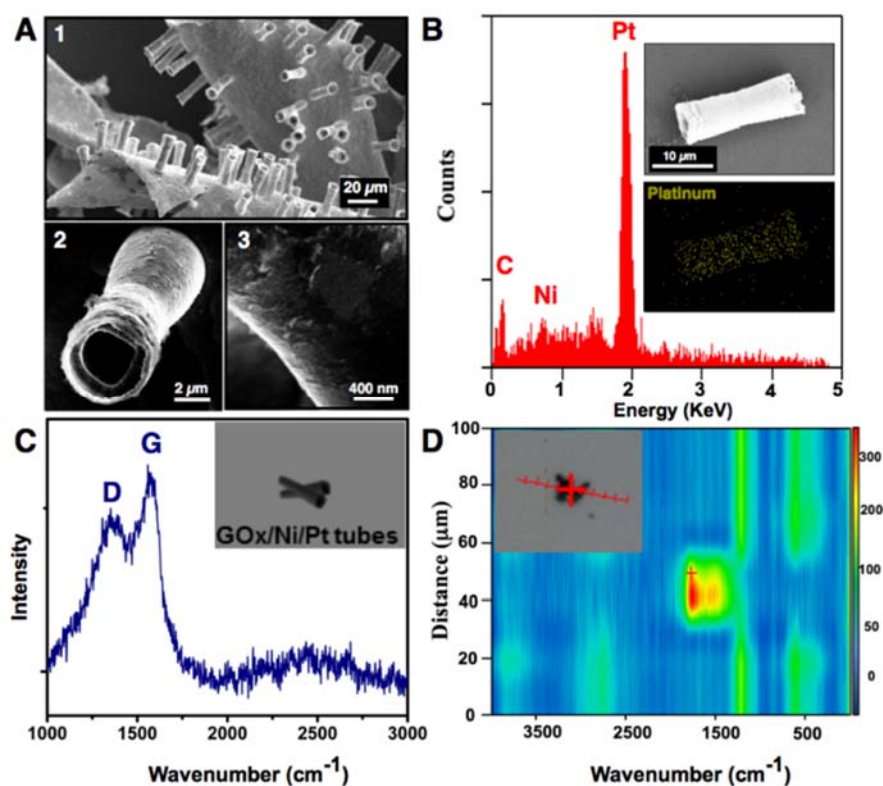


**Figure 32. Characterization of GOx-micromotors: (A) SEM images illustrating.** (1) GOx-micromotors attached to the gold layer, (2) structure of a single GOx-micromotor and (3) close look of the surface of a GOx-micromotor. (B) The EDX spectrum of GOx-micromotors (inset: EDX mapping of the GOx-micromotor for Pt). (C) Raman Spectrum from the surface of GOx-micromotors, showing characteristic D and G band of graphene oxide. (Inset is an illustration of the GOx-micromotors analyzed by Raman spectroscopy). (D) Raman spectroscopy displays the Raman scan map of the GOx-micromotors, confirming the presence of graphene on the full surface of micromotors (see inset: Image of the GOx/Ni/Pt tube and scanning path (Red line) of the analysis).

GOx-micromotors were characterized by scanning electron microscopy (SEM), energy dispersive X-ray spectroscopy (EDX), Raman spectroscopy and high-resolution X-ray photoelectron spectroscopy (XPS), as it is observed in **Figure 32**. **Figure 32A-1** illustrates the tubular morphology and size polydispersity of the micromotors after their fabrication. Most of the micromotors show bi-conical morphology and a low polydispersity indicating that fabrication was homogenous. **Figure 32A-2** displays the hollow inside layer of a representative micromotor. Their average outer diameter is  $4.6 \pm 0.1 \mu\text{m}$  ( $n=10$ ) and their inner diameter of  $2.5 \pm 0.1 \mu\text{m}$  ( $n=10$ ). The surface of micromotors is inhomogeneous, as it is shown in **Figure 32A-3** which can be due to the high number of defects produced by the non-homogeneous electrochemical deposition of graphene nanosheets on the polycarbonate membrane during the fabrication of these micromotors. **Figure 32B** illustrates the EDX analysis and reveals the components of the micro-bots including carbon, nickel and platinum where platinum is the major component. Raman spectroscopy analysis and mapping for GOx-micromotors are shown in **Figure 32C** and **D**, respectively. **Figure 32C** shows Raman spectrum of the micromotor surface where the characteristic peaks of D and G band are observed at  $1350$  and  $1570 \text{ cm}^{-1}$ , respectively. Usually, the D-mode is caused by disordered structure of graphene, while band G arises from the stretching of the C-C bond in graphitic materials and is common to all  $\text{sp}^2$  carbon systems. The band intensity ratio of  $I_D/I_G$  suggests the abundant presence of oxidized carbon in GOx-micromotors. To further confirm the complete coverage of GO layer on micromotors, the GOx-micromotors were characterized by confocal Raman technique. As shown in the bright field image (**Figure 32D** inset), a trimer of GOx-micromotors formed by physical attachment was chosen for the Raman mapping. By mapping integrated intensity values of D and G bands in Raman spectrum of GOx-micromotors, a 2-D Raman line mapping image was acquired and is presented in **Figure 32D**. Homogeneous distribution of high intensity signal in red and yellow colors resembles the width of a trimer with similar dimension. The confocal Raman line mapping image confirmed the successful and uniform coverage of GO on the surface of micromotors.

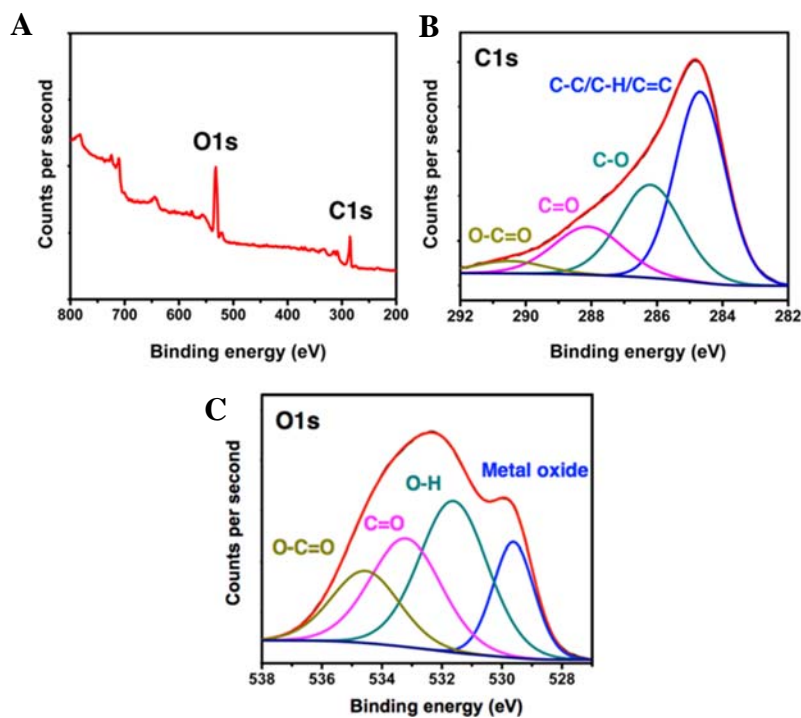


**Figure 33.** XPS spectra survey of GOx-micromotors. (A) showing O1s and C1s peaks. (B and C) High resolution C1s and O1s XPS spectra of GOx micromotors displaying various functional groups identified on the surface.

XPS spectra survey further reveals the presence of carbon (C1s peak) and oxygen (O1s peak) elements on the surface of GOx-micromotors, where the O1s signal is higher compared to the C1s signal (Figure 33A) characteristic for GOx. The peaks of high-resolution C1s spectra (Figure 33B) and O1s spectra (Figure 33C) correspond to the binding energy of various functional groups such as C-C/C-H/C=C, C-OH, C=O and O-C=O, revealing the nature of the covalent bonds of oxygen atoms and carbon atoms (Table 2).

The ratio of percentage atomic concentration of C-C/C-H/C=C functional groups to all carbon-oxygen functional groups is 0.94, which denotes the degree of oxidation of GOx. Abundant carbonyl and carboxyl groups are present on the GOx-micromotors which are considered very important for the adsorption of heavy metals on the surface of graphene oxide<sup>110</sup>.

**Table 2. Various functional groups identified on the surface of GOx-micromotors.**

Spectra	Group	Position	%At
C 1s	C-C/C-H/C=C	284.68	48.638
C 1s	C-O	286.19	29.875
C 1s	C=O	288.09	17.099
C 1s	O-C=O	290.49	4.387
O 1s	Metal oxide	529.61	17.231
O 1s	O-H	531.61	37.207
O 1s	C=O	533.2	27.858
O 1s	O-C=O	534.55	17.703

To prove the capability of the self-propelled GOx-micromotors for the purification of lead contaminated water by adsorption, a concentration of 1.5% v/v of H<sub>2</sub>O<sub>2</sub> and 0.1 % w/v of sodium dodecyl sulfate (SDS) were used systematically in the all experiments as the optimal conditions for the swimming of the GOx-micromotors. Velocities of the micromotors in these conditions averaged at approximately 500  $\mu\text{m s}^{-1}$ . A swarm of approximately  $2 \times 10^5$  GOx-micromotors was deployed in the lead contaminated water (1 ppm) for adsorptive removal. **Figure 34A** shows snapshots from characteristic micromotors swimming in lead-contaminated water at different time periods. Bubble tails released from micromotors indicate the trajectories and displacement of micromotors at initial time, 15, 30 and 60 min respectively.

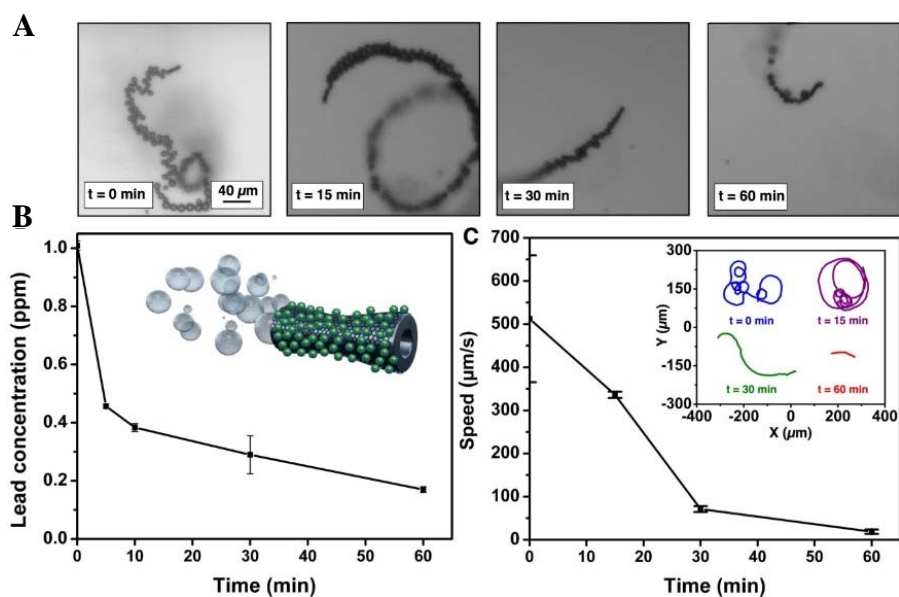


**Figure 34. Kinetics of Pb(II) decontamination and speed for the GOx-micromotors.** (A) Optical snapshots from videos of GOx-micromotors moving at different times during the decontamination process (B) Pb(II) ions concentration at different time intervals during decontamination by GOx-micromotors (inset: illustration of a GOx-micromotor with adsorbed lead (green dots) on the surface after the decontamination process). (C) Speed of GOx-micromotors at different times (0, 15, 30 and 60 min, Inset: trajectories of the GOx-micromotors for 5 seconds). Experimental conditions: 1 ppm as initial Pb(II) concentration, 1.5% v/v of H<sub>2</sub>O<sub>2</sub> and 0.1% w/v SDS.

**Figure 34B** shows the decrease in lead concentration over 60 minutes in the presence of motile GOx-micromotors. The lead concentration was measured using inductively coupled plasma optical emission spectrometry (ICP-OES) which is able to detect traces of metals. In the first 10 minutes, the GOx-micromotors were able to decrease the lead concentration from 1 ppm to lower than 0.4 ppm and in 1 hour the GOx-micromotors were able to remove more than the 80% of lead from the contaminated water. The GOx-micromotors were allowed to swim for 24 hours observing that after this time the concentration of lead was slightly higher ( $0.29 \pm 0.02$  ppm) than it was in one hour ( $0.17 \pm 0.01$  ppm). This could be attributed to the fact that with time, the process of adsorption reaches to a desorption-adsorption equilibrium where desorption phenomenon could also occur. Therefore, 1 hour was selected as the optimal time for the lead remediation from polluted water. **Figure 34C** (inset) displays the tracking of the average speed of the

micromotors for 5 seconds at different times (0, 15, 30 and 60 minutes). When the micromotors were initially added to the lead contaminated solution and 1.5% H<sub>2</sub>O<sub>2</sub> v/v, high velocities and frequent reorientation of trajectories were observed. After 15 minutes, the speed of the micromotors slightly decreased and their trajectories were usually circular or straight. After 30 and 60 minutes, micromotors swam at slower speed compared to their initial values and with less frequent reorientation in the direction of swimming. This swimming behavior was due to the fact that the H<sub>2</sub>O<sub>2</sub> was being consumed continuously from the solution during the catalytic reaction on the inner platinum surface. To demonstrate that the presence of lead does not affect the motor speeds, new fresh H<sub>2</sub>O<sub>2</sub> was added to the slow or non-swimming micromotors that had previously undergone 24 hours of catalytic reaction, which reestablished swimming of micromotors with similar velocities and movements as were observed at the beginning of the experiments.

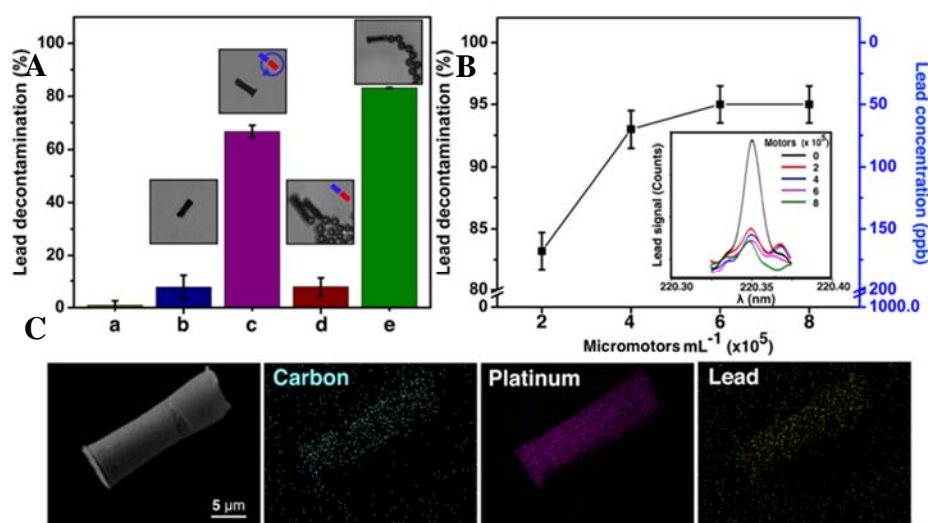


**Figure 35. Pb(II) ions decontamination by GOx-micromotors and characterization of micromotors after decontamination.** (A) Decontamination of Pb(II) ions in different systems: In the presence of (a) H<sub>2</sub>O<sub>2</sub> and of SDS (b) SDS and non-motile GOx- micromotors (c) SDS and GOx-micromotors stirred by external magnets (d) H<sub>2</sub>O<sub>2</sub>, SDS and docked GOx-micromotors (immobilized by stationary magnetic field) and (e) in the presence of H<sub>2</sub>O<sub>2</sub> and SDS motile GOx-micromotors (B) Decontamination of Pb(II) ions for different concentrations of GOx-micromotors in the presence of H<sub>2</sub>O<sub>2</sub> and of SDS. (Inset: ICP-OES signal of lead concentration after decontamination process for increasing amount of motors) (C)

EDX mapping: the SEM image of the analyzed GOx-micromotors after the decontamination process showing, carbon distribution, platinum distribution and Pb(II) distribution.

Several control experiments were carried out to demonstrate that the decontamination process was due to the adsorption on the GOx-micromotors (**Figure 35A**). The decontamination of lead was measured after placing contaminated lead solutions into different experimental conditions. **Figure 35A-a** shows that without the use of micromotors, the lead concentration does not decrease when in contact with the fuel  $\text{H}_2\text{O}_2$  and SDS after 24 hours. **Figure 35A-b** shows minor decontamination of lead when a fixed amount of GOx-micromotors were left in contact with the lead contaminated solution for 1 hour. This was performed without adding  $\text{H}_2\text{O}_2$  in the solution, so that GOx-micromotors could not swim, leading to a low decontamination of lead. The GOx-micromotors were then stirred by rotation of an external magnetic field generated by the magnetic stirrer, as it is represented in the inset in **Figure 35A-c**. Here, micromotors were able to remove  $66.6 \pm 2.4\%$  lead from water. When the GOx-micromotors are rotated at high speed in the solution, the diffusion of lead ions on the micromotors surface is enhanced due to induced micro-convection. This increases the chances of contact between contaminant and micromotors. **Figure 35A-d** displays the decontamination when the bubbled GOx-micromotors left in polluted solution, but their swimming was inhibited by the presence of a strong magnet, which immobilizes them in a fixed location. However, when these GOx-micromotors left free to swim (**Figure 35A-e**), the decontamination process is ten times more effective as it varies from  $7.7 \pm 4.5\%$  (non-motile) to  $83.2 \pm 1.0\%$  (motile). These results reveal the high significance of the synergy between the presence of graphene oxide and self-propulsion of the GOx-micromotors.

Because the lead decontamination is an adsorption process based on the adhesion of lead onto a GOx surface, when the number of GOx-micromotors in the contaminated water was increased, the concentration of lead in the solution decreased as displayed in **Figure 35B**. We doubled the number of micromotors and up to four times the standardized amount of micromotors ( $2 \times 10^5$  micromotors),

resulting in an increase of lead capture from 83.2% to more than 95 % (remaining lead concentration was <50 ppb). The plateau at  $6 \times 10^5$  micromotors, indicates the lead detection limit of the analytical system used for the analysis.

EDX mapping was used to verify the decontamination by GOx-micromotors, which showed the presence of Pb on their surfaces (**Figure 35C**). Lead was not found in EDX mapping performed previous to the decontaminating experiment (**Figure 32B**), which gives direct evidence of adsorption of lead on the surface of the micromotors. The effective adsorption of lead on graphene surface of the GOx-micromotors is based on the strong interactions produced between graphene oxide and Pb (II) ions due to the formation of electron donor–acceptor complexes. The presence of oxygen moieties and delocalized  $\pi$ -electron systems in graphene oxide act as Lewis base and attach to the Pb(II) ions which act as Lewis acid. In addition, this process is strongly dependent on the pH and temperature and independent of ionic strength<sup>111</sup>. We also observed that the structure of the GOx-micromotors was not damaged by the decontamination process maintaining its composition. (**Figure 35C**, SEM image).

We further demonstrate the recovery of lead after its removal from polluted water. **Figure 36A** shows the efficiency of lead recovery after treating GOx-micromotors in different chemical conditions to induce the desorption of Pb(II) from their surfaces. Different aliquots of previously used GOx-micromotors for lead removal were extracted using a magnet, dissolved in 3 mL of different media (**Figure 36A**) and stirred for 1 hour. After the removal of GOx-micromotors from the solution by magnetic control, the remaining solution was analyzed for lead by ICP-OES analysis. When the GOx-micromotors were in presence of water, cold water (temp 4 °C) and basic pH (11), the Pb(II) ion concentration was not detectable at the detection limit of the instrument (50 ppb). However, when the GOx-micromotors were kept in acidic media i.e HCl (pH=1) and HNO<sub>3</sub> (pH=0.3), desorption event reached recoveries up to  $91.2 \pm 4.6\%$  and  $101.0 \pm 3.5\%$ , respectively. The structure of the GOx-micromotors was not significantly affected as it is observed in the inset of

Figure 36A which shows a SEM image of GOx-micromotor after the decontamination and recovery processes.

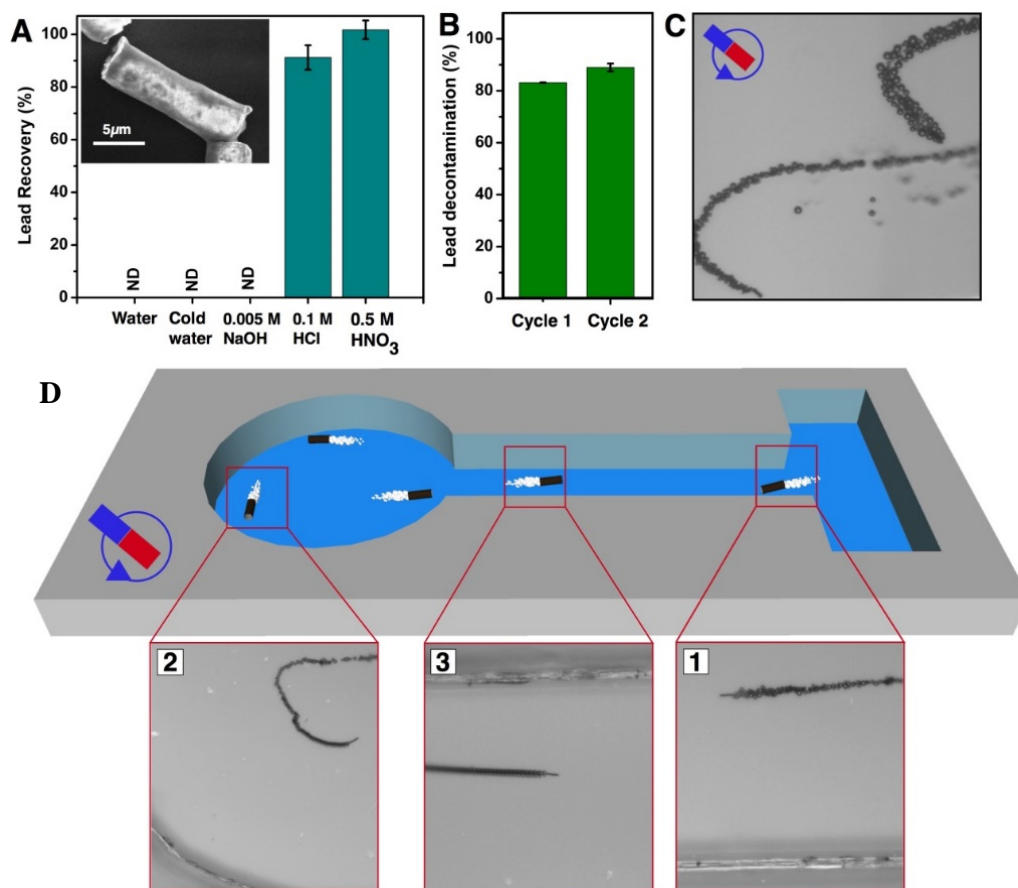


**Figure 36. Lead recovery, reusability of GOx-micromotors and magnetic control of GOx-micromotors.** (A) Recovery of Pb(II) ions from GOx-micromotors after different desorption treatments, which were previously employed in decontamination process. (Inset shows SEM image illustrating GOx-micromotors tube after the decontamination and desorption (with 0.5M HNO<sub>3</sub>) process. (B) Reusability of GOx-micromotors, representing lead decontamination in the first and second cycle. (C) Optical snapshot from a video of GOx-micromotors controlled by magnetic guidance after the lead recovery process. (D) GOx-micromotors controlled by magnetic guidance swimming in a PDMS microchannel as a prototype system.

After cleaning and washing GOx-micromotors, the reusability of GOx-micromotors was studied. The GOx-micromotors were added into the lead contaminated water as in the first decontamination assays. **Figure 36B** represents that the GOx micromotors

retained their lead removal efficiently in the second cycle after removing and recovering lead in the first cycle. Activation of graphene oxide by treatment with the oxidant acids such as nitric acids oxidize the graphene surface and increase the number of oxygen moieties, which mainly interact with Pb(II) ions.

As a proof-of-concept, we tested the capabilities of GOx-micromotors to perform various tasks inside a PDMS microchannel by external magnetic guidance. Since GOx-micromotors contain Ni layer, they are ferromagnetic in nature which allows control of their trajectories by external magnetic field. **Figure 36C** show the trajectory control of GOx-micromotors by using the external magnetic field after the process of Pb(II) decontamination on the surface. **Figure 36D** illustrate a GOx-micromotor guided in the microfluidic channel from the lead contaminated water containing reservoir after decontamination to the other location where lead can be recovered and concentrated for recycling. The ability to magnetically control the micromotors makes it possible to develop and program an automated system to guide swarm of micromotors to accomplish the assigned tasks.

### 3.3. Conclusions

In conclusion, we have demonstrated graphene oxide based micromotors for the efficient removal of toxic heavy metal (Pb) from contaminated water through an adsorption process, the recovery of Pb(II) ions and the subsequent reusability of GOx-micromotors. GOx-micromotors can be deployed in contaminated water to swim randomly and easily be collected using magnets once the water purification process has been completed. As a proof of the concept, magnetic control of GOx-micromotors swimming inside a microfluidic system was demonstrated. GOx-micromotors can be useful as new devices for future decontamination of heavy metals from industrial waste water due to their efficiency for decontamination, their easy removal from the solution and the possibility of lead recovery and their reusability. The use of active systems and graphene nanomaterials can pave the way for new functionalities of self-propelled micro-nanomotors, from drug delivery, sensing, energy to new environmental applications.

### 3.3. Experimental methods

#### 3.3.1. Materials and reagents

Graphene oxide, sodium dodecyl sulfate (SDS), lead nitrate, nitrate acid, hydrochloric acid and sodium hydroxide were purchased from Sigma-Aldrich (Germany). H<sub>2</sub>O<sub>2</sub> 30%, potassium nitrate, methylene chloride and ethanol were purchased from Merck (Germany). Ultrapure water (Millipore Corporation, USA) was used for the preparation of all aqueous solutions.

#### 3.3.2. Fabrication of graphene oxide-based multilayer micromotors

The graphene oxide-based multilayer micromotors were fabricated using a common template directed electrodeposition protocol. A cyclopore polycarbonate membrane, containing 5 μm maximum diameter conical-shaped micropores (Catalog no. 7060-2513; Whatman, Maidstone, UK), was employed as a template. 80 nm gold film was first sputtered (sputter system MED020 Bal-Tec) on one side of the porous membrane to serve as a working electrode using an evaporation and sputtering was performed at room temperature under vacuum of 5x10<sup>-2</sup>Torr, power 60 mA and Ar was flowed during 85s. A Pt wire and an Ag/AgCl with 3 M KCl were used as counter and reference electrodes, respectively. The membrane was then assembled in a plating cell with an aluminum foil serving as contact for the working electrode. A solution which contains 0.1mg/mL graphene oxide (GO<sub>x</sub>) in 0.5M of Na<sub>2</sub>SO<sub>4</sub> and 0.1 M of H<sub>2</sub>SO<sub>4</sub> was prepared from Sigma-Aldrich reagents<sup>1</sup>. The GO<sub>x</sub> of the solution was reduced by using cyclic voltammetry from -1.5V to 0.3V for five cycles. Then, the metallic layers were deposited from a Pt and Ni commercial solutions (Platinum TP; Technic Deutschland GmbH and nickel-100 semiplate; NB Technologies GmbH). Nickel solution was prepared by adding 0.0488 g l-1 SDS to the commercial Ni solution and sonicating using an ultrasound bath for 15 min. The first metallic layer, which uses a 1:1:1 Pt:Ni:water solution, was deposited galvanostatically at -2 mA for 300 s to provide a smooth surface and to improve the deposition of the next metallic layers. After washing three times with water, the Ni

layer was deposited amperometrically at -1.0 V for 2.4 C to achieve the ferromagnetic properties that allows the micromotor guidance by properly orienting the magnetic field created by a simple neodymium magnet. Finally, after other three washings, the catalytic inner Pt layer was deposited galvanostatically at -2 mA for 300 s. To release the GOx-micromotors from the template, the sputtered gold layer was completely removed by mechanical hand polishing with 5  $\mu\text{m}$  alumina slurry (Electron Microscopy Sciences, Hatfield, PA). The membrane was then dissolved in methylene chloride for 10 min to completely release the microtubes. Finally, the micromotors were washed two times more with methylene chloride, followed by ethanol and ultrapure water, two times of each, and collected by centrifugation at 9000 rpm (Eppendorf 3409) for 3 min after each wash.

### 3.3.3. Equipment used for the experiments.

Template electrochemical deposition of microtubes was carried out with using a potentiostat (AUT50101, Metrohm Autolab B.V.). The software used for the electrochemical depositions was NOVA 1.10. An inverted optical microscope (Leica DMI3000B), coupled with a 10X, 20X, 40X and 63X objectives, along with a Leica digital camera DFC3000G with LAS V4.5 soft-ware, were used for capturing movies. Scanning electron microscope (E-beam-SEM Ultra 55 Zeiss) was used for the micromotors characterization. Energy dispersive X-ray analysis (EDX) was carried out using EDAX connected to Cryo-SEM Ultra 55 Zeiss EDAX. Raman analysis and mapping were carried out on a Thermo Scientific DXRTM Raman Microscope with Atlus system. A 532nm laser line with an output power of 5 W was used as the excitation source. The spectra were collected in ranges of 100 to 4000  $\text{cm}^{-1}$  with exposure time of 1 second and 10 $\times$  magnification. All Raman experiments were conducted at room temperature and ambient pressures. X-ray photoelectron spectroscopy (XPS) from SPECS system (Germany) was used to identify functional groups on the GOx-micromotors surface. The instrument was equipped with XR50 duel anode source (Al operated at 150W) and a Phoibos MCD-9 detector. All measurements were done under the vacuum (pressure  $5 \times 10^{-9}$  mBar)

and the hemispherical analyzer was set at the pass energy 25 eV while the high-resolution spectra step size was set at 0.1 eV. Casa XPS program (Casa Software Ltd., UK) was used for the data analysis. Inductively coupled plasma optical emission spectrometry (ICP-OES), was employed as analytical technique for the detection of Pb(II) ions. Origin Pro 9.0 and Microsoft Excel 2010 were employed for the analysis of the experimental data.

#### Experimental procedure

The GOx-micromotors were characterized using different characterization techniques, such as, Raman, SEM and EDX. After characterization, the GOx-micromotors fabricated were transferred together in a falcon tube and they were observed by using an inverted microscope for estimating the concentration of GOx-micromotors in water. Once the GOx-micromotors have been characterized and counted, they were used for decontamination experiments, which are carried out in a glass beaker containing total 3 ml of heavy metal polluted water consisted of 1ppm of lead (1 $\mu$ g/ml or 1000 ppb), H<sub>2</sub>O<sub>2</sub> (1.5% v/v) and SDS (0.1 % w/v) at the pH (5.7). The assay was carried out by triplicate (n=3) for each time (5, 10, 30, 60 min and 24 hours) that the motors are swimming in the contaminated solution. Control experiments were also carried out by triplicate. Swimming of micromotors was recorded at different time interval by inverted microscope and tracking was done by a custom-made python script which used open CV libraries. Lead concentration was measured by ICP-OES and the GOx-micromotors were kept in the glass beakers using a magnet due to their magnetic properties. Then, the GOx-micromotors were washed once with water and characterized by SEM and EDX analysis. After that, they were exposed for 1 hour to different treatments, such as water presence, water presence under low temperature, basic pH, acid pH by using HCl (pH=1) and HNO<sub>3</sub> (pH=0.3) for the lead recovery and washed once with water. The supernatant from these different treatments were measured by ICP-OES to probe the lead content and thus, the lead recovery from the GOx-micromotors. On the other hand, the GOx micromotors were characterized by SEM and EDX and washed several times with water for their reusability. Reusability experiments were carried out following the same conditions of the first lead decontamination and also

by triplicate for 1 hour. After that, the GOx-micromotors were kept in the glass beakers using a magnet and the solutions were measured by ICP-OES.

## CHAPTER 4.

# BACTERIAL DISINFECTION AND REMOVAL USING MICROMOTORS

**The results described in this chapter are published in the following article.**

Vilela, D.; Stanton, M. M.; Parmar, J.; Sánchez, S. Microbots Decorated with Silver Nanoparticles Kill Bacteria in Aqueous Media. *ACS Appl. Mater. Interfaces* **2017**, *9* (27), 22093–22100.

### 4.1. Introduction

Waterborne diseases can have a devastating effect on public health<sup>10</sup>. Current disinfection methods use chemical (free chlorine, chloramines and ozone)<sup>112</sup> and physical disinfectants (UV light,<sup>113,114</sup> electronic radiation<sup>115</sup> and heat<sup>116</sup>). However, the resistance of some pathogens to conventional disinfectants requires the combination of these disinfection methods or higher disinfectant dosages<sup>107</sup> which can react with constituents in natural water forming harmful disinfection byproducts<sup>117</sup>. Therefore, there is an urgent need to develop more effective, innovative, low-cost, robust water cleaning methods, which do not adversely affect the environment or damage human health.

Recently, new bactericidal micromotors<sup>36,118,119</sup> are recently being developed as new efficient tools for cleaning waterborne bacteria because of the increasing threat of antibiotic resistant bacteria and the harmful chemical byproducts generated by conventional water disinfection methods<sup>117</sup>. However, these bactericidal micromotors can produce additional contamination because of the present of their residual structures after bactericidal assay, as they cannot be removed after use.

Alternative methods of bacterial disinfection have used silver in the form of metallic silver and silver ions for the treatment of injuries, wounds, and bacterial infections<sup>120</sup>. Currently, because of the rapid growth of nanotechnology, silver nanoparticles (AgNPs) are widely used in medical<sup>121</sup> and consumer<sup>122</sup> products owing to their potential bactericidal effects<sup>123–127</sup>. AgNPs have an exceptionally large surface area, which improves the contact with microorganisms and results in efficient antimicrobial properties compared to those of other Ag salts<sup>126</sup>. Furthermore, AgNPs can release Ag<sup>+</sup> ions at a desired rate and location depending on their design (size, surface coatings, etc). Thus, AgNPs can be used as the vehicle to efficiently deliver Ag<sup>+</sup> ions into the bacterial cytoplasm. The localized acidic pH of a bacterial membrane<sup>128,129</sup> increases the rate release of Ag<sup>+</sup> ions from AgNPs adhered to the bacteria<sup>123</sup>. Ag is able to bind to thiol groups present in proteins,

disrupting their functionality by compromising the permeability of the bacterial membrane, thereby leading to cell lysis and death<sup>123,130</sup>.

In this chapter, an efficient method for the disinfection and removal of bacteria from contaminated water using AgNPs-coated Janus micromotors self-propelled by the reaction of magnesium (Mg) in water, producing hydrogen (H<sub>2</sub>) bubbles is discussed. The high antibacterial capacity of the developed AgNPs-coated Janus micromotors is the result of two synergistic effects: (i) the enhanced contact killing by the combination of the Janus micromotors self-propulsion and immobilized AgNPs on their surface<sup>131</sup> and (ii) attachment of the bacteria to gold surface.<sup>132,133</sup> Therefore, AgNPs-coated Janus micromotors are able to clean waterborne bacteria within 15 min of swimming in contaminated water. In addition, bacteria trapped and adhered to the micromotors can be removed from the water source using a magnetic field to collect the particles. After swimming of the micromotors and bacterial harvest, the magnetic field can be used to remove the micromotors and captured dead bacteria. Unlike previous reports of microswimmers using toxic fuel sources, such as H<sub>2</sub>O<sub>2</sub>, the Mg-based Janus micromotor is biocompatible, environmentally friendly, and does not produce chemical waste during and after operation.

### 4.2. Results and discussion

AgNPs-coated micromotors are based on four materials: (1) Magnesium (Mg) microparticles (15±5 μm diameter) as a template structure and for self-propulsion, (2) iron (Fe) Janus cap which provides magnetic control, (3) gold (Au) layer on top of Fe layer providing an easily modifiable surface and cell adhesion and (4) AgNPs attached on the Au surface providing antibacterial properties to the micromotors.

The detailed fabrication of the water-propelled, AgNPs-coated Janus micromotors is described in **Figure 37**. As shown, the micromotors' fabrication is carried out by the consequent deposition of Fe and Au on a monolayer of previously cleaned commercial Mg microparticles using an e-beam metal evaporator (**Figure 37A**). After the deposition, Janus microparticles were dispersed in an ethanol solution for the chemical modification of the Au surface using a solution of cysteamine

hydrochloride. Then, AgNPs immobilization is mediated by overnight incubation of the cysteamine modified Janus microparticles in previously synthesized AgNPs solution. A layer of AgNPs is formed on the Au surface of the Janus microparticles due to the interactions between AgNPs and amines (**Figure 37B**)<sup>131,134</sup>.

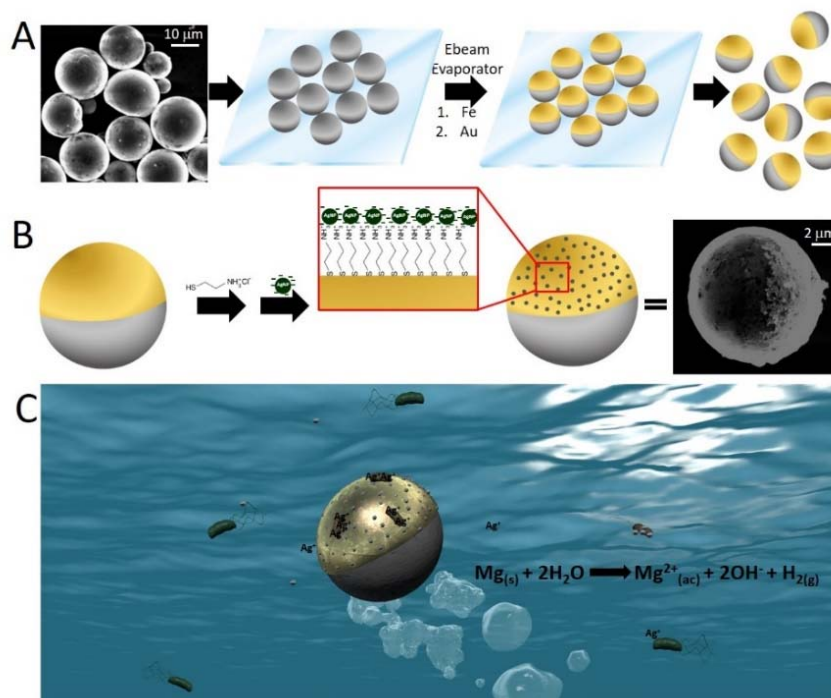


**Figure 37. Fabrication of the AgNPs-coated Janus micromotors.** (A) A monolayer of Mg microparticles was deposited on a glass slide. An e-beam metal evaporator was used for the deposition of 14 nm layer of Fe and 35 nm layer of Au. To obtain free Janus micromotors, short ultrasound pulses in ethanol were applied. (B) Fabrication of the AgNPs-coated Janus micromotors by the modification of the Au surface first with cysteamine hydrochloride and then with previously synthesized AgNPs. (C) Schematic representation of the different possible mechanisms of bactericidal action caused by the water-propelled AgNPs-coated Janus micromotors.

The Janus micromotors are composed of various materials for a multi-functional, environmental remediation system. The Mg microparticle reacts with water producing Mg ions (Mg<sup>2+</sup>), hydroxide ions (OH<sup>-</sup>) and hydrogen gas (H<sub>2</sub>) providing a microbubble propulsion mechanism which exerts enough force that enables the micromotors to swim. The reaction of Mg with water is a spontaneous redox

reaction in which Mg is oxidized and  $H^+$  protons from water molecules are reduced to  $H_2$  (Figure 37C). The inner Fe layer offers the ability for remote guidance and removal of the micromotors using an applied magnetic field. The outer Au layer provides surface chemistry for thiol attachment and subsequent AgNPs modification by electrostatic interactions (Figure 37B) and helps bacteria adhesion. The presence of the AgNPs on the Janus micromotor provides the particles' bactericidal behavior. Figure 37C represents the possible mechanisms of bactericidal action caused by the water-propelled AgNPs-coated Janus micromotors: (i) direct contact with immobilized AgNPs on coated micromotors, (ii) contact with AgNPs that are released from the AgNPs-coated micromotors into the solution as colloids, and (iii) mediated via silver ions released either from colloidal AgNPs in the solution or immobilized nanoparticles.<sup>36,43,46</sup>

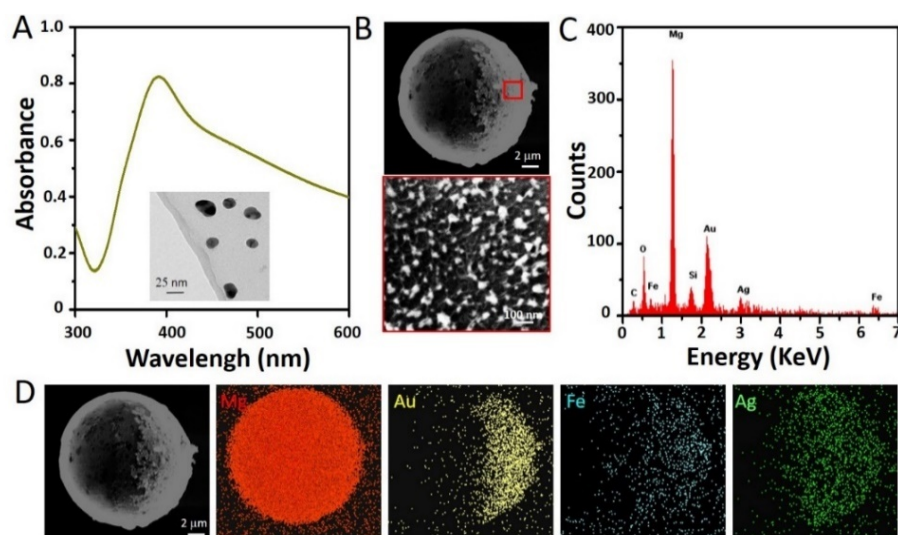


**Figure 38. Characterization of colloidal AgNPs and AgNPs-coated Janus micromotors.** (A) UV-visible spectrum of prepared AgNPs in colloidal solution (inset: TEM images corresponding to AgNPs in colloidal solution). (B) Top panel: SEM image of an AgNPs-coated Janus micromotor; bottom panel: an enlarged SEM image of the Au modified surface with AgNPs. (C) EDX element analysis of an AgNPs-coated Janus micromotor. (D) EDX mapping of the metallic elements of an AgNPs-coated Janus micromotor.

Janus micromotors were characterized by scanning electron microscopy (SEM), energy dispersive X-ray spectroscopy (EDX), UV-Vis spectroscopy, and

transmission electron microscopy (TEM) (**Figure 38**). **Figure 38A** displays the characteristic maximum absorbance peak of AgNPs colloidal aqueous solution at 398 nm in the UV-Visible spectrum. Additionally, the size of the AgNPs in colloidal solution is characterized by TEM (**Figure 38A**, inset) with an observed average diameter of  $23 \pm 6$  nm. **Figure 38B**, C and D illustrate the characterization of AgNPs-coated Janus micromotors using SEM and EDX. In the **Figure 38B** top image, an SEM image shows an AgNPs-coated Janus particle, where the two faces of the particle can be differentiated. The bottom image is a magnified view of a small area of the AgNPs coated Au surface (red square) where AgNPs are visible. **Figure 38C** illustrates the EDX analysis which confirms the metallic components of the AgNPs-coated Janus micromotors, including Mg, Au, Fe and Ag, where Mg is the major component. To show the distribution of these elements are distributed in the Janus micromotor structure, **Figure 38D** displays the mapping of the detected metallic elements performed by EDX analysis. As it can be observed, the bulk of the sphere is Mg since it is the base material of the particle. Only half of the particle, *i.e.* the Janus particle cap, contains Fe, Au and Ag.

To prove the capability of the motion of AgNPs-coated Janus micromotors and consequently, their active behavior as bactericidal tools for water disinfection, their swimming behavior is studied. **Figure 39A** shows the quantification of the speed of the Janus micromotors against a short range of pHs (5.0 – 6.5) of the swimming solution, similar to the pH of drinking water. **Figure 39C** display the traveled distance of AgNPs-coated Janus micromotors at different pHs for 10 seconds. With decreasing pH, the speed of the micromotors as well as their total distance traveled increases. This behavior is due to the increased degradation rate of Mg in acidic aqueous solution, producing increased amounts of H<sub>2</sub>, and consequently, more bubbles, for a greater self-propulsion velocity. Thus, the highest speeds of the micromotors are observed at pH 5.0 ( $26.9 \pm 1.8 \mu\text{m/s}$ ), followed by pH 5.5 ( $14.0 \pm 0.6 \mu\text{m/s}$ ), pH 6.0 ( $12.6 \pm 3.0 \mu\text{m/s}$ ) and pH 6.5 ( $6.2 \pm 1.0 \mu\text{m/s}$ ). The constant consumption of Mg during the reaction limits the life time of the micromotors (**Figure 39D**) and is directly related to the pH of the solution. That is observed in

Figure 39B, where swimming lifetime of the Janus micromotors is shorter in acidic pH compared to micromotors in a more neutral pH.

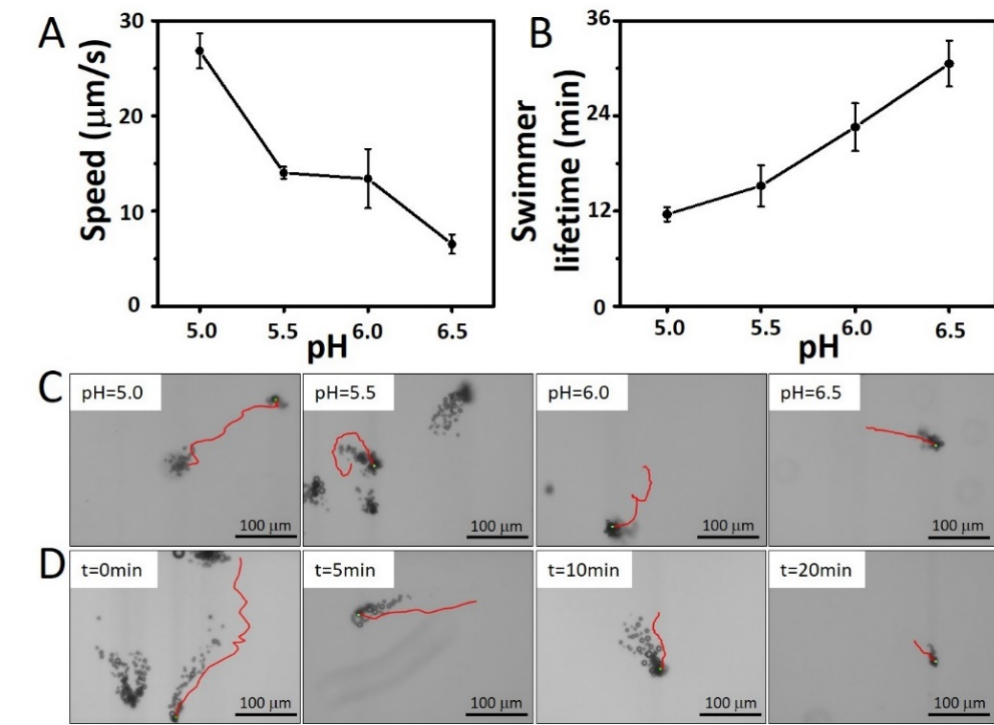


**Figure 39. Swimming behavior of AgNPs-coated Janus micromotors.** (A) Representation of the average velocities of Janus micromotors vs. different pHs, (B) representation of the average lifetime of micromotors vs. different pHs, (C) a AgNPs-coated Janus micromotor swimming over the pH (each image contains 10 s of tracking over pH 5.0, 5.5, 6.0, and 6.5, respectively), (D) a AgNPs-coated Janus micromotor over their swimming lifetime (each image contains 10 s of tracking over 0, 5, 10, and 20 min observation, respectively). Experimental conditions: PBS (pH=6.0) and 2% Tween-20.

Addition of a biocompatible surfactant, such as Tween-20, made the Janus micromotors swim more efficiently, improving their active movement and showing higher efficacy in water solution by reducing the surface tension and producing small bubbles for the propulsion. The speed of the micromotors at different Tween-20 concentrations was studied (Figure 40). The speed of Janus micromotors at pH 6 increased with increased concentration of Tween-20, but after 2% v/v of Tween-20, speeds remained constant. Therefore, to reach a compromise, pH 6 and 2% of Tween-20 were selected as optimal pH and surfactant concentration, respectively,

and 15 minutes as effective swimming time to carry out the remediation of bacteria-contaminated water by AgNPs-coated Janus micromotors.

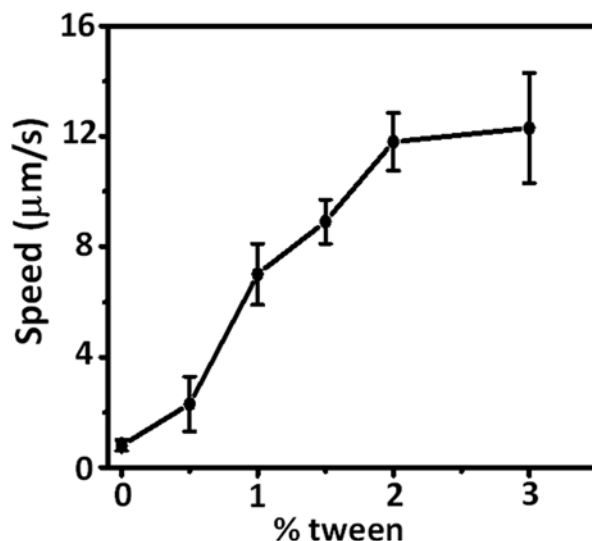
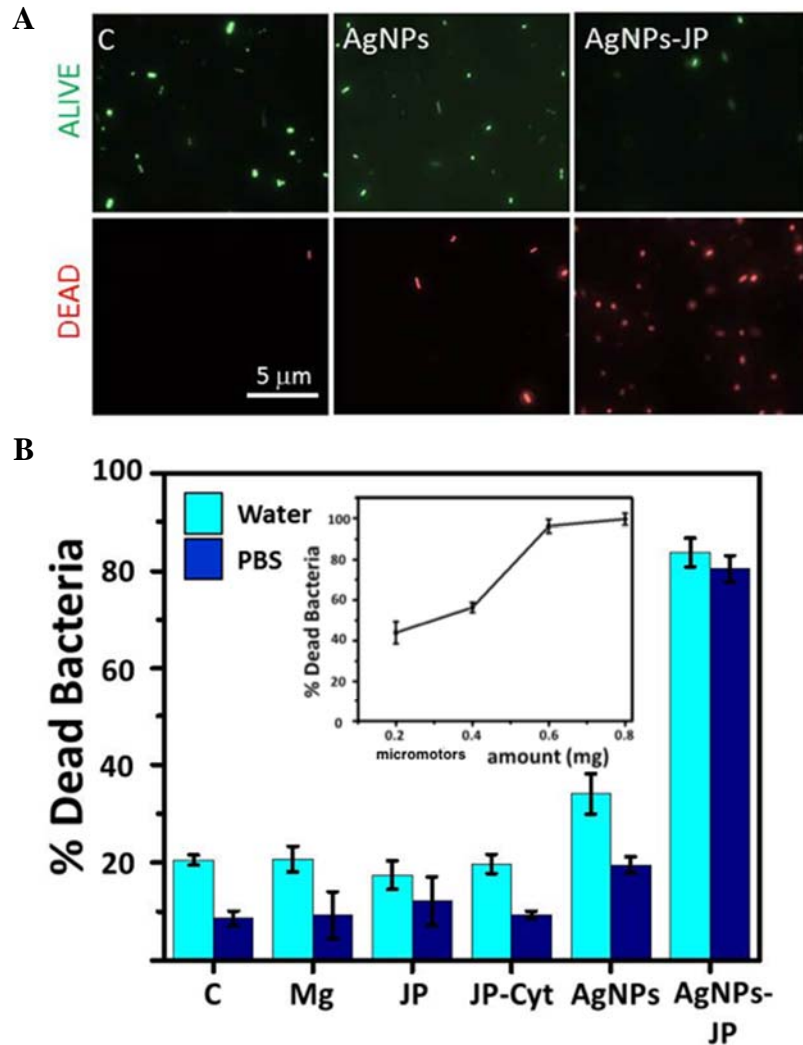


Figure 40. Velocities of AgNPs coated Janus micromotors vs. different tween concentration.

To study the antibacterial capacity of AgNPs-coated Janus micromotors, *E. coli* are used as model bacteria. Also, different control experiments are carried out demonstrating the efficiency of the active AgNPs-coated Janus micromotors approach. *E. coli* are one of the most well studied bacteria and are responsible for many bacterial infections in host organisms ingested from food or water sources being the best biological drinking water indicator for public health protection<sup>135</sup>. Alternative methods are needed to remove these bacteria from water sources to ensure their drinkability. The AgNPs-coated Janus micromotors provide an ideal biocompatible platform for self-propulsion, capture and termination of bacteria, and removal of micromotors with dead bacteria. After the micromotors swam and killed bacteria in solution, they were removed and imaged using fluorescence viability studies and compared to their control groups.



**Figure 41. Bactericidal assay results using AgNPs-coated Janus micromotors.** (A) Optical microscope images of bacteria using fluorescence lamp after bactericidal assays for control solution (B) % Dead *E. coli* after contact with 0.5 mg of Mg microparticles (Mg), Janus microparticles (JP), Cysteamine modified JP (JP-Cyt) and AgNPs-coated micromotors (AgNPs-JP) for 15 min in water pH 6 (cyan) and PBS pH 6 (blue). (Insert) Dead bacteria ratio using different amount of AgNPs-coated Janus micromotors in water.

**Figure 41** shows the antibacterial capability of micromotors in comparison with control assays in PBS and water. The amount of particles were kept the same between each experimental group. The control group with only AgNPs, had the same quantity of AgNPs as the AgNPs-coated Janus micromotors since the

concentration of AgNPs on the surface of the micromotors was estimated during the micromotors fabrication process. The same quantity (w/v) of Mg microparticles was compared to the Au/Fe/Mg Janus particles (JP), and the cysteamine modified Au/Fe/Mg Janus microparticles (JP-Cyt). The groups were studied in the presence of two different medias, water and PBS, at the same pH. As expected, Mg and Janus microparticles (JP and JP-Cyt) are not able to kill bacteria since they do not contain AgNPs. In addition, the hydrogen and ions liberated from the reaction of magnesium with water from these structures does not affect significantly the viability of the bacteria (**Figure 41B**, Mg, JP and Cyt-JP)). Static colloidal AgNPs are also employed as a control, since, as it is well-known, AgNPs interact with the outer membrane of bacteria, causing structural damage that leads to their death.<sup>36-40,43</sup> **Figure 41**, also displays the percentage of dead *E. coli* in presence of AgNPs colloidal solution. AgNPs were able to kill around 25 % of bacteria in PBS and less than 40% in water. This is due to the fact that *E. coli* have higher viability in salt solutions such as PBS. Incubation of *E. coli* in salt free water induces stress on bacteria making them easier to kill. This indicates the presented motors would be highly effective at eliminating bacteria in drinking water that typically has low salt concentrations. The interaction of swimming bacteria with AgNPs and liberated Ag<sup>+</sup> ions in water solutions lead to increased bactericidal activity. However, the bigger bactericidal effect is observed when the bacteria are in contact with AgNPs-coated Janus micromotors which are able to kill more than 80% of *E. coli*. These micromotors swim actively in water solution at pH 6 for more than 15 min (**Figure 39B**) promoting an active contact of AgNPs with bacteria and the diffusion of Ag<sup>+</sup> ions, increasing the bactericidal efficiency of the AgNPs (**Figure 37C**). Furthermore, the influence of micromotors concentration in the efficiency of killing bacteria has been studied. As it is observed in **Figure 41B** (insert), the efficiency of the approach to kill bacteria in contaminated water is directly related to the quantity of AgNPs-coated micromotors in the sample. Thus, depending on the amount of bacterial contamination in water, different concentrations of micromotors could be used to obtain the clean water.

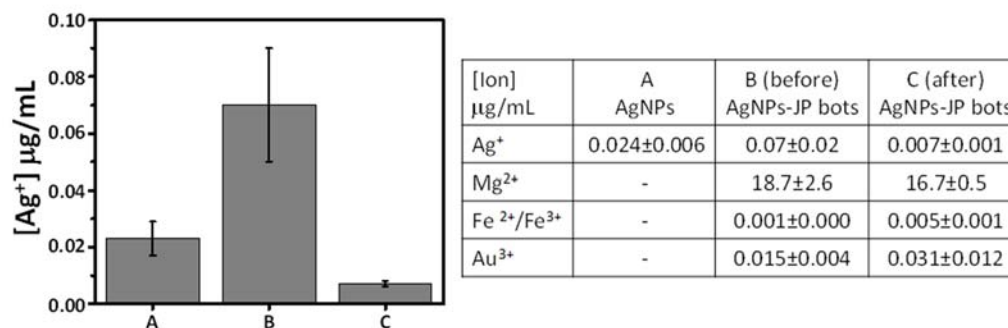


**Figure 42.** Graphic presenting the Ag ions released and a table with the total metallic ions released from. (A) Ag<sup>+</sup> ions released from AgNPs after antibacterial assay, (B) metal ions released from AgNPs-coated micromotors after 15 min in solution (no bacteria presence) and (C) metal ions released from AgNPs micromotors after antibacterial assay. (Table) Release of Mg, Fe and Au ions.

The metallic ions released in solution after AgNPs and AgNPs-coated Janus micromotors were used for removing bacteria (Figure 42A and C) have been analyzed and compared with the ions released from AgNPs-coated Janus micromotors that were not exposed to *E. coli*. (Figure 42B). It is observed that the higher amount of released ions corresponds to Mg<sup>2+</sup> (less than 20 µg/mL) since the metallic Mg structure is consumed during time in contact with aqueous solution (Figure 42, Table). Ag<sup>+</sup> ion concentration in solution was 3-folds higher for AgNPs (0.024±0.006 µg/mL) than for the micromotors (0.007±0.001 µg/mL) in the presence of bacteria. However, when the AgNPs-coated micromotors swam in the absence of bacteria, the release was 10-folds higher than the analogous assay with bacteria (0.07±0.02 µg/mL). That fact could elucidate the predominant mechanism of killing bacteria and the higher efficiency obtained using AgNPs-coated Janus micromotors. Regarding the other ions that may be released from the AgNPs-coated micromotors to the solution during the bactericidal assay, the concentration the released Mg ions was between the values recommended by the World Health Organization (WHO) for drinking water (10-50 mg/mL) and the concentration of Fe ion released was below the allowed WHO concentration (0.3 mg/mL). Currently there is no existing reference value for gold ions. Thus, the effective water

disinfection carried out by AgNPs-coated Janus micromotors may be caused by: (i) the  $\text{Ag}^+$  ions efficiently released from AgNPs attached on the micromotors into bacterial cytoplasm because of the local lower pH of the bacteria membrane<sup>36</sup> and (ii) the enhancement of the killing contact of immobilized AgNPs with bacteria and the self-mixing provoked by self-propelled micromotors. According to the WHO, the level of  $\text{Ag}^+$  in drinking water is  $0.005 \mu\text{g}/\text{mL}$  whereas that the drinking water sources with bacteria is up to  $0.1 \mu\text{g}/\text{mL}$ . The presented micromotors releases  $\text{Ag}^+$  concentrations, with or without bacteria, well within this range.

It has been previously demonstrated that bacteria display preferential adhesion to metals<sup>47,48</sup> and that the negative charge of their cell wall favors their interactions with positive charged surfaces by van der Waals and electrostatic forces<sup>136,137</sup>. Thus, these interactions promote, in this case, the adhesion to the Au cap where the AgNPs are attached (**Figure 43** and **Figure 44**). The adhesion of bacteria to the AgNPs modified Au surface and the low z-potential that the synthesized AgNPs (PVP-capped AgNPs, z-potential=  $-10 \text{ mV}$ )<sup>138</sup> favor the mortality of bacteria and their posterior removal from the solution by the removal of the residual micromotor structures after the antibacterial assay. **Figure 43** confirms the adhesion of bacteria in water and PBS to the metal surfaces of the AgNPs-coated Janus micromotors (B and D), but also on the surface of the Au/Fe/Mg Janus microparticles (A and C). Bacteria attached to the non AgNPs-coated Au surface (**Figure 43A** and C) are mostly alive bacteria, as observed in the fluorescence microscope by green emission. However, the bacteria attached on the AgNPs-coated gold surface of the micromotors are mostly dead (red color) (**Figure 43B** and D).

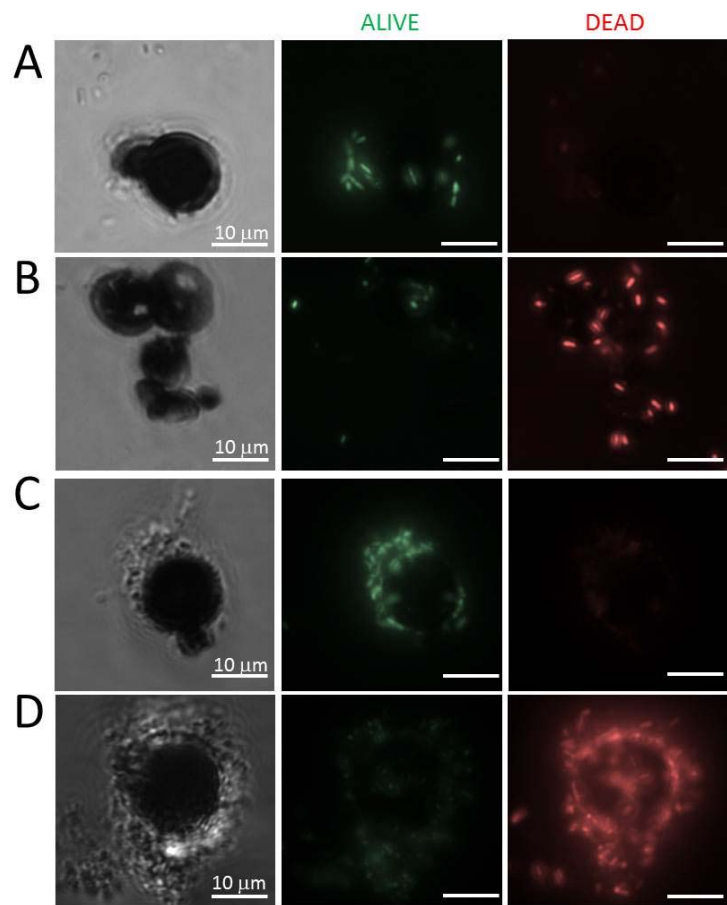


**Figure 43. Bacteria captured onto AgNPs-coated Janus micromotors after bactericidal assay.** Images corresponding to captured bacteria in PBS on (A) Au/Fe/Mg Janus microparticles (JP) and (B) AgNPs-coated Janus micromotors (AgNPs-JP). Images corresponding to captured bacteria in water on (C) Au/Fe/Mg Janus microparticles (JP) and (D) AgNPs-coated Janus micromotors (AgNPs-JP). (Note all images have same scale bar).

As the micromotors contain Fe as a sandwiched material (Au/Fe/Mg) on the particle, AgNPs coated Janus micromotors are capable to remove the bacteria from contaminated solutions using their magnetic properties. **Figure 44A** displays a micromotor externally guided using a simple permanent neodymium magnet. The micromotor swims following the applied magnetic field and can also alter its direction upon changes in the magnetic field orientation similarly to other previously reported Janus micromotors<sup>139,140</sup>. **Figure 44B** shows an immobilized

micromotor during bactericidal assay. As it is marked by the yellow arrows, bacteria are attached on the Au surface modified with AgNPs which helps to kill bacteria and remove them from the solution.

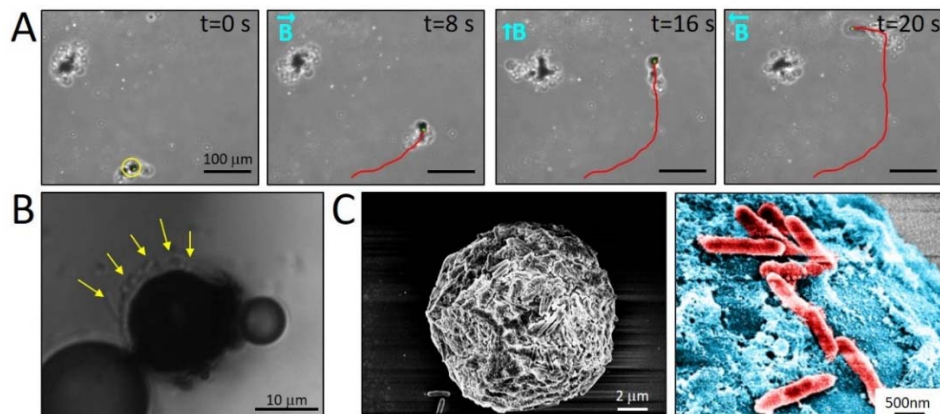


**Figure 44. Magnetic and bacteria adhesion properties of AgNPs-coated Janus micromotors.** (A) Magnetic control of AgNPs-coated Janus micromotors using an external magnetic field. (B) Optical image of bacteria attachment on an immobilized AgNPs-coated Janus micromotor during bactericidal assay. (C) Left: top view of a cap from a Janus micromotor after cleaning water assay and right: close view of the attached *E. coli* (red) on the Au surface of Janus micromotors (blue).

After the removal of bacteria by magnetic attraction of the micromotors, they were observed by SEM (Figure 44C). SEM images confirm that the residual micromotor surface is fully covered by bacteria. Attachment of bacteria to different metals has been previously reported, where guided bacteria adhesion was exploited for creating swimming biohybrids,<sup>48</sup> but here the metal cap has dual capabilities of capturing bacteria and then killing them. The magnetic properties of the cap allow them to be removed from solution with the captured, dead *E. coli* making the micromotor optimal for water purification applications.

### 4.3. Conclusions

We demonstrated that Janus micromotors decorated with silver nanoparticles are an efficient bactericidal tool for water disinfection. Janus micromotors are self-propelled in water and contain a layer of iron which provides magnetic properties.

Thus, differently from the previous reported magnesium based micromotors, AgNPs-coated Janus micromotors can be used to control their swimming and to remove them after their use from the clean solution using external magnets. Such controls can help to achieve targeted attack of micromotors on specific sites and to avoid additional contaminants in solution. The high antibacterial efficiency of micromotors can be explained by mainly two properties of the micromotors: (i) active motion of micromotors, which let the micromotors to travel around and improve the chances of contact of surface decorated AgNPs with the bacteria as well as their self-propulsion, which can increase the diffusion of  $\text{Ag}^+$  ions released from the AgNPs, and (ii) the capacity of the bacteria to attach on the AgNPs-coated Janus micromotors after contact, which provokes a major effect and speed in killing bacteria by the selective  $\text{Ag}^+$  released. We have proved the successful combination of active systems and nanomaterials to develop new micromotors for the cleaning of waterborne bacteria from contaminated water.

### 4.4. Experimental methods

#### 4.4.1. Materials and reagents

Silver nitrate, sodium borohydride, polyvinylpyrrolidone (PVP), cysteamine hydrochloride, disodium hydrogen phosphate, sodium chloride, potassium chloride, potassium dihydrogen phosphate, chloridric acid, sodium hydroxide and tween were purchased from Sigma-Aldrich (Germany). Acetone, isopropanol and ethanol were purchased from Merck (Germany). Ultrapure water (Millipore Corporation, USA) was used for the preparation of aqueous solutions.

#### 4.4.2. Equipment

Janus particles fabrication was carried out using an in-house built electron-beam (e-beam) deposition system. A spectrophotometer Specord 50/plus (Analytik Jena, Germany) was employed to characterize the synthesized AgNPs and estimate their amount attached to the surface of the modified Janus particles. An inverted optical

microscope (Leica DMI3000B), coupled with a 10X, 20X, 40X and 63X objectives, along with a Leica digital camera DFC3000G with LAS V4.5 soft-ware, were used for capturing movies. Scanning electron microscope (E-beam-SEM Ultra 55 Zeiss) was used for the AgNPs-coated Janus micromotor characterization and the visualization of the attached bacteria on the cap structure. Energy dispersive X-ray analysis (EDX) was carried out using EDAX connected to Cryo-SEM Ultra 55 Zeiss EDAX. Bright field images from AgNPs were recorded using a transmission electronic microscope (TEM) Zeiss EM 912 Omega from NORAN. Inductively coupled plasma optical emission spectrometry (ICP-OES), was employed as the analytical technique for the detection of trace metals (Mg, Ag, Fe and Au). Origin Pro 9.0, Microsoft Excel 2013 and ImageJ were employed for the analysis of the experimental data.

### 4.4.3. Synthesis of AgNPs

Silver nanoparticles (AgNPs) were fabricated by reduction of silver nitrate with  $\text{NaBH}_4$  in presence of PVP as stabilizer<sup>1</sup>. Prior to the preparation of AgNPs, all necessary glasswares were cleaned using freshly prepared aqua regia, rinsed thoroughly in water, and dried in the air for 24 hours. An Erlenmeyer flask with 10 mL of 0.02 M  $\text{NaBH}_4$  and 10 mL of 0.375 M PVP was placed in an ice bath with constant stirring for 20 min. Then, 10 mL of 0.02 M  $\text{AgNO}_3$  solution was added dropwise into the solution until the solution became vivid dark yellow. The AgNP colloidal solution was washed three times in ethanol by centrifugation at 13000 rpm for 10 min. AgNPs were characterized carrying out their UV-Visible spectrum and by TEM. The average size of the diameter of synthesized AgNPs was  $23 \pm 6$  nm.

### 4.4.4. Synthesis of Janus microparticles

Commercial magnesium microparticles (catalog #FMW20, TangShan WeiHao Magnesium Powder Co.;  $20 \pm 5$   $\mu\text{m}$ ) were dispersed in ethanol (Ethanol absolute,  $\geq 99.8\%$  (GC)) and then filtered twice using cyclopore etched membranes with 12  $\mu\text{m}$  pore size (7034572, Whatman) using Millipore vacuum pump (XF5423050,

230V/50Hz) to remove all small particles and impurities. Janus particles were obtained by drop casting of a suspension of the previous filtered spherical magnesium microparticles ( $15 \pm 5 \mu\text{m}$ ) in ethanol on an oxygen-plasma-cleaned glass slide followed by slow evaporation of the solvent and placed in an electron beam evaporation system. The high vacuum was applied and subsequently a monolayer of 14 nm Fe was evaporated to obtain magnetic properties and 36 nm Au for further surface modifications. To release particles from the glass slides into ethanol, short ultrasound pulses were sufficient. Afterwards, the Janus particles were cleaned twice in ethanol. Previously fabricated Janus microparticles were incubated overnight with a 1 mM cysteamine hydrochloride in ethanol solution overnight. The microparticles were washed with ethanol and incubated for 24 hours with a diluted solution of the previously prepared AgNPs in ethanol. Afterwards, the AgNPs-coated Janus micromotors were washed twice and stored in ethanol.

### 4.4.5. Bacteria Culture

*Escherichia coli* (E. coli) MG1655 cultured on LB agar plates (Sigma-Aldrich) were transferred to 5 mL LB broth (Sigma-Aldrich) and allowed to divide overnight at 30°C and 200 rpm. 0.5 mL of concentrated MG1655 solution was diluted in 5 mL of fresh LB broth and allowed to culture another 3 hrs. Bacteria were centrifuged (6000 rpm, 3 min) and resuspended twice in PBS (pH 6.5) or deionized water. Bacteria were diluted by a factor of 10 with water or PBS for experimentation. Their measured optical density at 600 nm (OD600) using a BioTek (Bad Friedrichshall, Germany) Gen5 Synergy 2 plate reader was 0.3. The OD600 was obtained from 200  $\mu\text{L}$  of media with bacteria in a 96-well plate at ambient temperature with bacteria free deionized water for a control.

Bacteria on micromotors were imaged with a Zeiss Ultra 55 Gemini scanning electron microscope (SEM) using an accelerating voltage of 5 keV and an in-lens detector. To prepare samples for SEM, biohybrids suspended in motility media were allowed to sediment on clean, plasma etched (1 min argon plasma, Diener Electronic Atto Plasma Cleaner, Ebhausen, Germany) silicon wafer chips (5 x 6

mm) for 1 hr at ambient temperature. Wafers were incubated in 2.5% glutaraldehyde in PBS for 45 min at 4 °C, rinsed with PBS, then water. Bacteria were dehydrated in a series of increasing aqueous ethanol concentrations (30%, 50%, 70%, 90%, and 100%) for 5 min in each solution and 10 min in pure ethanol. Bacteria were further dehydrated and preserved using a series of hexamethyldisilazane (HMDS, Sigma-Aldrich) solutions; 2:1 Ethanol:HMDS (15 min), 1:2 Ethanol: HMDS (15 min), pure HMDS (15 min). Wafers and bacteria air dried followed by sputtering deposition of 3 nm gold using a Bal-tec MED 020 coating system (Leica).

### 4.4.5. Experimental procedures

The AgNPs-coated Janus micromotors were prepared by following the previous protocol. Then, the AgNPs-coated Janus micromotors were characterized using different characterization techniques, such as, SEM and EDX. After characterization, the AgNPs-coated Janus micromotors were transferred together in a falcon tube, most of the solvent was removed and they were dried at room temperature over 2 hours to be divided into several aliquots of 0.5 mg ( $1.11 \times 10^5 \pm 3.8 \times 10^4$ ). The same protocol was carried out to the controls (magnesium microparticles, Fe/Mg Janus microparticles and Au/Mg Janus microparticles).

Once the AgNPs-coated Janus micromotors have been characterized and weighed, their bactericidal activity was tested. Each aliquot of 0.5mg of AgNPs-coated Janus micromotors were placed in petri dishes containing total 2 ml of bacteria in water or PBS and tween (2.0 % w/v) at the pH (6.0). The assay was carried out in triplicate ( $n=3$ ) for 15 minutes while the micromotors were swimming in the bacteria solution. Each control experiment was also carried out in triplicate. Micromotors were removed from the solution using neodymium (NdFeB) magnet. The bacteria present in the solution and the bacteria attached to the cap of the micromotors were washed and re-suspended in fresh deionized water. Samples were incubated with 1  $\mu\text{L}/\text{mL}$  of propidium iodide and STYO 9 (Life Technologies) for 10 min with gentle shaking. Then, they were centrifuged, washed twice with PBS (pH 6.5), and

immediately imaged with a fluorescent microscope. Percent cell viability was defined as the total number of live cells divided by the sum of live and dead cells using Image J software.

To measure the amount of residual metals ions (Mg, Ag, Fe and Au) left in the solution after antibacterial assay, 0.5 mg of AgNPs-coated Janus particles were placed in a water solution (2% tween, pH 6) for 15 minutes in triplicated. Then, the solutions with without micromotors were analyzed using ICP-OES.

## CHAPTER 5.

# MULTIFUNCTIONAL MICROMOTORS AND SCALABLE SYNTHESIS

**The results described in this chapter are published in the following articles.**

(Section 5.1)

Villa, K.; Parmar, J.; Vilela, D.; Sánchez, S. Metal-Oxide-Based Microjets for the Simultaneous Removal of Organic Pollutants and Heavy Metals. *ACS Appl. Mater. Interfaces* **2018**, *10* (24), 20478–20486.

(Section 5.2)

Parmar, J.; Villa, K.; Vilela, D.; Sánchez, S. Platinum-Free Cobalt Ferrite Based Micromotors for Antibiotic Removal. *Appl. Mater. Today* **2017**, *9*, 605–611.

## 5.1. Multifunctional photocatalytic micromotors

### 5.1.1. Introduction

Tubular micro- and nanomotors are usually fabricated by polycarbonate-template-assisted electrodeposition,<sup>23</sup> self-assembly of organic molecules<sup>24,25</sup> and rolled-up nanotechnologies.<sup>26</sup> These methods lead to micro- and nanomotors with a precise geometry and controlled shape. However, specialized equipment such as metal evaporators, cleanroom facilities for lithography process or electrochemical workstations is required to use these technologies.<sup>27,28</sup> Therefore, there is a need for the development of facile synthesis of micro- and nanomotors that involves only basic and inexpensive equipment.<sup>29</sup> Some efforts have been made to develop other simple methodologies for the synthesis of micro- and nanomotors, by using emulsions,<sup>30</sup> microfluidics<sup>31,32</sup> or by simple aggregation processes,<sup>33</sup> but tubular motors cannot be obtained easily by such procedures. Our group has recently reported the fabrication of tubular mesoporous silica micromotors by sol-gel synthesis using a polycarbonate membrane as a template, which uses platinum as catalyst for the self-propulsion in H<sub>2</sub>O<sub>2</sub>.<sup>34</sup> In order to reduce the cost associated with large-scale micromotors synthesis and solve platinum poisoning under harsh chemical environments, micromotors based on metal oxide catalysts have previously been proposed as inexpensive materials for the propulsion of micromotors, but the resulting speeds are still too low.<sup>30,33,35-38</sup>

Previous research has demonstrated the potential of combining the self-propulsion of micromotors with advanced oxidation processes (AOPs) such as Fenton<sup>11,39</sup> reactions and photocatalysis<sup>17,40,41</sup> for environmental remediation. Photocatalytic processes are environmentally-friendly and offer the possibility of using solar radiation as the main energy source, which significantly decreases the cost of water treatments<sup>2,42-44</sup>. Considering that the visible region is one of the major components of solar irradiation, the development of photocatalytic and Fenton-like micromotors

that can harvest solar irradiation to remove different kind of pollutants has the potential to advance micromotors-based water cleaning methods.

Here, we present multifunctional mesoporous silica-based micromotors with  $\text{MnO}_2$  immobilized on the inner surface and decorated with  $\gamma\text{-Fe}_2\text{O}_3$  nanoparticles (NPs) (band gap of  $\sim 2.0$  eV)<sup>45</sup> as magnetic photocatalyst on the outer surface, hereafter called  $\text{FeSiMnO}_x$  micromotors ( $\text{Fe}_2\text{O}_3/\text{SiO}_2\text{-MnO}_2$  micromotors).  $\text{FeSiMnO}_x$  micromotors are fabricated by growing silica tubes on a polycarbonate template by sol-gel method. The immobilized  $\text{MnO}_2$  and  $\text{Fe}_2\text{O}_3$  catalysts act as functional materials for both propulsion and removal of pollutants. Furthermore, the  $\text{FeSiMnO}_x$  micromotors are magnetically steered and guided in a controlled manner, facilitating their recovery and further reuse.

### 5.1.2. Results and Discussions

$\text{FeSiMnO}_x$  micromotors were synthesized by facile and scalable procedures as shown in **Figure 45**. The tubular structure was achieved by using a polycarbonate (PC) membrane as template and a mixture of  $\text{SiO}_2$  precursors at  $80^\circ\text{C}$ .<sup>34</sup> Then, 10 mM  $\text{KMnO}_4$  was reduced to  $\text{MnO}_2$  inside the pores of the membrane by a hydrothermal reaction. After releasing the tubes from the PC membrane,  $\gamma\text{-Fe}_2\text{O}_3$  NPs were mixed with  $\text{SiO}_2\text{-MnO}_2$ -based microtubes and attached to their outer surface. The final tubular structure consists of a biconical mesoporous silica tube with  $\text{MnO}_2$  inner layer and  $\gamma\text{-Fe}_2\text{O}_3$  NPs on the outer surface (**Figure 45**).

The structural and morphological characterization of the micromotors was carried out by TEM-EDX-mapping and SEM, respectively (**Figure 46**). The SEM images show that the micromotors have a tubular biconical structure (see blue inset) with a length of about  $17\ \mu\text{m}$  (**Figure 46A**). The length of the micromotor is co-related with the thickness of the PC membrane ( $20\ \mu\text{m}$ ) used for the synthesis process. The TEM image in **Figure 46B** shows a color contrast along the  $\text{SiMnO}_x$  tube due to the non-homogeneous dispersion of  $\text{MnO}_2$  on the inner surface. This heterogeneity in the inner surface of the micromotors may result in several nucleation points for bubble growth, which can be beneficial for the micromotors motion.

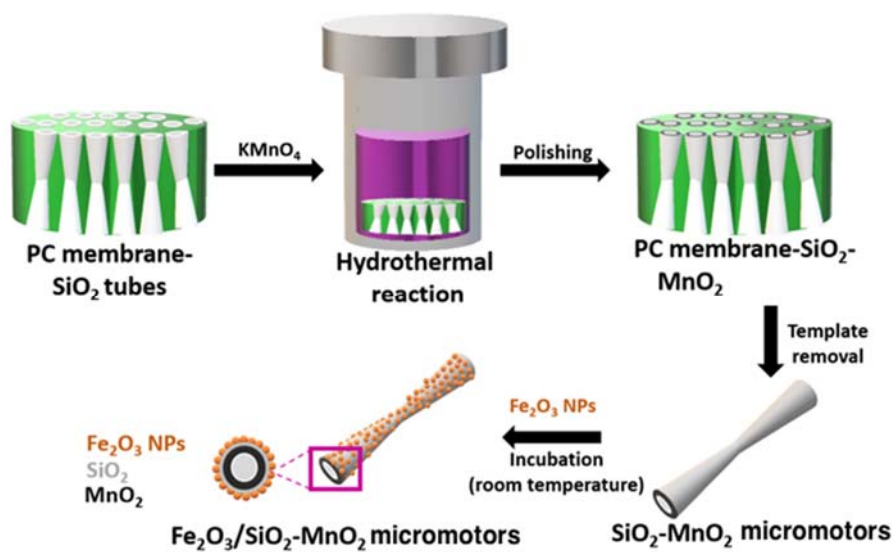


**Figure 45.** Chemical fabrication of mesoporous  $\text{Fe}_2\text{O}_3/\text{SiO}_2\text{-MnO}_2$  ( $\text{FeSiMnO}_x$ ) micromotors for the photocatalytic degradation of organic pollutants and removal of heavy metals.

After the modification of the outer surface of the  $\text{SiMnO}_x$  micromotors with  $\gamma\text{-Fe}_2\text{O}_3$  NPs, it is observed that the  $\gamma\text{-Fe}_2\text{O}_3$  NPs are distributed along the surface (Figure 46C and red dotted inset) and on the edges of the cavity of the  $\text{FeSiMnO}_x$  micromotors (see blue square inset in Figure 46C). Figure 46D displays the rough outer surface of the  $\text{FeSiMnO}_x$  micromotors. This results from the adherence of  $\gamma\text{-Fe}_2\text{O}_3$  NPs to the silica surface, due to the electrostatic interaction between the external  $-\text{NH}_2$  groups from the  $\text{SiO}_2$  tubes surface and the negative charge of  $\gamma\text{-Fe}_2\text{O}_3$  NPs ( $-7.43 \pm 1.53$  mV, average  $\pm$  standard error of mean,  $n = 6$ ) measured by DLS. As observed in Figure 2E, these  $\gamma\text{-Fe}_2\text{O}_3$  NPs have a diameter size ranging from 20-50 nm. The TEM-EDX spectrum confirms the presence of Si, Fe and Mn in  $\text{FeSiMnO}_x$  micromotors (Figure 46F). Furthermore, EDX mapping and the profile analysis of the tubes for the different elements show the distribution of Mn in the tubes and the dispersion of  $\text{Fe}_2\text{O}_3$  NPs along their surface (Figure 46G and H).

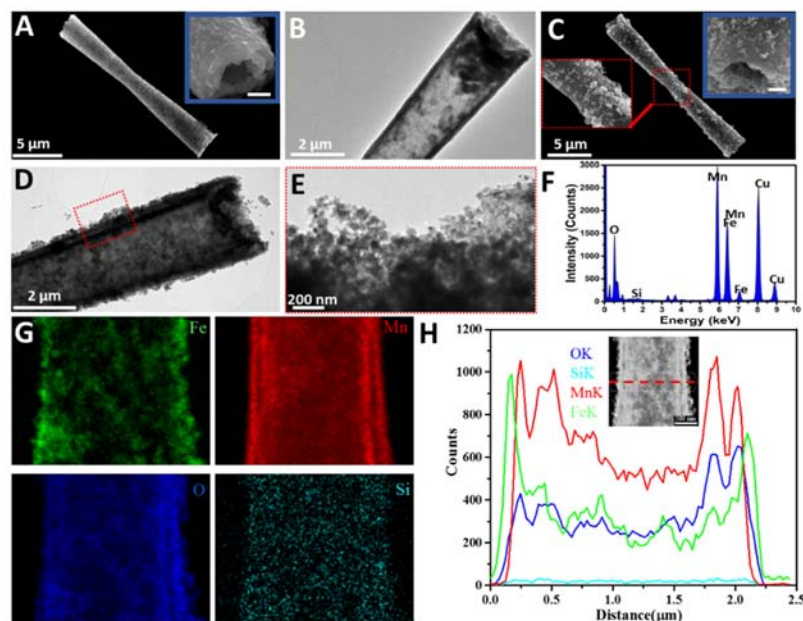


**Figure 46. Characterization of FeSiMnO<sub>x</sub> micromotors.** A) SEM image of the SiMnO<sub>x</sub> micromotor, inset corresponding to the cavity of the tube, B) TEM image of the SiMnO<sub>x</sub> micromotor, C) SEM image of the FeSiMnO<sub>x</sub> micromotor, blue solid inset corresponding to the tube cavity and red dotted inset corresponding to  $\gamma$ -Fe<sub>2</sub>O<sub>3</sub> NPs on the outer surface, D) TEM image of the FeSiMnO<sub>x</sub> micromotor, E) Magnification of the red dotted lines in Figure 2D, F) EDX spectrum of the FeSiMnO<sub>x</sub> micromotor, G) EDX mapping of the FeSiMnO<sub>x</sub> micromotor and H) element profile of the FeSiMnO<sub>x</sub> (represented by a red dotted line).

The mechanism of propulsion of FeSiMnO<sub>x</sub> micromotors is based on the catalytic decomposition of H<sub>2</sub>O<sub>2</sub> into water and oxygen gas by MnO<sub>2</sub>, leading to the generation of microbubbles in their cavity. The motion capabilities of FeSiMnO<sub>x</sub> and SiMnO<sub>x</sub> micromotors were examined using an optical microscope. To find out the relation between MnO<sub>2</sub> loading and motion of SiMnO<sub>x</sub> micromotors, different concentrations of KMnO<sub>4</sub> (10-30 mM) were studied. An increase of KMnO<sub>4</sub> concentration (>10 mM) resulted in a total blockage of the internal holes of the micromotors and/or rupture of the tubular structure in half. As a result, not all the microtubes were swimming, and if they were their speed was very low. Therefore, 10 mM KMnO<sub>4</sub> was selected as the optimal concentration for the synthesis of SiMnO<sub>x</sub> and FeSiMnO<sub>x</sub> micromotors.

Figure 47A shows the motion behavior of  $\text{SiMnO}_x$  and  $\text{FeSiMnO}_x$  micromotors in 5 wt%  $\text{H}_2\text{O}_2$  and 0.2 wt% of SDS. Both micromotors display directional trajectories, but  $\text{FeSiMnO}_x$  micromotors show a faster speed than  $\text{SiMnO}_x$ . This improvement in the speed of  $\text{FeSiMnO}_x$  micromotors is related to the presence of  $\gamma\text{-Fe}_2\text{O}_3$  NPs, which can also catalyze the decomposition of  $\text{H}_2\text{O}_2$  into  $\text{O}_2$  gas through a series of complex reactions.<sup>47–49</sup> The agglomeration of  $\gamma\text{-Fe}_2\text{O}_3$  NPs on the tubes surface might be beneficial for the enhancement of the propulsion of  $\text{FeSiMnO}_x$  micromotors.

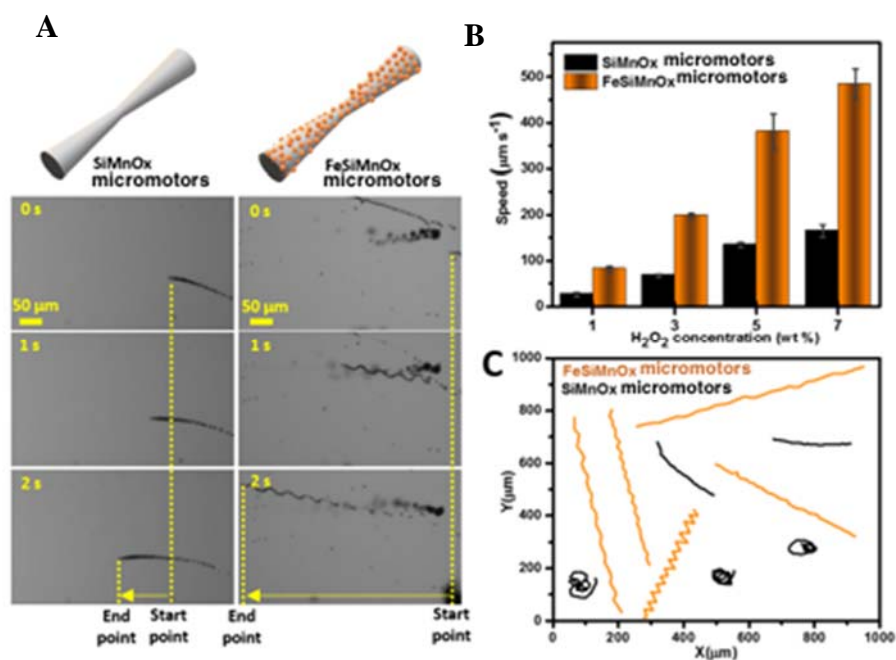


**Figure 47. Motion characterization of  $\text{FeSiMnO}_x$  micromotors.** A) Optical images of the trajectories of  $\text{SiMnO}_x$  and  $\text{FeSiMnO}_x$  micromotors swimming for 2 s at 5 wt%  $\text{H}_2\text{O}_2$ , B) speed of the  $\text{SiMnO}_x$  and  $\text{FeSiMnO}_x$  micromotors at different  $\text{H}_2\text{O}_2$  concentrations ( $n=5$ , error bars represent the standard error of the mean) and C) Swimming trajectories of  $\text{SiMnO}_x$  and  $\text{FeSiMnO}_x$  micromotors at 5 wt%  $\text{H}_2\text{O}_2$ .

Figure 47B illustrates the speed of  $\text{SiMnO}_x$  and  $\text{FeSiMnO}_x$  micromotors at different  $\text{H}_2\text{O}_2$  concentrations (1, 3, 5 and 7 wt%). The speed of the jets increases by increasing the fuel concentration, reaching the highest values at 7 wt%  $\text{H}_2\text{O}_2$  of  $165 \pm 13 \mu\text{m s}^{-1}$  and  $485 \pm 32 \mu\text{m s}^{-1}$  for  $\text{SiMnO}_x$  and  $\text{FeSiMnO}_x$  micromotors

respectively. FeSiMnO<sub>x</sub> micromotors are almost 3 times faster than the bare SiMnO<sub>x</sub>, swimming at approximately 28 body length s<sup>-1</sup> at 7 wt% H<sub>2</sub>O<sub>2</sub>. As depicted in **Table 3**, the speed showed by FeSiMnO<sub>x</sub> micromotors is the highest reported so far for tubular micromotors propelled by non-metallic catalysts. The trajectories of the SiMnO<sub>x</sub> and FeSiMnO<sub>x</sub> micromotors are shown in **Figure 47C**. It was observed that FeSiMnO<sub>x</sub> and SiMnO<sub>x</sub> micromotors move randomly following helical or straight paths.

**Table 3. Speed comparison of different micromotors propelled by non-metallic catalysts.**

Materials in micromotors	Shape	[H <sub>2</sub> O <sub>2</sub> ] (% wt)	Speed (μm s <sup>-1</sup> )	Approximate Body-length s <sup>-1</sup>	Ref.
PEDOT/MnO <sub>2</sub>	Tube	5	200±80	16	141
Fullerene-MnO <sub>2</sub>	Tube	5	39±5	---	142
MnO <sub>2</sub>	Amorphous	12	~50	10	142
Graphene/MnO <sub>2</sub>	Tube	5	210.4±80.4	21	143
Graphene/MnO <sub>2</sub>	Alveolate	2.5	47.92	7.4	144
PEDOT/MnO <sub>2</sub>	tube	6	~125	15.6	145
MOF/Co	Amorphous	5	~25	5	146
MOF/Mn	Amorphous	5	~12	2.4	146
MnFe <sub>2</sub> O <sub>4</sub>	Hollow sphere	2	~260	11	147
Fe <sub>2</sub> O <sub>3</sub> /SiO <sub>2</sub> /MnO <sub>2</sub>	Tube	5	380.8±38.7	22.4	This work

The presence of γ-Fe<sub>2</sub>O<sub>3</sub> NPs provides magnetic properties to the FeSiMnO<sub>x</sub> micromotors. Considering the intended use of micromotors for water cleaning, magnetic properties add beneficial functionality for guiding their swimming direction and for their removal by an external magnet after the cleaning treatment,<sup>13,56</sup> avoiding further water contamination by the catalyst itself, which is one the key issues in water treatment.<sup>8</sup> Moreover, the magnetic properties of FeSiMnO<sub>x</sub> would allow to magnetically guide them towards polluted areas that are difficult to access. More importantly, once the different kind of pollutants are removed, the micromotors could be guided<sup>13</sup> or transferred<sup>56</sup> to another container

for further decontamination processes. **Figure 48A-B** displays the snapshots of the micromotors without and with magnetic control, respectively. The orientation of the micromotors was randomly distributed in the absence of a magnetic field (**Figure 48C**). After applying the magnetic field, most of the micromotors were aligned and following the instructed direction (downward), even in the presence of massive bubbling (**Figure 48D**). As can be seen from **Figure 48E**, after applying the magnetic field, the direction of FeSiMnO<sub>x</sub> micromotors can be also changed instantly from left to right (**Figure 48E**).

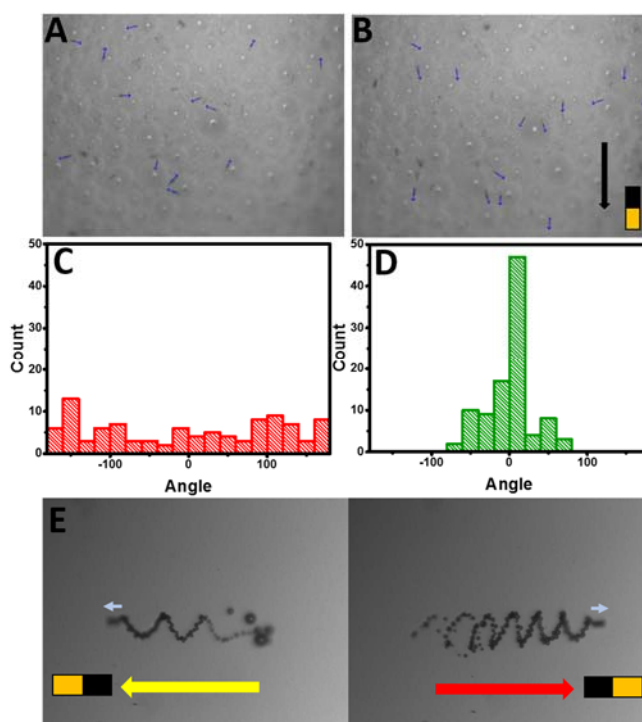


**Figure 48. Magnetic control of FeSiMnO<sub>x</sub> micromotors.** A) A snapshot from a video of FeSiMnO<sub>x</sub> micromotors swimming with random orientation, B) A snapshot from a video of FeSiMnO<sub>x</sub> micromotors with their orientation controlled by magnetic guidance (downward), C) Distribution of orientation of micromotors without magnetic field (n=100), D) Distribution of orientation of micromotors in the presence of magnetic field along Y axis (n=100) and E) Optical snapshot from a video of FeSiMnO<sub>x</sub> micromotors controlled by magnetic guidance (left and right).

The photocatalytic performance of the FeSiMnO<sub>x</sub> micromotors was evaluated upon the degradation of tetracycline (TC) and Rhodamine B (RB) (chosen as model

pollutants from the pharmaceutical and dye industries, respectively). These kinds of pollutants are known as refractory organic compounds, being very difficult to remove by the classical wastewater treatments.

First, to evaluate the photocatalytic performance of  $\text{FeSiMnO}_x$  micromotors, control experiments without micromotors were carried out. To this end, the contribution of  $\text{H}_2\text{O}_2$  (in the dark) and  $\text{H}_2\text{O}_2$  plus visible irradiation was studied in the degradation of the above-mentioned pollutants. As can be seen in **Figure 49A-B**, both controls are only degrading 10% and 30% after 15 min in the case of TC and RB, respectively. In addition, enhanced degradation rates of both pollutants were not observed after visible irradiation in the presence of  $\text{H}_2\text{O}_2$  and without micromotors.

The photocatalytic experiments were then performed in the presence of micromotors. As it is observed in **Figure 49A** and **B**, the degradation rates were markedly improved in comparison with the control tests, following an increasing trend:  $\text{FeSiMnO}_x > \text{SiMnO}_x > \text{FeSiMnO}_x$  (in the dark)  $> \text{FeSiO}_x$  microtubes. Since  $\text{FeSiO}_x$  microtubes (without  $\text{MnO}_2$ ) do not present self-propulsion, the slight degradation performance was due to the photocatalytic properties of  $\text{Fe}_2\text{O}_3$  NPs on the surface of  $\text{FeSiO}_x$  microtubes. In the case of  $\text{SiMnO}_x$  micromotors,  $\text{MnO}_2$  can act as a dual catalyst for the decomposition of  $\text{H}_2\text{O}_2$  to generate  $\text{O}_2$  bubbles for the motion but also for the degradation of organic pollutants *via* Fenton-like reaction.<sup>35,57,58</sup> However, as shown in **Figure 49A** and **B**, the resulting performance is much slower than the one obtained with the  $\text{FeSiMnO}_x$  micromotors.

The fast degradation activity shown by  $\text{FeSiMnO}_x$  micromotors is mainly due to the efficient photocatalytic performance exhibited by  $\gamma\text{-Fe}_2\text{O}_3$  NPs on the surface of the micromotors, along with the catalytic properties of  $\text{MnO}_2$  on the inner surface. When the degradation reactions were carried out in the presence of  $\text{FeSiMnO}_x$  micromotors and  $\text{H}_2\text{O}_2$  under dark conditions (**Figure 49A** and **B**), the removal yield was much lower than  $\text{FeSiMnO}_x$  micromotors under visible light irradiation.

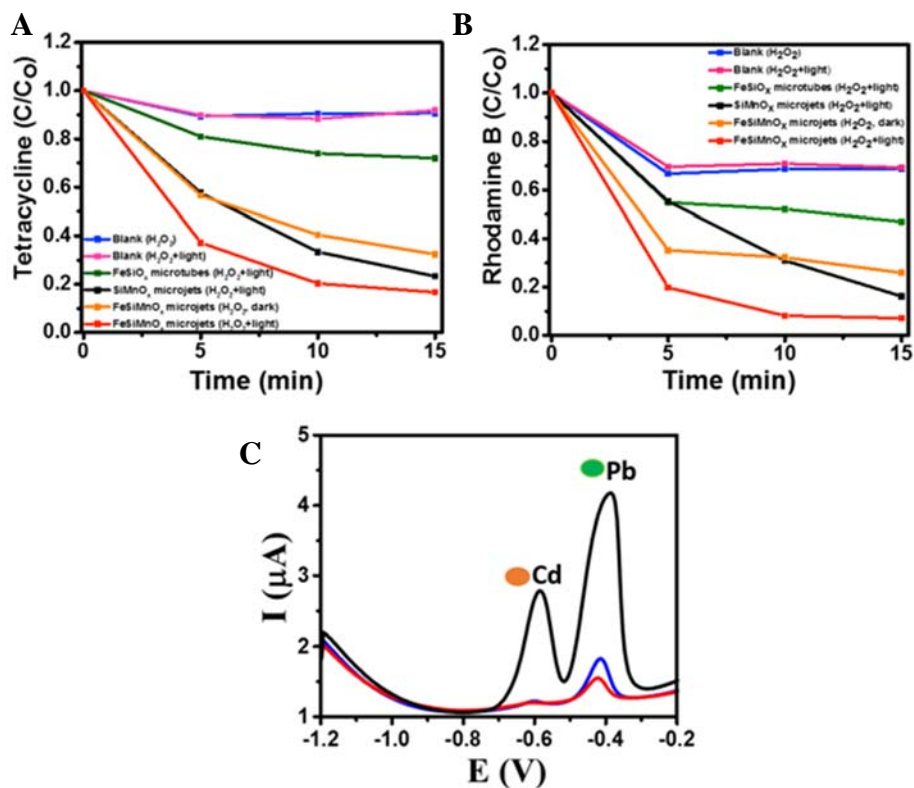


**Figure 49.** Removal of contaminants in wastewater over FeSiMnO<sub>x</sub> micromotors after 15 min of reaction. (A) C/C<sub>0</sub> kinetics of photocatalytic degradation of TC, (B) C/C<sub>0</sub> kinetics of photocatalytic degradation of RB, (C) Removal of lead and cadmium by adsorption on FeSiMnO<sub>x</sub> micromotors in presence of 10 ppm RB at 0 min (black) after 7 min (blue) and 15 min (red) of reaction.

The mechanism of the photocatalytic degradation of RB and TC involves the activation of  $\gamma$ -Fe<sub>2</sub>O<sub>3</sub> photocatalyst with visible irradiation to generate electron-hole pairs. These photogenerated pairs can migrate to the catalyst surface and react with the adsorbed molecules to produce hydroxyl (HO<sup>•</sup>) and superoxide (O<sub>2</sub><sup>•-</sup>) radicals.<sup>59–61</sup> Given the high oxidation potential of these radicals,<sup>62</sup> they can perform the total degradation of the organic matter (pollutants) to non-harmful molecules (CO<sub>2</sub> and water). At the same time, MnO<sub>2</sub> can also produce additional HO<sup>•</sup> radicals through the Fenton-like reaction in the presence of H<sub>2</sub>O<sub>2</sub><sup>57,63–66</sup>, resulting in an enhancement of the total oxidation of the organic pollutants.

Finally, to prove that FeSiMnO<sub>x</sub> micromotors can remove other types of contaminants, we selected Cd<sup>2+</sup> and Pb<sup>2+</sup> as model pollutants of toxic heavy metals.

Taking advantage of the interactions between  $\text{Fe}_2\text{O}_3$  NPs and heavy metals<sup>67,68</sup>, we used  $\text{FeSiMnO}_x$  micromotors for the removal of  $\text{Cd}^{2+}$  and  $\text{Pb}^{2+}$  in the presence of another pollutant, such as RB. **Figure 49C** illustrates the results corresponding to the capture of both heavy metals from water after 7 and 15 min of treatment with 0.3 mg  $\text{FeSiMnO}_x$  micromotors in 5%  $\text{H}_2\text{O}_2$ . It was observed that  $\text{FeSiMnO}_x$  micromotors were able to remove more than 98% and 94% ( $n=3$ ) of  $\text{Cd}^{2+}$  and  $\text{Pb}^{2+}$ , respectively, from a contaminated water with 1 ppm of each metal. Thus, we demonstrated that  $\text{FeSiMnO}_x$  micromotors can be used for the efficient remediation of several classes of contaminants, such as antibiotics, dyes and heavy metals in wastewater.

### 5.1.3. Conclusions

In conclusion, we have developed highly efficient  $\text{FeSiMnO}_x$  micromotors for multifunctional environmental applications, such as the degradation of persistent organic pollutants under visible irradiation and the removal of heavy metals from wastewater. The micromotors can be easily guided and extracted using a magnetic field. Remarkably,  $\text{FeSiMnO}_x$  micromotors exhibited the highest speed ( $485 \pm 32 \mu\text{m s}^{-1}$ ) that has been obtained so far for tubular micromotors powered by non-noble metals such as  $\text{MnO}_2$ . The synthesis of micromotors was carried out using only chemical methods and simple apparatus, which is an advantage for their eventual mass-production. The strategy of combining two metal oxides ( $\text{Fe}_2\text{O}_3/\text{MnO}_2$ ) that can decompose  $\text{H}_2\text{O}_2$  with simultaneous generation of hydroxyl radicals resulted in a significant improvement in the photocatalytic performance of the micromotors. This approach opens up new inexpensive alternative methods to fabricate other types of metal-oxide based micromotors and microtubular structures for different applications in the environmental field.

### 5.1.4. Experimental methods

#### 5.1.4a. Synthesis of micromotors

Mesoporous silica ( $\text{SiO}_2$ ) microtubes were obtained using a polycarbonate membrane (Whatman, conical-shaped micropores with 2  $\mu\text{m}$  diameter) as the template, and a mixture of tetraethyl orthosilicate (TEOS,  $\geq 99.0\%$  (GC), Sigma-Aldrich), hexadecyltrimethylammonium bromide (CTAB, BioUltra  $\geq 99.0\%$ , Sigma-Aldrich), 3-aminopropyltriethoxysilane (APTES, 99.0%, Sigma-Aldrich) and triethanolamine (TEOA,  $\geq 99.0\%$ , Sigma-Aldrich), as described in a previous work reported by our group.<sup>34</sup> These  $\text{SiO}_2$  microtubes were used as the scaffold for the micromotors. Once the mesoporous silica tubes were grown inside the membrane, it was placed in 30 mL of 10mM  $\text{KMnO}_4$  (ACS reagent  $\geq 99.0\%$ , Sigma-Aldrich) and transferred into a 50 mL Teflon-lined stainless-steel autoclave and heated at 160  $^\circ\text{C}$  for 9 h. Afterwards, the black resulting membrane was polished with water to remove the excess of  $\text{MnO}_2$ . The  $\text{SiO}_2$ - $\text{MnO}_2$  microtubes were released by dissolving the membrane template in  $\text{CH}_2\text{Cl}_2$  (GPR RECTAPUR, VWR) for 15 min and then washing them twice for 3 min with  $\text{CH}_2\text{Cl}_2$ , ethanol and water, respectively.

To optimize the  $\text{MnO}_2$  filling inside the silica tubes, different  $\text{KMnO}_4$  loadings of 10, 20 and 30 mM were tested. The best swimming behavior was observed in  $\text{MnO}_2$ -based microtubes synthesized with 10 mM of  $\text{KMnO}_4$ , thus being this concentration of  $\text{KMnO}_4$  selected as the optimal concentration for our fabrication protocol.

Finally, the surface of  $\text{SiO}_2$ - $\text{MnO}_2$  microtubes was functionalized with  $\gamma$ - $\text{Fe}_2\text{O}_3$  (Maghemite, nanopowder  $< 50$  nm, Sigma-Aldrich) by mixing them with 1 mL of an ethanolic suspension containing 0.001 g of  $\gamma$ - $\text{Fe}_2\text{O}_3$  nanoparticles (NPs) for 6 h. After this, the  $\text{Fe}_2\text{O}_3$ / $\text{SiO}_2$ - $\text{MnO}_2$  microtubes were separated from the NPs by filtering the suspension with a 2  $\mu\text{m}$  pore size membrane (Whatman), and then they were washed several times with ethanol and water, respectively.

For the sake of simplicity, the  $\text{Fe}_2\text{O}_3$ / $\text{SiO}_2$ - $\text{MnO}_2$ -based microtubes have been labelled as  $\text{FeSiMnO}_x$  micromotors,  $\text{SiMnO}_x$  micromotors (without  $\text{Fe}_2\text{O}_3$ ) or  $\text{FeSiO}_x$  microtubes (without  $\text{MnO}_2$ ).

### 5.1.4b. Micromotors characterization

A JEOL JEM-2100 LaB6 microscope operating at 200 kV accelerating voltage and equipped with an Oxford Instruments INCA x-sight (Si(Li) detector) and a Zeiss SESAM microscope (200kV) equipped with an EDS System from ThermoFisher were used to perform transmission electron microscopy (TEM) and Energy-dispersive X-ray (EDX) analysis. Scanning Electron Microscopy (SEM) images were taken on a FEI NOVA NanoSEM 230 microscope. Surface charge of  $\gamma$ -Fe<sub>2</sub>O<sub>3</sub> NPs was examined by Dynamic Light Scattering (DLS, Wyatt Möbius coupled with an Atlas cell pressurization system). The motion of micromotors was observed and recorded by using an inverted optical Microscope (Leica DMI 3000 B) equipped with a camera (Leica DFC 3000 G) with LAS V4.5 software. For recording the videos, 10  $\mu$ L of micromotors suspension was placed onto a glass slide and 0.2 wt% of sodium dodecyl sulfate (SDS, ACS reagent  $\geq$ 99.0%, Sigma-Aldrich) was added in the presence of different concentrations of H<sub>2</sub>O<sub>2</sub>. The speed and tracking of micromotors was calculated from the recorded videos and analyzed using openCV libraries and Python-based software.

The magnetic control setup consists of two pairs of coils in Helmholtz configuration, which create a magnetic field gradient in, respectively, the X and Y directions. Cylindrical steel rods are put inside the coils to increase the strength field. The intensity of the gradient is controlled remotely through an Arduino microcontroller, whose current is amplified using a TS250 Wave Amplifier. A Python script with a user interface is used to send orders to the Arduino in real time, allowing total control of the magnetic field from a PC. The gradient per unit of electric current created by the coils for each pair is 18 G (A·mm)<sup>-1</sup>. During the magnetic control experiments, a maximum current of 2.5 A was used.

### 5.1.4c. Photocatalytic set-up

The photocatalytic degradation of aqueous solutions of rhodamine (RB) and tetracycline (TC) was carried out in a 5mL cylindrical glass vessel. For the

photocatalytic experiments, a 300 W high pressure UV-visible lamp (Ultravitalux Osram, 280-780 nm) was used as light source. A polyester UV filter sheet (Edmund Optics) was used to remove wavelengths radiation below 400 nm and to ensure only visible irradiation. In all degradation experiments, 1 mL of RB (10 ppm) or TC (50 ppm) solution containing 0.3 mg of micromotors was placed in the vessel with 0.2 wt% SDS as surfactant. No acidic or basic pH adjustments were performed during the photocatalytic tests.

Prior to illumination, the micromotors were kept in the dark for 30 min to reach adsorption-desorption equilibrium on their surface. In this way, the decrease in the absorbance signal of the pollutants due to adsorption can be ruled out in the degradation experiments. After that, the lamp was turned on and 5 wt% H<sub>2</sub>O<sub>2</sub> was added to initiate the reaction. Liquid aliquots were periodically taken out during the reaction (before the absorbance measurements, the solids were removed by centrifugation in the case of SiMnO<sub>x</sub> micromotors or by a magnet in the case of FeSiMnO<sub>x</sub> and FeSiO<sub>x</sub> micromotors). They were then immediately analyzed by measuring their absorbance at 555 nm and 358 nm for RB and TC respectively, using a UV-Vis spectrophotometer (Specord 50 plus).

Control experiments without micromotors (only H<sub>2</sub>O<sub>2</sub> or H<sub>2</sub>O<sub>2</sub> + light irradiation) were also performed to evaluate the contribution of the photolysis of H<sub>2</sub>O<sub>2</sub> on the oxidation of our target pollutants. Additionally, a test with non-filled FeSiO<sub>x</sub> microtubes (without MnO<sub>2</sub>) in the presence of H<sub>2</sub>O<sub>2</sub> under light irradiation was also carried out to investigate the importance of the motion of micromotors on the photocatalytic performance.

### 5.1.4d. Heavy metals removal

To prove the capability of FeSiMnO<sub>x</sub> micromotors to capture heavy metals, 0.3 mg of the micromotors was added to 1 mL of a water solution, which contained 1 ppm of lead (Pb<sup>2+</sup>) and cadmium (Cd<sup>2+</sup>), in the presence of another contaminant (10 ppm of RB). After allowing the FeSiMnO<sub>x</sub> micromotors to swim for 7 and 15 min in the previously prepared solution, the concentration of both heavy metals was determined at both time intervals by square wave voltammetry using a mercury-coated glassy carbon electrode (GCE)<sup>46</sup> as working electrode. Prior to the measurements, any trace of H<sub>2</sub>O<sub>2</sub> was removed by adding an excess of 1 M sodium bisulfite solution to avoid any interference in the electrochemical signals. First, the mercury film was pre-plated at the beginning from a non-deaerated 80 mg L<sup>-1</sup> mercury solution (in 0.02 M HCl), by holding the carbon strip electrode at -1.15 V for 15 min. Then, the potential was switched to -0.20 V for a 2 min cleaning period. The subsequent cycles involved the Pb<sup>2+</sup> and Cd<sup>2+</sup> deposition (3 min of preconcentration at -1.15 V) and stripping steps (from -1.15V to -0.2V). Before the next measurement, the electrode is maintained for 60 s at -0.2 V to ensure that Pb and Cd do not remain on the working electrode surface. After finishing the measurement of heavy metals, the mercury film is removed from the GCE by holding it at +0.4 V for 5 min. An acetate buffer 0.02 M solution (pH 4.8) was used as electrolyte during the sensing of the heavy metals, the intermediate steps and the removal of the mercury film from the GCE.

The linear range was between 0.01–0.1 ppm for Pb<sup>2+</sup> (Area<sub>peak</sub>=1.086+0.027[Pb<sup>2+</sup>], r=0.980) and Cd<sup>2+</sup> (Area<sub>peak</sub>=0.04255+0.01405[Cd<sup>2+</sup>], r=0.990), respectively. To measure the concentration of Pb<sup>2+</sup> and Cd<sup>2+</sup> ions from the assay solution, a dilution 1:10 (total volume 5 mL, 0.02 acetate buffer solution) was carried out, before and after the removal of both ions by the FeSiMnO<sub>x</sub> micromotors.

## 5.2. Template free synthesis of micromotors

### 5.2.1. Introduction

Most of the micromotors-based systems reported for environmental applications are propelled by bubble thrust and contain platinum as a catalyst to obtain motion by decomposition of  $\text{H}_2\text{O}_2$ . They are typically fabricated by various multi-step processes like template assisted synthesis or photolithography, and subsequent glancing angle deposition. These techniques produce multi-material structures with a cavity where bubbles can grow from the locally saturated oxygen and get ejected, which induces self-propulsion. The motion of the catalytic self-propelled micromotors enhances micro-mixing and mass transfer in the aqueous system, thus increasing the removal rate of pollutants present in wastewaters by the functional material (adsorbent or oxidative catalyst)<sup>69,77</sup>. For instance, micromotors have been proven to be useful for heavy metal removal<sup>148,149</sup>, organic removal<sup>71,150–155</sup> and bacteria disinfection<sup>36,118,119,156</sup>. One of the major challenges is the prohibitive cost associated with the use of platinum for micromotors propulsion<sup>157</sup>. Furthermore, current fabrication methods make scaling up challenging and expensive<sup>21</sup>. The mass production method of micromotors based on an inexpensive material is the key to their large-scale viability for water treatment remediation. Efforts have been made to develop platinum free catalytic micromotors for organic removal from water, nevertheless the reported systems still require the addition of surfactants to work efficiently<sup>158–160</sup>. These surfactants are often toxic and add an extra organic contamination load in water.

Iron and other transition metals based react with  $\text{H}_2\text{O}_2$  via Fenton-Like reactions to produce reactive oxygen species (ROS), especially hydroxyl radicals ( $\text{HO}\cdot$ ) by decomposition of  $\text{H}_2\text{O}_2$ . Fenton-Like processes are complex and include multiple chain reactions, which generate hydroxyl radicals and oxygen gas during the catalysis cycle<sup>161</sup>. Hydroxyl radicals generated by Fenton-like reactions are extremely oxidative, thus they are very important for advanced oxidative process to degrade refractory organic pollutants which cannot be removed naturally by

microorganisms<sup>162</sup>. Pharmaceutical pollutants, namely antibiotics, hormones, and phenolic compounds are among the refractory pollutants that are toxic for humans and aquatic life even at very low concentrations<sup>163</sup>. Currently, industrial and municipal water treatment plants widely use activated sludge methods to remove organic pollutants from wastewater, which is often not sufficient to remove these contaminants<sup>164,165</sup>.

Here, we present platinum and surfactant free cobalt ferrite-based bubble propelled micromotors (CFO micromotors) for oxidation of tetracycline (TC) antibiotic, as pharmaceutical model pollutant, via Fenton-like reaction. Tetracycline is one of most widely used antibiotic for human and veterinary healthcare<sup>166</sup>. The CFO micromotors function as self-propelled heterogeneous Fenton-like catalysts in presence of H<sub>2</sub>O<sub>2</sub>, which acts as both fuel for micromotors propulsion and reagent for Fenton-like oxidation of the antibiotic pollutant. Furthermore, CFO micromotors are also ferromagnetic in nature, which makes it possible to easily recover the micromotors after the completion of degradation process.

### 5.2.2. Results and discussion

CFO micromotors were fabricated from the cobalt ferrite nanoparticles, which were synthesized by using cobalt(II) acetate and iron(III) chloride (molar ratio Co<sup>2+</sup>/Fe<sup>3+</sup> = 0.5) as precursors in ethylene glycol via solvothermal route<sup>167</sup>. The solvent ethylene glycol acts as a reducing agent while sodium acetate and polyethylene glycol are added in the solution to prevent the aggregation of nanoparticles during the synthesis in the liquid phase.

The synthesized cobalt ferrite nanoparticles were dried to obtain agglomerated micrometer-sized CFO micromotors as depicted in **Figure 50A**. The CFO micromotors decompose H<sub>2</sub>O<sub>2</sub> into strongly oxidizing hydroxyl radicals via Fenton-like reaction that can oxidize TC antibiotic into intermediate oxidized products and eventually into carbon dioxide (CO<sub>2</sub>). In addition, the oxygen gas (O<sub>2</sub>) bubbles generated during H<sub>2</sub>O<sub>2</sub> decomposition induce self-propulsion of the micromotors,

which enhances mass transfer and micro-mixing of the solution to further promote the degradation of tetracycline (TC) by the hydroxyl radicals (Figure 50B).

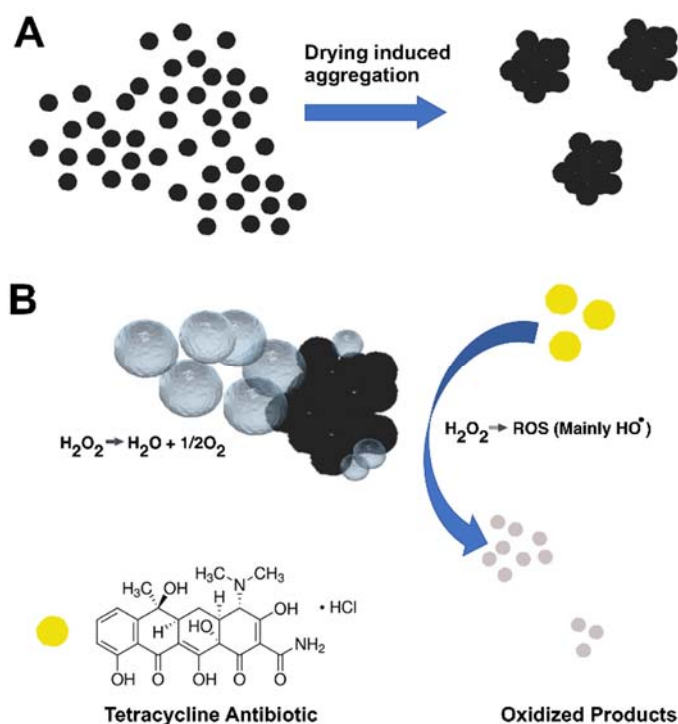


**Figure 50.** Scheme of the synthesis and mechanism of the cobalt-iron micromotors (CFO micromotors). (A) Synthesis of the CFO micromotors by drying of cobalt ferrite nanoparticles. (B) Degradation of tetracycline (TC) antibiotic by using the self-propelled CFO micromotors.

CFO micromotors were characterized by TEM and SEM (Figure 51A, B & C). Figure 51A displays a TEM image of synthesized cobalt ferrite nanoparticles. It is observed that the diameter of individual nanoparticles is smaller than 100 nm. The cobalt ferrite nanoparticles have tendency to agglomerate because of strong magnetic interactions between the particles, therefore it is hard to prevent their agglomeration, even in the suspension form.<sup>167,168</sup> Once the nanoparticles are washed to remove unreacted solvents and surface stabilizer and dried, they strongly adhere with each other and require significant stress to deform.<sup>169,170</sup> The aggregated nanoparticles form microparticles of various sizes, ranging from submicron scale aggregates to a few hundred micrometers. The resulting microparticles were further

grinded and sieved to obtain micromotors under 100 micrometers. **Figure 51B** and **C** show SEM images of a micrometer sized CFO micromotor obtained from aggregated nanoparticles. The surface of micromotors is rough and porous because of the hierarchical aggregation of the already agglomerated nanoparticles. The roughness and porosity of surface (**Figure 51C**) increase the surface area and provide favorable points for bubble nucleation, necessary for propulsion.

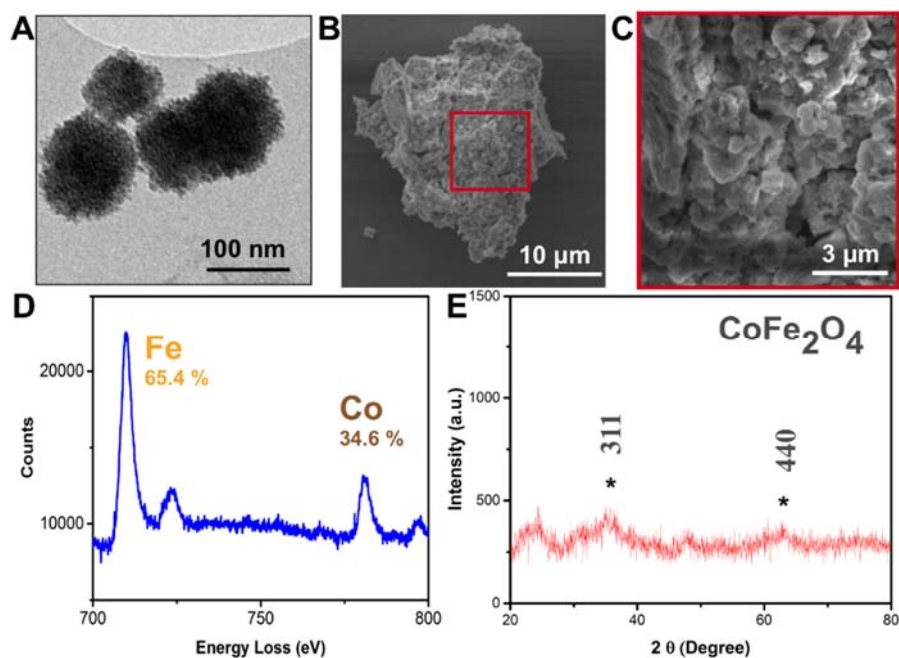


**Figure 51. Characterization of the CFO micromotors.** (A) TEM image of cobalt ferrite nanoparticles (B) SEM image of a CFO micromotor. (C) SEM image of the surface morphology of a CFO micromotor. (D) Element composition of the CFO micromotors obtained by electron energy loss spectroscopy (EELS). (E) X-ray diffraction (XRD) pattern of CFO micromotors.

The composition and crystalline structure of the CFO micromotors was analyzed by electron energy loss spectroscopy (EELS) method and XRD respectively (**Figure 51D &E**). Individual elements present in the micromotors were quantified to estimate their amount in the structure. Mainly three elements cobalt, iron, and oxygen were detected. The ratio of cobalt and iron elements was found to be 0.5 which is consistent with the ratio of the cobalt and iron precursor used in the synthesis of the micromotors (**Figure 51D**), confirming the  $\text{CoFe}_2\text{O}_4$  structure. The XRD patterns of

the dried  $\text{CoFe}_2\text{O}_4$  micromotors (**Figure 51E**) evidence a poorly crystalline structure. The (311) and (440) lattice planes correspond to  $\text{CoFe}_2\text{O}_4$  (JCPDS 22-1086).

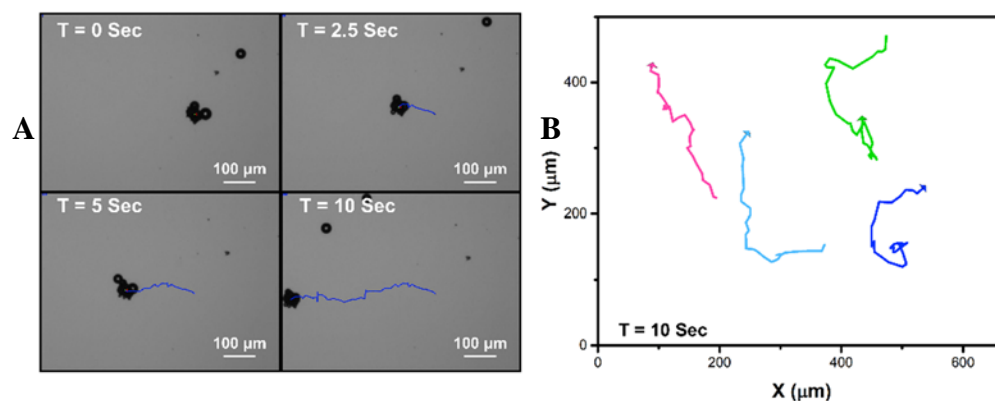


**Figure 52. Swimming behavior of CFO micromotors.** (A) Tracking of an individual CFO micromotor swimming in 5% w/w  $\text{H}_2\text{O}_2$  concentration. (B) Tracking of multiple CFO micromotors swimming in 5 % w/w  $\text{H}_2\text{O}_2$ .

The motion of cobalt ferrite nanoparticles and micromotors was investigated by optical microscopy. We observed that the nanoparticles do not exhibit bubble propulsion in  $\text{H}_2\text{O}_2$  solution. Bubbles were only observed in the bulk liquid or on the surface of the container due to gas saturation in the sample. On the contrary, in the case of CFO micromotors, they self-propel by the bubbles generated from the decomposition of  $\text{H}_2\text{O}_2$  fuel at their surface because their bigger size and rough surface can provide sufficient nucleation points for bubbles to grow. It has previously been reported that the size limit of the catalytic micromotors for bubble propulsion depends on the catalytic activity, concentration of  $\text{H}_2\text{O}_2$  and various geometrical factors<sup>33</sup>. For instance, platinum coated spherical micromotors can only exhibit bubble propulsion if their diameters are above  $10\ \mu\text{m}$ <sup>32</sup>. However, tubular micromotors can swim by bubble propulsion even with sub-micrometer diameter due to the confinement of the gas generated in the tubular structure<sup>171</sup>. In the case of CFO micromotors, a precise quantification of their cut-off size for bubble propulsion is difficult to assess due to the asymmetric shape of the micromotors which leads to a different number of nucleation points for the bubble growth and detachment. **Figure 52A** shows tracking of an individual CFO micromotor swimming

in 5% w/w  $H_2O_2$  for 10 seconds. We observed that the motion of the micromotors was pulsatile and the recoil force of the bubble detachment mainly contributed to their motion. Swarms of CFO micromotors rapidly move around the liquid producing a chaotic swimming behavior that can induce an efficient mixing in the system. **Figure 52B** illustrates the tracking of four different CFO micromotors swimming for 10 seconds. CFO micromotors can maintain individual swimming direction even though bursting and fusion of the bubbles create often strong drift in the liquid.

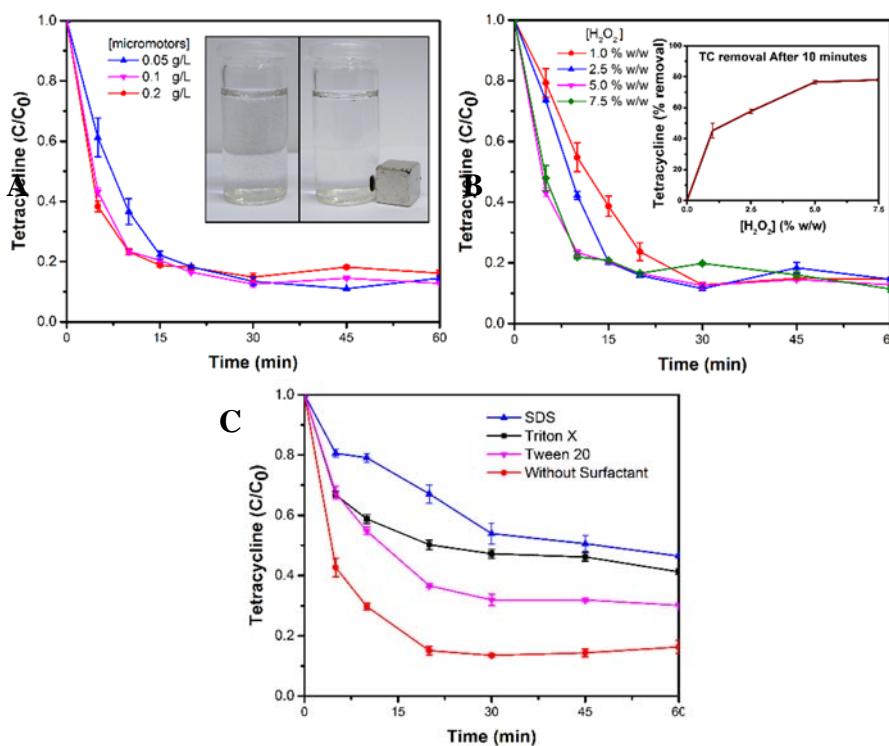


**Figure 53. Degradation of TC antibiotic by CFO micromotors.** (A) Effect of different amount of CFO micromotors. (Inset: Extraction of micromotors using NdFeB magnet) (B) Effect of different  $H_2O_2$  concentrations. (Inset: TC removal after 10 minutes of reaction with micromotors at different  $H_2O_2$  concentrations). (C) Effect of presence of various surfactants

The CFO micromotors were studied for their efficiency towards TC degradation via Fenton-like reaction. First, the micromotors concentration was optimized by using different amounts of CFO micromotors from 0.05 to 0.2 g/L in the presence of 5%

w/w H<sub>2</sub>O<sub>2</sub> (**Figure 53A**). We observed that the degradation rate of TC did not increase above 0.1 g/L micromotors. To study the effect of H<sub>2</sub>O<sub>2</sub>, further experiments were carried out using 0.1 g/L CFO micromotors and varying the H<sub>2</sub>O<sub>2</sub> concentration (1%, 2.5%, 5% and 7.5% w/w). As it is observed in **Figure 53B**, the TC degradation rate increased by increasing H<sub>2</sub>O<sub>2</sub> concentration, reaching a maximum at 5% w/w (**Figure 53B** inset). 0.1 g/L micromotors and 5% w/w H<sub>2</sub>O<sub>2</sub> were selected as optimized concentrations and for further experiments to study the effect of surfactants and the generation of hydroxyl radicals.

Generally, surfactants are added to the solution to improve the overall swimming behavior of the micromotors regarding directionality and speed. Surfactants stabilize the interface of bubbles therefore facilitating their detachment from the micromotors surface, which smoothens the swimming and decreases the drift in the liquid due to fusion and bursting of bubbles<sup>172</sup>. In certain cases, surfactants are even necessary to achieve motion of micromotors.<sup>173</sup> Recently, it has been reported that addition of surfactants improves pollutant removal efficiency of micromotors because of the improvement in the swimming behavior and adsorptive separation of pollutants on the bubbles.<sup>69,158,159</sup> However, surfactants increase the organic matter of the wastewater and can be toxic, requiring further treatment such as electrocoagulation processes<sup>174,175</sup>. We studied the performance of CFO micromotors for TC antibiotic degradation in the presence of various surfactants, such as sodium dodecyl sulfate (SDS), triton-X and Tween 20 and without the addition of surfactant. CFO micromotors performed better (~84%) for removal of TC when surfactants were not added in the system. However, the presence of surfactants severely affected the performance of degradation of TC by the CFO micromotors (**Figure 53C**). Indeed, it was observed that SDS (~54 % removal) decreased the efficiency of TC degradation more significantly than Tween 20 and Triton-X (~70 % and ~59% removal respectively). The extra organic load added by the presence of the surfactant can competitively consume the reactive oxygen species produced by the Fenton-like reaction. Furthermore, surfactants form micellar structure around TC molecules that may oxidize first and prevent access of

hydroxyl radicals to TC. This effect can be enhanced for anionic surfactant like SDS due to its electrostatic interaction with TC<sup>176</sup>.

The degradation efficiency of TC by the CFO micromotors was compared with control experiments using only H<sub>2</sub>O<sub>2</sub> without the addition of the CFO micromotors and the TC degradation by the micromotors without the addition of H<sub>2</sub>O<sub>2</sub>. As shown in **Figure 54A**, only a small decrease in the characteristic absorbance peak of TC in both control experiments were observed, which can be attributed to the oxidative nature of the H<sub>2</sub>O<sub>2</sub> and adsorption of TC on the CFO micromotors. TC degradation was minimal in the control experiments while in the presence of swimming CFO micromotors most of the antibiotic was degraded from the solution after 10 min of the Fenton-like reaction, being the characteristic absorbance peak of TC negligible.

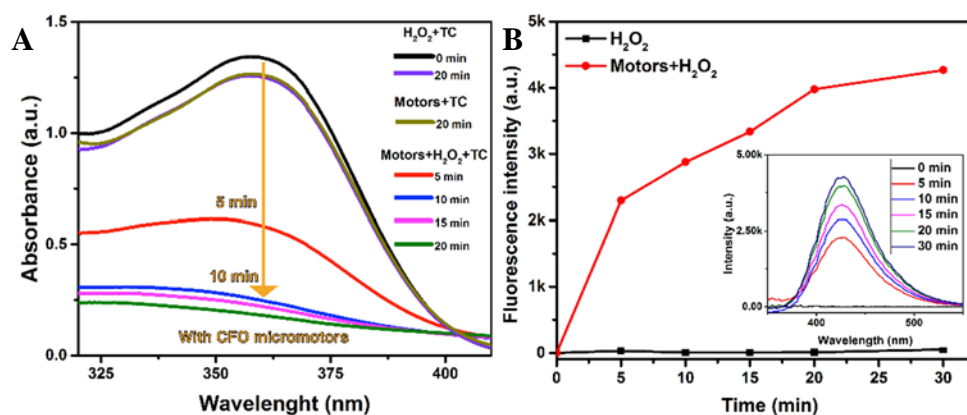
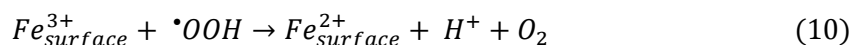
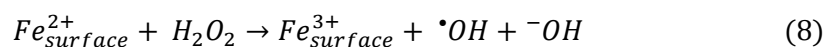


**Figure 54. Degradation of TC and production of hydroxyl radicals.** (A) Degradation of TC by the CFO micromotors approach at optimized H<sub>2</sub>O<sub>2</sub> concentration (5%) and CFO micromotors amount (0.1 g/L) over time. (B) Hydroxyl radical generated during the swimming of CFO micromotors in H<sub>2</sub>O<sub>2</sub> probed by fluorescence intensity measurement of 2-hydroxyterephthalic acid converted from terephthalic acid. (Inset: fluorescence spectra scan over time).

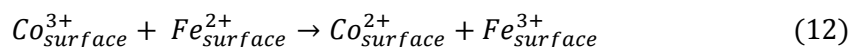
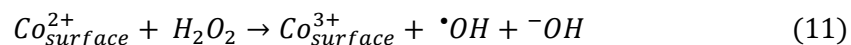
The degradation pathway of TC was previously studied by other researchers giving a general idea of its possible mineralization pathways<sup>177</sup>. The mechanism includes oxidation of the methyl and amino groups attached to the aromatic rings, followed by the ring opening reactions that subsequently become oxidized into the short chain carboxylic acids before mineralization into carbon dioxide. Because of the complex structure of the TC molecules, many intermediate molecules can be

produced during the oxidative removal. Hydroxyl radicals are considered the key oxidative radicals generated in the Fenton-like reaction that are mainly responsible for such mineralization process. To verify the generation of the hydroxyl radical by CFO micromotors, we used terephthalic acid as probe molecule, that acts as selective scavenger of hydroxyl radicals and converts into 2-hydroxyterephthalic, which is fluorescent. The increase in 2-hydroxyterephthalic acid concentration was measured by fluorescence spectrometry. Figure 5B displays the increase in the fluorescence signal of 2-hydroxyterephthalic acid over time when the CFO micromotors are swimming in mixture of H<sub>2</sub>O<sub>2</sub> and terephthalic acid solution, thus confirming the presence of the hydroxyl radicals. Fluorescence signal of 2-hydroxyterephthalic acid rapidly increases over the time during the Fenton-like reaction of CFO micromotors indicating an increase in the generation of hydroxyl radicals. Hydroxyl radical production rate slows down after 20 minutes of reaction which can be attributed to depletion in both, H<sub>2</sub>O<sub>2</sub> and terephthalic acid concentrations.

Fenton reaction mechanism, proposed by Haber and Weiss, can explain both the production of hydroxyl radicals for organic degradation (Eq. 8) and oxygen bubble for self-propulsion in the ferrous ions recycling step (Eq. 10).



Presence of cobalt in the catalyst structure can also activate H<sub>2</sub>O<sub>2</sub> for increased production of hydroxyl radicals, thus increasing the efficiency of the catalyst (Eq. 11).



$\text{Co}^{3+}$  can be recycled back to  $\text{Co}^{2+}$  by  $\text{Fe}^{2+}$  because of the thermodynamically favorable redox reaction to accelerate decomposition of  $\text{H}_2\text{O}_2$ <sup>178</sup> (Eq. 13). Apart from above mentioned radical mediated production of oxygen gas, surface oxygen vacancies present in the metal oxides can also decompose  $\text{H}_2\text{O}_2$  directly into oxygen and water without producing intermediate hydroxyl radicals<sup>179</sup>. However, the detection of hydroxyl radicals suggests the involvement of radical mediated pathways for CFO micromotors for both the degradation of TC and generation of oxygen gas for self-propulsion.

### 5.2.3. Conclusions

We have fabricated inexpensive CFO based micromotors by nanoparticle drying process, using easily scalable synthesis methods. The CFO micromotors can swim without the addition of surfactants in the system and efficiently degrade antibiotics from wastewater. Furthermore, we observed that the presence of the surfactants decreases the efficiency of CFO micromotors. We have also verified the production of hydroxyl radicals to support the oxidation mechanism of TC by CFO micromotors. Since the hydroxyl radicals are non-selective oxidants, these micromotors can potentially be used for wide range of pharmaceutical and other organic pollutants. We believe that CFO micromotors do not only demonstrate the usability of self-propelled micromotors for wastewater cleaning, but also show an improvement of previously reported systems, since they are composed of cheap materials and do not require the addition of surfactants, which are an extra organic load on the water.

### 5.2.4. Experimental methods

#### 5.2.4a Synthesis and characterization of micromotors

CFO micromotors were fabricated from cobalt ferrite nanoparticles. Cobalt ferrite nanoparticles were synthesized by solvothermal method using cobalt acetate (CoAc, sigma 403024) and Iron(III) chloride hexahydrate ( $\text{FeCl}_3 \cdot 6\text{H}_2\text{O}$ , sigma F2877) as the precursors. First, 0.92 g CoAc and 1 g  $\text{FeCl}_3 \cdot 6\text{H}_2\text{O}$  were dissolved in 30 ml of

ethylene glycol (sigma 324558). Then, 2.78 mg of sodium acetate (NaAc, sigma S8750) and 1 ml of polyethylene glycol (PEG 200, Alfa Aesar B21918) as the stabilizer were added to the previous mix. The prepared solution was transferred into 50 ml Teflon lined hydrothermal autoclave and heated to 170°C for 15 hours. After the reaction was completed the reactor was cool down to room temperature and then the content was transferred into a beaker. The nanoparticle suspension obtained was washed multiple times with isopropanol (Panreac 211090) to remove ethylene glycol and unreacted precursor molecules. Then, the resulting suspension was dried using an oven at 80°C for 15 hours. The drying process induces the aggregation of the cobalt ferrite nanoparticles into few hundred-micrometers sizes of microparticles. These microparticles were manually grounded and sieved to obtain CFO micromotors with the size under 100 micrometers.

A diluted suspension of the cobalt ferrite nanoparticles was dried overnight at room temperature on a copper grid to prepare samples for the transmission electron microscopy (TEM) analysis. JEOL Centurio model was used to obtain images of nanoparticles. Electron energy loss spectroscopy (EELS) (Gatan GIF ERS electron energy-loss spectrometer) coupled with TEM was used to quantify ratio of Co and Fe present in the nanoparticles. The scanning electron microscope (SEM) images of CFO micromotors were obtained using a FEI NOVA NanoSEM 230 system. The crystalline structure of micromotors were further characterized by using the Bruker D8 Advance diffractometer equipped with a Cu K $\alpha$  radiation (1.5417 Å) source, a LYNXEYE super speed detector and a Ni filter.

Swimming behavior of the CFO micromotors was analyzed using an inverted optical microscope Leica DMI 3000 B equipped with a camera Leica DFC 3000 G. A custom-made 3D printed sample holder was prepared to position the glassware under the microscope for observing the swimming of the micromotors *in-situ*.

### **5.2.4b. Antibiotic degradation experiments using CFO micromotors.**

Tetracycline (TC, sigma T7660) was selected as target antibiotic. TC degradation experiments were carried out in a glass beaker containing CFO micromotors in 50 mg/L TC solution and 5% H<sub>2</sub>O<sub>2</sub> (sigma 31642). In all the experiments, the concentration of the TC was kept constant. To optimize the degradation approach, we studied different parameters. First, the effect of the amount of CFO micromotors in the efficiency of TC degradation was studied. To this end, three different suspensions of CFO micromotors with the concentrations of 0.05 g/L, 0.1 g/L, and 0.2 g/L were used in triplicate. To achieve the optimized H<sub>2</sub>O<sub>2</sub> concentration for TC degradation using CFO micromotors, four concentrations of H<sub>2</sub>O<sub>2</sub> were evaluated (1 %w/w, 2.5% w/w, 5% w/w and 7%w/w).

The effect of surfactant was studied by using the optimized concentration of 0.1 g/L CFO micromotors, 5% w/w H<sub>2</sub>O<sub>2</sub> and 50 mg/L TC. Four sets of experiments were carried out (n=3) containing three different surfactants, sodium dodecyl sulfate triton-X and tween 20 in 1% w/w concentration in three different sets and one without the presence of any surfactant.

In all the degradation experiments, aliquots of the different samples were taken at timed intervals. The concentration of TC in each sample was measured by reading the absorbance value of the sample at 358nm using a UV-Vis spectrometer.

### **5.2.4c. Identification of hydroxyl radicals.**

Terephthalic acid was used as a probe to investigate the hydroxyl radical generation during the Fenton-like reaction of CFO micromotors. A solution containing terephthalic acid (0.5mM) (sigma 185361), H<sub>2</sub>O<sub>2</sub> (5 % w/w) and CFO micromotors (0.1 g/L) was used for the experiment and an identical solution without micromotors was used as control. The presence of 2-hydroxyterephthalic acid was produced by the reaction between terephthalic acid and the generated hydroxyl radical species. This product was detected by measuring its fluorescence spectra from 350nm to 600nm at 320nm excitation wavelength using a multimode microplate reader (Tecan Infinite M200 PRO).

## CHAPTER 6.

### CONCLUSIONS AND FINAL REMARKS

Waste-water treatment and water reuse are an essential part of environmental sustainability. However, pollution originating from human activities is often difficult to clean by nature's method of waste removal. Organic pollutants, heavy metal and pathogenic microorganism contamination in water pose a serious risk to the public health and other life forms, if the wastewater is released without any additional treatment. To tackle the scarcity of clean water, nanotechnology is widely hoped for the development better treatment solutions<sup>10</sup>. Currently, researchers working in nanotechnology are designing new nanosystems and nanomaterials for fast and efficient removal of pollutants from water.

In this direction, we developed self-propelled micromotors that can efficiently remove organic pollutants, heavy metals and bacterial contaminants from polluted water. These micromotors are actively propelled in H<sub>2</sub>O<sub>2</sub> containing media, due to the propulsion force generated by oxygen gas bubbles produced via catalytic decomposition on H<sub>2</sub>O<sub>2</sub>. In the case of bactericidal micromotors, the propulsion is driven by hydrogen gas bubbles produced during the reaction of magnesium, present in the micromotors structure, with water. The active motion of the micromotors is coupled with functional materials that are mainly responsible for pollutant removal activity. We designed micromotors that use iron, iron oxides and cobalt ferrite as active materials for removal of organic pollutants via Fenton-like reactions. Heavy metal removal is targeted by using graphene oxides or silica as adsorbents, and bactericidal motors are decorated with silver nanoparticles for contact killing. We observed that the active micromotors demonstrated an improvement in pollutant removal efficiency, compared to the non-active micromotors with the same functional materials and structure. This effect is

attributed to the enhanced mass transfer induced by the active motion of the micromotors.

To expand the applicability of such micromotors to more realistic scenarios, some of the key limitations of current systems need to be addressed. One of the main challenges is related to the fabrication of micromotors via low-cost and scalable techniques. Currently used common fabrication methods require additional facilities, such as electrochemical stations, clean rooms, metal evaporators or lithography platforms, which are expensive for the large-scale synthesis necessary to clean up large volumes of contaminated water. Another economy related challenge is to avoid the use of expensive precious metals in the structure of micromotors, such as commonly used Ag, Pt, Pd and Au catalysts. We explored different approaches dealing with fabrication scalability and the use of alternative low-cost metals for their propulsion. We developed a synthesis protocol for tubular micromotors with multifunctionality. These micromotors have low-cost metal oxides, involving Mn, Si and Fe based oxides in their structure. The polycarbonate template assisted synthesis protocol does not require use of electrochemical setup, nor cleanroom and photolithography techniques, and the entire process can be done via sol-gel chemistry and hydrothermal methods.

Another important technical challenge is the use of the surfactants for the efficient propulsion of bubble-propelled micromotors. Surfactants ease the release of the bubble, facilitating their propulsion. Bubble-propelled micromotors are reported to swim either very slowly or not at all without surfactants<sup>172,173,180</sup>. Considering that these surfactants add extra organic load in the water and they can also compete with the pollutants during the degradation reaction, it may limit the overall efficiency of the performance of micromotors. Therefore, it is vital to ensure that micromotors do not leave any harmful reactants, by-products or other kinds of pollutants once their task is completed. We synthesized cobalt ferrite based micromotors that can propel without the presence of surfactants. These micromotors are simple in structure, fabricated by template free method of simple aggregation of nanoparticles and contain a single material, that acts as both the propulsion catalyst and Fenton-like

catalyst for degradation of pharmaceutical organic pollutants. The preparation of micromotors based on merely synthetic chemical procedures is promising for their potential mass-production. However, the structures synthesized by using these chemical methods are rather simple, usually containing a single material, and such methods do not allow much control for the synthesis of complex structures. Future efforts should be directed towards the development of scalable and low-cost synthesis methods for the fabrication of micromotors using inexpensive catalysts with multi-material configurations. The current system of micromotors can still be used for small scale water treatment systems, for removal of extremely toxic pollutants that are probably too dangerous to transport, for example wastewater generated during laboratory experiments involving synthesis of poisonous organic or inorganic compounds or infectious agents with high potential of biohazard.

The need of a chemical fuel can limit the application of micromotors for some environmental remediation purposes. Even though  $H_2O_2$ , commonly used in many advanced oxidative processes, is considered a green reagent (that leaves only water and oxygen), micromotors designed for the adsorptive or antimicrobial activity should explore alternative propulsion strategies in future. Having on board active materials such as magnesium, zinc or iron that react with water for propulsion and leave environmental friendly by-products could be an attractive alternative, if the fuel enables micromotors function for long enough time to complete their task. Some of the remaining challenges to be addressed include special attention to the reusability of these micromotors for the removal of different pollutants, including changes in the speed over usage time and maximum cycles of efficient decontamination. Moreover, the development of multifunctional micromotors that can simultaneously decontaminate several types of pollutants commonly found in wastewater can pave way for highly efficient single-step universal water treatment technology.

## References

- (1) Watkins, K. Human Development Report 2006-Beyond Scarcity: Power, Poverty and the Global Water Crisis. **2006**.
- (2) Xie, S.-P.; Deser, C.; Vecchi, G. A.; Ma, J.; Teng, H.; Wittenberg, A. T. Global Warming Pattern Formation: Sea Surface Temperature and Rainfall. *J. Clim.* **2010**, *23* (4), 966–986.
- (3) International Decade for Action “Water for Life” 2005-2015. Focus Areas: Water scarcity <http://www.un.org/waterforlifedecade/scarcity.shtml> (accessed Jun 26, 2018).
- (4) WWAP; UNESCO. *The United Nations World Water Development Report, 2017: Wastewater: The Untapped Resource*; UNESCO Publishing, 2017.
- (5) Marco, A.; Esplugas, S.; Saum, G. How and Why Combine Chemical and Biological Processes for Wastewater Treatment. *Water Sci. Technol.* **1997**, *35* (4), 321–327.
- (6) Werker, A. G.; Hall, E. R. Limitations for Biological Removal of Resin Acids from Pulp Mill Effluent. *Water Sci. Technol.* **1999**, *40* (11), 281–288.
- (7) Clara, M.; Strenn, B.; Gans, O.; Martinez, E.; Kreuzinger, N.; Kroiss, H. Removal of Selected Pharmaceuticals, Fragrances and Endocrine Disrupting Compounds in a Membrane Bioreactor and Conventional Wastewater Treatment Plants. *Water Res.* **2005**, *39* (19), 4797–4807.
- (8) Oturan, M. A.; Aaron, J.-J. Advanced Oxidation Processes in Water/Wastewater Treatment: Principles and Applications. A Review. *Crit. Rev. Environ. Sci. Technol.* **2014**, *44* (23), 2577–2641.
- (9) Cloete, T. E. *Nanotechnology in Water Treatment Applications*; Horizon Scientific Press, 2010.
- (10) Shannon, M. A.; Bohn, P. W.; Elimelech, M.; Georgiadis, J. G.; Marinas, B. J.; Mayes, A. M. Science and Technology for Water Purification in the Coming Decades. *Nature* **2008**, *452* (7185), 301–310.
- (11) Qu, X.; Alvarez, P. J.; Li, Q. Applications of Nanotechnology in Water and Wastewater Treatment. *Water Res.* **2013**, *47* (12), 3931–3946.
- (12) Parmar, J.; Vilela, D.; Villa, K.; Wang, J.; Sanchez, S. Micro- and Nanomotors as Active Environmental Microcleaners and Sensors. *J. Am. Chem. Soc.* **2018**.
- (13) Duan, W.; Wang, W.; Das, S.; Yadav, V.; Mallouk, T. E.; Sen, A. Synthetic Nano- and Micromachines in Analytical Chemistry: Sensing, Migration, Capture, Delivery, and Separation. *Annu. Rev. Anal. Chem.* **2015**, *8* (1), 311–333.
- (14) Restrepo-Pérez, L.; Soler, L.; Martínez-Cisneros, C.; Sánchez, S.; G. Schmidt, O. Biofunctionalized Self-Propelled Micromotors as an Alternative on-Chip Concentrating System. *Lab. Chip* **2014**, *14* (16), 2914–2917.

- (15) Koumura, N.; Zijlstra, R. W.; van Delden, R. A.; Harada, N.; Feringa, B. L. Light-Driven Monodirectional Molecular Rotor. *Nature* **1999**, *401* (6749), 152.
- (16) Balzani, V.; Credi, A.; Raymo, F. M.; Stoddart, J. F. Artificial Molecular Machines. *Angew. Chem. Int. Ed.* **2000**, *39* (19), 3348–3391.
- (17) The 2016 Nobel Prize in Chemistry - Press Release  
[http://www.nobelprize.org/nobel\\_prizes/chemistry/laureates/2016/press.html](http://www.nobelprize.org/nobel_prizes/chemistry/laureates/2016/press.html) (accessed Jul 4, 2018).
- (18) The Discovery of Brownian Motion  
[http://web2.uwindsor.ca/courses/physics/high\\_schools/2005/Brownian\\_motion/discovery.html](http://web2.uwindsor.ca/courses/physics/high_schools/2005/Brownian_motion/discovery.html) (accessed May 22, 2018).
- (19) Purcell, E. M. *Life at Low Reynolds Number*; World Scientific, 2014; pp 47–67.
- (20) Sánchez, S.; Soler, L.; Katuri, J. Chemically Powered Micro- and Nanomotors. *Angew. Chem. Int. Ed.* **2015**, *54* (5), 1414–1444.
- (21) Wang, H.; Pumera, M. Fabrication of Micro/Nanoscale Motors. *Chem. Rev.* **2015**, *115* (16), 8704–8735.
- (22) Paxton, W. F.; Kistler, K. C.; Olmeda, C. C.; Sen, A.; St. Angelo, S. K.; Cao, Y.; Mallouk, T. E.; Lammert, P. E.; Crespi, V. H. Catalytic Nanomotors: Autonomous Movement of Striped Nanorods. *J. Am. Chem. Soc.* **2004**, *126* (41), 13424–13431.
- (23) Paxton, W. F.; Baker, P. T.; Kline, T. R.; Wang, Y.; Mallouk, T. E.; Sen, A. Catalytically Induced Electrokinetics for Motors and Micropumps. *J. Am. Chem. Soc.* **2006**, *128* (46), 14881–14888.
- (24) Ma, X.; Jannasch, A.; Albrecht, U.-R.; Hahn, K.; Miguel-López, A.; Schäffer, E.; Sánchez, S. Enzyme-Powered Hollow Mesoporous Janus Nanomotors. *Nano Lett.* **2015**, *15* (10), 7043–7050.
- (25) Howse, J. R.; Jones, R. A. L.; Ryan, A. J.; Gough, T.; Vafabakhsh, R.; Golestanian, R. Self-Motile Colloidal Particles: From Directed Propulsion to Random Walk. *Phys. Rev. Lett.* **2007**, *99* (4), 048102.
- (26) Brown, A.; Poon, W. Ionic Effects in Self-Propelled Pt-Coated Janus Swimmers. *Soft Matter* **2014**, *10* (22), 4016–4027.
- (27) Ebbens, S.; Gregory, D. A.; Dunderdale, G.; Howse, J. R.; Ibrahim, Y.; Liverpool, T. B.; Golestanian, R. Electrokinetic Effects in Catalytic Platinum-Insulator Janus Swimmers. *EPL Europhys. Lett.* **2014**, *106* (5), 58003.
- (28) Patiño, T.; Feiner-Gracia, N.; Arqué, X.; Miguel-López, A.; Jannasch, A.; Stumpp, T.; Schäffer, E.; Albertazzi, L.; Sánchez, S. Influence of Enzyme Quantity and Distribution on the Self-Propulsion of Non-Janus Urease-Powered Micromotors. *J. Am. Chem. Soc.* **2018**, *140* (25), 7896–7903.
- (29) Mei, Y.; Huang, G.; Solovev, A. A.; Ureña, E. B.; Mönch, I.; Ding, F.; Reindl, T.; Fu, R. K. Y.; Chu, P. K.; Schmidt, O. G. Versatile Approach for Integrative and Functionalized Tubes by Strain Engineering of Nanomembranes on Polymers. *Adv. Mater.* **2008**, *20* (21), 4085–4090.

- (30) Zhao, G.; Ambrosi, A.; Pumera, M. Clean Room-Free Rapid Fabrication of Roll-up Self-Powered Catalytic Microengines. *J. Mater. Chem. A* **2014**, *2* (5), 1219–1223.
- (31) Gao, W.; Sattayasamitsathit, S.; Orozco, J.; Wang, J. Highly Efficient Catalytic Microengines: Template Electrosynthesis of Polyaniline/Platinum Microtubes. *J. Am. Chem. Soc.* **2011**, *133* (31), 11862–11864.
- (32) Manjare, M.; Yang, B.; Zhao, Y.-P. Bubble Driven Quasioscillatory Translational Motion of Catalytic Micromotors. *Phys. Rev. Lett.* **2012**, *109* (12), 128305.
- (33) Ma, X.; Jang, S.; Popescu, M. N.; Uspal, W. E.; Miguel-López, A.; Hahn, K.; Kim, D.-P.; Sánchez, S. Reversed Janus Micro/Nanomotors with Internal Chemical Engine. *ACS Nano* **2016**, *10* (9), 8751–8759.
- (34) Chen, X.-Z.; Jang, B.; Ahmed, D.; Hu, C.; Marco, C. D.; Hoop, M.; Mushtaq, F.; Nelson, B. J.; Pané, S. Small-Scale Machines Driven by External Power Sources. *Adv. Mater.* **2018**, *30* (15), 1705061.
- (35) Dreyfus, R.; Baudry, J.; Roper, M. L.; Fermigier, M.; Stone, H. A.; Bibette, J. Microscopic Artificial Swimmers. *Nature* **2005**, *437* (7060), 862–865.
- (36) Hoop, M.; Shen, Y.; Chen, X.-Z.; Mushtaq, F.; Iuliano, L. M.; Sakar, M. S.; Petruska, A.; Loessner, M. J.; Nelson, B. J.; Pané, S. Magnetically Driven Silver-Coated Nanocoils for Efficient Bacterial Contact Killing. *Adv. Funct. Mater.* **2016**, *26* (7), 1063–1069.
- (37) Gao, W.; Sattayasamitsathit, S.; Manesh, K. M.; Weihs, D.; Wang, J. Magnetically Powered Flexible Metal Nanowire Motors. *J. Am. Chem. Soc.* **2010**, *132* (41), 14403–14405.
- (38) Zhang, L.; Abbott, J. J.; Dong, L.; Kratochvil, B. E.; Bell, D.; Nelson, B. J. Artificial Bacterial Flagella: Fabrication and Magnetic Control. *Appl. Phys. Lett.* **2009**, *94* (6), 064107.
- (39) Wong, F.; Sen, A. Progress toward Light-Harvesting Self-Electrophoretic Motors: Highly Efficient Bimetallic Nanomotors and Micropumps in Halogen Media. *ACS Nano* **2016**, *10* (7), 7172–7179.
- (40) Dong, R.; Zhang, Q.; Gao, W.; Pei, A.; Ren, B. Highly Efficient Light-Driven TiO<sub>2</sub>-Au Janus Micromotors. *ACS Nano* **2016**, *10* (1), 839–844.
- (41) Dai, B.; Wang, J.; Xiong, Z.; Zhan, X.; Dai, W.; Li, C.-C.; Feng, S.-P.; Tang, J. Programmable Artificial Phototactic Microswimmer. *Nat. Nanotechnol.* **2016**, *11* (12), 1087–1092.
- (42) Hong, Y.; Diaz, M.; Córdova-Figueroa, U. M.; Sen, A. Light-Driven Titanium-Dioxide-Based Reversible Microfireworks and Micromotor/Micropump Systems. *Adv. Funct. Mater.* **2010**, *20* (10), 1568–1576.
- (43) Jang, B.; Hong, A.; Kang, H. E.; Alcantara, C.; Charreyron, S.; Mushtaq, F.; Pellicer, E.; Büchel, R.; Sort, J.; Lee, S. S.; et al. Multiwavelength Light-Responsive Au/B-TiO<sub>2</sub> Janus Micromotors. *ACS Nano* **2017**, *11* (6), 6146–6154.
- (44) Wang, X.; Sridhar, V.; Guo, S.; Talebi, N.; Miguel-López, A.; Hahn, K.; Aken, P. A. van; Sánchez, S. Fuel-Free Nanocap-Like Motors Actuated Under Visible Light. *Adv. Funct. Mater.* **2015**, *25* (25), 1705862.

- (45) Wang, W.; Castro, L. A.; Hoyos, M.; Mallouk, T. E. Autonomous Motion of Metallic Microrods Propelled by Ultrasound. *ACS Nano* **2012**, *6* (7), 6122–6132.
- (46) Kagan, D.; Benchimol, M. J.; Claussen, J. C.; Chuluun-Erdene, E.; Esener, S.; Wang, J. Acoustic Droplet Vaporization and Propulsion of Perfluorocarbon-Loaded Microbullets for Targeted Tissue Penetration and Deformation. *Angew. Chem.* *124* (30), 7637–7640.
- (47) Jiang, H.-R.; Yoshinaga, N.; Sano, M. Active Motion of a Janus Particle by Self-Thermophoresis in a Defocused Laser Beam. *Phys. Rev. Lett.* **2010**, *105* (26).
- (48) Loget, G.; Kuhn, A. Electric Field-Induced Chemical Locomotion of Conducting Objects. *Nat. Commun.* **2011**, *2*, 535.
- (49) Magdanz, V.; Sanchez, S.; Schmidt, O. G. Development of a Sperm-Flagella Driven Micro-Bio-Robot. *Adv. Mater.* **2013**, *25* (45), 6581–6588.
- (50) Stanton, M. M.; Park, B.-W.; Miguel-López, A.; Ma, X.; Sitti, M.; Sánchez, S. Biohybrid Microtube Swimmers Driven by Single Captured Bacteria. *Small* **2017**, *13* (19), 1603679.
- (51) Li, J.; Ávila, B. E.-F. de; Gao, W.; Zhang, L.; Wang, J. Micro/Nanorobots for Biomedicine: Delivery, Surgery, Sensing, and Detoxification. *Sci. Robot.* **2017**, *2* (4), eaam6431.
- (52) Soler, L.; Martínez-Cisneros, C.; Swiersy, A.; Sánchez, S.; G. Schmidt, O. Thermal Activation of Catalytic Microjets in Blood Samples Using Microfluidic Chips. *Lab. Chip* **2013**, *13* (22), 4299–4303.
- (53) Zhao, G.; Viehrig, M.; Pumera, M. Challenges of the Movement of Catalytic Micromotors in Blood. *Lab. Chip* **2013**, *13* (10), 1930–1936.
- (54) Prinz, V. Y.; Seleznev, V. A.; Gutakovskiy, A. K.; Chehovskiy, A. V.; Preobrazhenskii, V. V.; Putyato, M. A.; GavriloVA, T. A. Free-Standing and Overgrown InGaAs/GaAs Nanotubes, Nanohelices and Their Arrays. *Phys. E Low-Dimens. Syst. Nanostructures* **2**, *6* (1–4), 828–831.
- (55) Schmidt, O. G.; Eberl, K. Nanotechnology: Thin Solid Films Roll up into Nanotubes. *Nature* **2001**, *410* (6825), 168–168.
- (56) Vaccaro, P. O.; Kubota, K.; Aida, T. Strain-Driven Self-Positioning of Micromachined Structures. *Appl. Phys. Lett.* **2001**, *78* (19), 2852–2854.
- (57) Huang, G.; Mei, Y. Thinning and Shaping Solid Films into Functional and Integrative Nanomembranes. *Adv. Mater.* **2012**, *24* (19), 2517–2546.
- (58) Huang, M.; Cavallo, F.; Liu, F.; Lagally, M. G. Nanomechanical Architecture of Semiconductor Nanomembranes. *Nanoscale* **2011**, *3* (1), 96–120.
- (59) Hawkeye, M. M.; Taschuk, M. T.; Brett, M. J. *Glancing Angle Deposition of Thin Films: Engineering the Nanoscale*; John Wiley & Sons, 2014.
- (60) Parmar, J.; Vilela, D.; Sanchez, S. Tubular Microjets: Fabrication, Factors Affecting the Motion and Mechanism of Propulsion. *Eur. Phys. J. Spec. Top.* **2016**, *225* (11–12), 2255–2267.
- (61) Li, J.; Singh, V. V.; Sattayasamitsathit, S.; Orozco, J.; Kaufmann, K.; Dong, R.; Gao, W.; Jurado-Sanchez, B.; Fedorak, Y.; Wang, J. Water-

- Driven Micromotors for Rapid Photocatalytic Degradation of Biological and Chemical Warfare Agents. *ACS Nano* **2014**, 8 (11), 11118–11125.
- (62) Manjare, M.; Yang, B.; Zhao, Y.-P. Bubble-Propelled Microjets: Model and Experiment. *J. Phys. Chem. C* **2013**, 117 (9), 4657–4665.
- (63) Li, L.; Wang, J.; Li, T.; Song, W.; Zhang, G. A Unified Model of Drag Force for Bubble-Propelled Catalytic Micro/Nano-Motors with Different Geometries in Low Reynolds Number Flows. *J. Appl. Phys.* **2015**, 117 (10), 104308.
- (64) Fomin, V. M.; Hippler, M.; Magdanz, V.; Soler, L.; Sanchez, S.; Schmidt, O. G. Propulsion Mechanism of Catalytic Microjet Engines. *IEEE Trans. Robot.* **2014**, 30 (1), 40–48.
- (65) Guix, M.; Mayorga-Martinez, C. C.; Merkoçi, A. Nano/Micromotors in (Bio)Chemical Science Applications. *Chem. Rev.* **2014**, 114 (12), 6285–6322.
- (66) Wang, J. *Nanomachines: Fundamentals and Applications*; John Wiley & Sons, 2013.
- (67) Guix, M.; Orozco, J.; García, M.; Gao, W.; Sattayasamitsathit, S.; Merkoçi, A.; Escarpa, A.; Wang, J. Superhydrophobic Alkanethiol-Coated Microsubmarines for Effective Removal of Oil. *ACS Nano* **2012**, 6 (5), 4445–4451.
- (68) Gao, W.; Feng, X.; Pei, A.; Gu, Y.; Li, J.; Wang, J. Seawater-Driven Magnesium Based Janus Micromotors for Environmental Remediation. *Nanoscale* **2013**, 5 (11), 4696–4700.
- (69) Soler, L.; Magdanz, V.; Fomin, V. M.; Sanchez, S.; Schmidt, O. G. Self-Propelled Micromotors for Cleaning Polluted Water. *ACS Nano* **2013**, 7 (11), 9611–9620.
- (70) Li, J.; Singh, V. V.; Sattayasamitsathit, S.; Orozco, J.; Kaufmann, K.; Dong, R.; Gao, W.; Jurado-Sanchez, B.; Fedorak, Y.; Wang, J. Water-Driven Micromotors for Rapid Photocatalytic Degradation of Biological and Chemical Warfare Agents. *ACS Nano* **2014**, 8 (11), 11118–11125.
- (71) Mushtaq, F.; Guerrero, M.; Sakar, M. S.; Hoop, M.; Lindo, A. M.; Sort, J.; Chen, X.; Nelson, B. J.; Pellicer, E.; Pane, S. Magnetically Driven Bi<sub>2</sub>O<sub>3</sub>/BiOCl-Based Hybrid Microrobots for Photocatalytic Water Remediation. *J. Mater. Chem. A* **2015**, 3 (47), 23670–23676.
- (72) Singh, V. V.; Martin, A.; Kaufmann, K.; D. S. de Oliveira, S.; Wang, J. Zirconia/Graphene Oxide Hybrid Micromotors for Selective Capture of Nerve Agents. *Chem. Mater.* **2015**, 27 (23), 8162–8169.
- (73) Singh Virendra V.; Jurado-Sánchez Beatriz; Sattayasamitsathit Sirilak; Orozco Jahir; Li Jinxing; Galarnyk Michael; Fedorak Yuri; Wang Joseph. Multifunctional Silver-Exchanged Zeolite Micromotors for Catalytic Detoxification of Chemical and Biological Threats. *Adv. Funct. Mater.* **2015**, 25 (14), 2147–2155.
- (74) Kiristi, M.; Singh, V. V.; Esteban-Fernández de Ávila, B.; Uygun, M.; Soto, F.; Aktaş Uygun, D.; Wang, J. Lysozyme-Based Antibacterial Nanomotors. *ACS Nano* **2015**, 9 (9), 9252–9259.

- (75) Campuzano, S.; Orozco, J.; Kagan, D.; Guix, M.; Gao, W.; Sattayasamitsathit, S.; Claussen, J. C.; Merkoçi, A.; Wang, J. Bacterial Isolation by Lectin-Modified Microengines. *Nano Lett.* **2012**, *12* (1), 396–401.
- (76) Uygun, M.; Singh, V. V.; Kaufmann, K.; Uygun, D. A.; de Oliveira, S. D. S.; Wang, J. Micromotor-Based Biomimetic Carbon Dioxide Sequestration: Towards Mobile Microscrubbers. *Angew. Chem. Int. Ed.* **2015**, *54* (44), 12900–12904.
- (77) Orozco, J.; Jurado-Sánchez, B.; Wagner, G.; Gao, W.; Vazquez-Duhalt, R.; Sattayasamitsathit, S.; Galarnyk, M.; Cortés, A.; Saintillan, D.; Wang, J. Bubble-Propelled Micromotors for Enhanced Transport of Passive Tracers. *Langmuir* **2014**, *30* (18), 5082–5087.
- (78) Risso, F. Agitation, Mixing, and Transfers Induced by Bubbles. *Annu. Rev. Fluid Mech.* **2018**, *50* (1), 25–48.
- (79) Singh, V. V.; Soto, F.; Kaufmann, K.; Wang, J. Micromotor-Based Energy Generation. *Angew. Chem.* **2015**.
- (80) Moo, J. G. S.; Wang, H.; Pumera, M. Acetylene Bubble-Powered Autonomous Capsules: Towards in Situ Fuel. *Chem. Commun.* **2014**, *50* (100), 15849–15851.
- (81) Guix, M.; Mayorga-Martinez, C. C.; Merkoçi, A. Nano/Micromotors in (Bio)Chemical Science Applications. *Chem. Rev.* **2014**, *114* (12), 6285–6322.
- (82) Brillas, E.; Sirés, I.; Oturan, M. A. Electro-Fenton Process and Related Electrochemical Technologies Based on Fenton's Reaction Chemistry. *Chem. Rev.* **2009**, *109* (12), 6570–6631.
- (83) Goti, A.; Cardona, F. Hydrogen Peroxide in Green Oxidation Reactions: Recent Catalytic Processes. In *Green Chemical Reactions*; Tundo, P., Esposito, V., Eds.; NATO Science for Peace and Security Series; Springer Netherlands, 2008; pp 191–212.
- (84) Noyori, R.; Aoki, M.; Sato, K. Green Oxidation with Aqueous Hydrogen Peroxide. *Chem. Commun.* **2003**, No. 16, 1977–1986.
- (85) Neyens, E.; Baeyens, J. A Review of Classic Fenton's Peroxidation as an Advanced Oxidation Technique. *J. Hazard. Mater.* **2003**, *98* (1), 33–50.
- (86) Oller, I.; Malato, S.; Sánchez-Pérez, J. Combination of Advanced Oxidation Processes and Biological Treatments for Wastewater Decontamination—a Review. *Sci. Total Environ.* **2011**, *409* (20), 4141–4166.
- (87) Bokare, A. D.; Choi, W. Review of Iron-Free Fenton-like Systems for Activating H<sub>2</sub>O<sub>2</sub> in Advanced Oxidation Processes. *J. Hazard. Mater.* **6**, 275, 121–135.
- (88) Babuponnusami, A.; Muthukumar, K. A Review on Fenton and Improvements to the Fenton Process for Wastewater Treatment. *J. Environ. Chem. Eng.* **2014**, *2* (1), 557–572.
- (89) Pereira, M.; Oliveira, L.; Murad, E. Iron Oxide Catalysts: Fenton and Fenton-like Reactions—a Review. *Clay Miner.* **2012**, *47* (3), 285–302.

- (90) Hsueh, C.; Huang, Y.; Wang, C.; Chen, C.-Y. Degradation of Azo Dyes Using Low Iron Concentration of Fenton and Fenton-like System. *Chemosphere* **2005**, *58* (10), 1409–1414.
- (91) Gomathi Devi, L.; Girish Kumar, S.; Mohan Reddy, K.; Munikrishnappa, C. Photo Degradation of Methyl Orange an Azo Dye by Advanced Fenton Process Using Zero Valent Metallic Iron: Influence of Various Reaction Parameters and Its Degradation Mechanism. *J. Hazard. Mater.* **2009**, *164* (2–3), 459–467.
- (92) Khalil, I. S.; Magdanz, V.; Sanchez, S.; Schmidt, O. G.; Misra, S.; Ben-Jacob, E. Wireless Magnetic-Based Closed-Loop Control of Self-Propelled Microjets. *PLoS One* **2014**, *9* (2), e83053.
- (93) Hameed, B. H.; Lee, T. W. Degradation of Malachite Green in Aqueous Solution by Fenton Process. *J. Hazard. Mater.* **2009**, *164* (2–3), 468–472.
- (94) Scheffe, J. R.; Francés, A.; King, D. M.; Liang, X.; Branch, B. A.; Cavanagh, A. S.; George, S. M.; Weimer, A. W. Atomic Layer Deposition of Iron(III) Oxide on Zirconia Nanoparticles in a Fluidized Bed Reactor Using Ferrocene and Oxygen. *Thin Solid Films* **2009**, *517* (6), 1874–1879.
- (95) Srivastava, N.; Shripathi, T.; Srivastava, P. C. Core Level X-Ray Photoelectron Spectroscopy Study of Exchange Coupled Fe/NiO Bilayer Interfaced with Si Substrate (Fe/NiO–NSi Structure). *J. Electron Spectrosc. Relat. Phenom.* **2013**, *191*, 20–26.
- (96) Descostes, M.; Mercier, F.; Thromat, N.; Beaucaire, C.; Gautier-Soyer, M. Use of XPS in the Determination of Chemical Environment and Oxidation State of Iron and Sulfur Samples: Constitution of a Data Basis in Binding Energies for Fe and S Reference Compounds and Applications to the Evidence of Surface Species of an Oxidized Pyrite in a Carbonate Medium. *Appl. Surf. Sci.* **2000**, *165* (4), 288–302.
- (97) Luo, Y.-D.; Lin, Y.-H.; Zhang, X.; Liu, D.; Shen, Y.; Nan, C.-W.; Luo, Y.-D.; Lin, Y.-H.; Zhang, X.; Liu, D.; et al. Ferromagnetic Behaviors in Fe-Doped NiO Nanofibers Synthesized by Electrospinning Method, Ferromagnetic Behaviors in Fe-Doped NiO Nanofibers Synthesized by Electrospinning Method. *J. Nanomater. J. Nanomater.* **2013**, *2013*, 2013, e252593.
- (98) Cabello, G.; Araneda, A.; Lillo, L.; Caro, C.; Venegas, C.; Tejos, M.; Chornik, B. Application of Photochemical Method in the Synthesis of Ga<sub>2</sub>O<sub>3</sub>–X Thin Films Co-Doped with Terbium and Europium. *Solid State Sci.* **2014**, *27*, 24–29.
- (99) Fu, F.; Wang, Q. Removal of Heavy Metal Ions from Wastewaters: A Review. *J. Environ. Manage.* **3**, 92 (3), 407–418.
- (100) Ali, I. New Generation Adsorbents for Water Treatment. *Chem. Rev.* **2012**, *112* (10), 5073–5091.
- (101) Zhao, G.; Li, J.; Ren, X.; Chen, C.; Wang, X. Few-Layered Graphene Oxide Nanosheets As Superior Sorbents for Heavy Metal Ion Pollution Management. *Environ. Sci. Technol.* **2011**, *45* (24), 10454–10462.

- (102) Cong, H.-P.; Ren, X.-C.; Wang, P.; Yu, S.-H. Macroscopic Multifunctional Graphene-Based Hydrogels and Aerogels by a Metal Ion Induced Self-Assembly Process. *ACS Nano* **2012**, *6* (3), 2693–2703.
- (103) Huang, Z.-H.; Zheng, X.; Lv, W.; Wang, M.; Yang, Q.-H.; Kang, F. Adsorption of Lead(II) Ions from Aqueous Solution on Low-Temperature Exfoliated Graphene Nanosheets. *Langmuir* **2011**, *27* (12), 7558–7562.
- (104) Orozco, J.; García-Gradilla, V.; D'Agostino, M.; Gao, W.; Cortés, A.; Wang, J. Artificial Enzyme-Powered Microfish for Water-Quality Testing. *ACS Nano* **2013**, *7* (1), 818–824.
- (105) Moo, J. G. S.; Wang, H.; Zhao, G.; Pumera, M. Biomimetic Artificial Inorganic Enzyme-Free Self-Propelled Microfish Robot for Selective Detection of Pb<sup>2+</sup> in Water. *Chem.- Eur. J.* **2014**, *20* (15), 4292–4296.
- (106) Dey, K. K.; Bhandari, S.; Bandyopadhyay, D.; Basu, S.; Chattopadhyay, A. The PH Taxis of an Intelligent Catalytic Microbot. *Small* **2013**, *9* (11), 1916–1920.
- (107) Vilela, D.; Orozco, J.; Cheng, G.; Sattayasamitsathit, S.; Galarnyk, M.; Kan, C.; Wang, J.; Escarpa, A. Multiplexed Immunoassay Based on Micromotors and Microscale Tags. *Lab. Chip* **2014**, *14* (18), 3505–3509.
- (108) Esteban-Fernández de Ávila, B.; Lopez-Ramirez, M. A.; Báez, D. F.; Jodra, A.; Singh, V. V.; Kaufmann, K.; Wang, J. Aptamer-Modified Graphene-Based Catalytic Micromotors: Off-On Fluorescent Detection of Ricin. *ACS Sens.* **2016**.
- (109) Moreno-Guzman, M.; Jodra, A.; López, M.-Á.; Escarpa, A. Self-Propelled Enzyme-Based Motors for Smart Mobile Electrochemical and Optical Biosensing. *Anal. Chem.* **2015**, *87* (24), 12380–12386.
- (110) Moo, J. G. S.; Khezri, B.; Webster, R. D.; Pumera, M. Graphene Oxides Prepared by Hummers', Hofmann's, and Staudenmaier's Methods: Dramatic Influences on Heavy-Metal-Ion Adsorption. *ChemPhysChem* **2014**, *15* (14), 2922–2929.
- (111) Zhao, G.; Ren, X.; Gao, X.; Tan, X.; Li, J.; Chen, C.; Huang, Y.; Wang, X. Removal of Pb(II) Ions from Aqueous Solutions on Few-Layered Graphene Oxide Nanosheets. *Dalton Trans.* **2011**, *40* (41), 10945–10952.
- (112) Li, Q.; Mahendra, S.; Lyon, D. Y.; Brunet, L.; Liga, M. V.; Li, D.; Alvarez, P. J. J. Antimicrobial Nanomaterials for Water Disinfection and Microbial Control: Potential Applications and Implications. *Water Res* **2008**, *42*, 4591.
- (113) Koivunen, J.; Heinonen-Tanski, H. Inactivation of Enteric Microorganisms with Chemical Disinfectants, Uv Irradiation and Combined Chemical/Uv Treatments. *Water Res* **2005**, *39*, 1519.
- (114) Wolfe, R. L. Ultraviolet Disinfection of Potable Water. *Env. Sci Technol* **1990**, *24*, 768.
- (115) Anpilov, A. M.; Barkhudarov, E. M.; Christofi, N.; Kop'ev, V. A.; Kossyi, I. A.; Taktakishvili, M. I.; Zadiraka, Y. Pulsed High Voltage Electric Discharge Disinfection of Microbially Contaminated Liquids. *Lett Appl Microbiol* **2002**, *35*, 90.

- (116) Cappelli, G.; Riccardi, M.; Perrone, S.; Bondi, M.; Ligabue, G.; Albertazzi, A. Water Treatment and Monitor Disinfection. *Hemodial Int* **2006**, *10*, S13.
- (117) Krasner, S. W. Occurrence of a New Generation of Disinfection Byproducts. *Env. Sci Technol* **2006**, *40*, 7175.
- (118) Delezuk, J. A. M.; Ramírez-Herrera, D. E.; Ávila, B. E.-F. de; Wang, J. Chitosan-Based Water-Propelled Micromotors with Strong Antibacterial Activity. *Nanoscale* **2017**, *9* (6), 2195–2200.
- (119) Ge, Y.; Liu, M.; Liu, L.; Sun, Y.; Zhang, H.; Dong, B. Dual-Fuel-Driven Bactericidal Micromotor. *Nano-Micro Lett.* **2016**, *8* (2), 157–164.
- (120) Castellano, J. J.; Shafii, S. M.; Ko, F.; Donate, G.; Wright, T. E.; Mannari, R. J.; Payne, W. G.; Smith, D. J.; Robson, M. C. Comparative Evaluation of Silver-Containing Antimicrobial Dressings and Drugs. *Int Wound J* **2007**, *4*, 114.
- (121) Chen, X.; Schluesener, H. J. Nanosilver: A Nanoproduct in Medical Application. *Toxicol Lett* **2008**, *176*, 1.
- (122) Quadros, M. E.; Marr, L. C. Silver Nanoparticles and Total Aerosols Emitted by Nanotechnology-Related Consumer Spray Products. *Env. Sci Technol* **2011**, *45*, 10713.
- (123) Xiu, Z. -m.; Zhang, Q. -b.; Puppala, H. L.; Colvin, V. L.; Alvarez, P. J. J. Negligible Particle-Specific Antibacterial Activity of Silver Nanoparticles. *Nano Lett* **2012**, *12*, 4271.
- (124) Lara, H. H.; Ayala-Núñez, N. V.; Ixtepan Turrent, L. d. C.; Rodríguez Padilla, C. Bactericidal Effect of Silver Nanoparticles against Multidrug-Resistant Bacteria. *World J Microbiol Biotechnol* **2010**, *26*, 615.
- (125) Morones-Ramirez, J. R.; Winkler, J. A.; Spina, C. S.; Collins, J. J. Silver Enhances Antibiotic Activity against Gram-Negative Bacteria. *Sci Transl Med* **2013**, *5*, 190ra81.
- (126) Rai, M.; Yadav, A.; Gade, A. Silver Nanoparticles as a New Generation of Antimicrobials. *Biotechnol Adv* **2009**, *27*, 76.
- (127) Sondi, I.; Salopek-Sondi, B. Silver Nanoparticles as Antimicrobial Agent: A Case Study on E. Coli as A Model for Gram-Negative Bacteria. *J Colloid Interface Sci* **2004**, *275*, 177.
- (128) Kemper, M. A.; Urrutia, M. M.; Beveridge, T. J.; Koch, A. L.; Doyle, R. J. Proton Motive Force May Regulate Cell Wall-Associated Enzymes of Bacillus Subtilis. *J Bacteriol* **1993**, *175*, 5690.
- (129) Koch, A. L. The Ph in the Neighborhood of Membranes Generating a Protonmotive Force. *J Theor Biol* **1986**, *120*, 73.
- (130) Xiu, Z.-M.; Ma, J.; Alvarez, P. J. J. Differential Effect of Common Ligands and Molecular Oxygen on Antimicrobial Activity of Silver Nanoparticles Versus Silver Ions. *Env. Sci Technol* **2011**, *45*, 9003.
- (131) Agnihotri, S.; Mukherji, S.; Mukherji, S. Immobilized Silver Nanoparticles Enhance Contact Killing and Show Highest Efficacy: Elucidation of the Mechanism of Bactericidal Action of Silver. *Nanoscale* **2013**, *5*, 7328.
- (132) Tuson, H. H.; Weibel, D. B. Bacteria-Surface Interactions. *Soft Matter* **2013**, *9*, 4368.

- (133) Stanton, M. M.; Simmchen, J.; Ma, X.; Miguel-López, A.; Sánchez, S. Biohybrid Janus Motors Driven by Escherichia Coli. *Adv. Mater. Interfaces* **3** (2), 1500505.
- (134) Ahlberg, S.; Antonopoulos, A.; Diendorf, J.; Dringen, R.; Epple, M.; Flöck, R.; Goedecke, W.; Graf, C.; Haberl, N.; Helmlinger, J.; et al. Pvp-Coated, Negatively Charged Silver Nanoparticles: A Multi-Center Study of Their Physicochemical Characteristics, Cell Culture and in Vivo Experiments. *Beilstein J Nanotechnol* **2014**, *5*, 1944.
- (135) Edberg, S. C.; Rice, E. W.; Karlin, R. J.; Allen, M. J. Escherichia Coli: The Best Biological Drinking Water Indicator for Public Health Protection. *J Appl Microbiol* **2000**, *88*, 106S.
- (136) Jucker, B. A.; Harms, H.; Zehnder, A. J. Adhesion of the Positively Charged Bacterium Stenotrophomonas (Xanthomonas) Maltophilia 70401 to Glass and Teflon. *J Bacteriol* **1996**, *178*, 5472.
- (137) Harkes, G.; Feijen, J.; Dankert, J. Adhesion of Escherichia Coli on to a Series of Poly(Methacrylates) Differing in Charge and Hydrophobicity. *Biomaterials* **1991**, *12*, 853.
- (138) El Badawy, A. M.; Silva, R. G.; Morris, B.; Scheckel, K. G.; Suidan, M. T.; Tolaymat, T. M. Surface Charge-Dependent Toxicity of Silver Nanoparticles. *Env. Sci Technol* **2011**, *45*, 283.
- (139) Baraban, L.; Makarov, D.; Streubel, R.; Mönch, I.; Grimm, D.; Sanchez, S.; Schmidt, O. G. Catalytic Janus Motors on Microfluidic Chip: Deterministic Motion for Targeted Cargo Delivery. *ACS Nano* **2012**, *6*, 3383.
- (140) Liu, L.; Liu, M.; Su, Y.; Dong, Y.; Zhou, W.; Zhang, L.; Zhang, H.; Dong, B.; Chi, L. Tadpole-Like Artificial Micromotor. *Nanoscale* **2015**, *7*, 2276.
- (141) Safdar, M.; Wani, O. M.; Jänis, J. Manganese Oxide-Based Chemically Powered Micromotors. *ACS Appl. Mater. Interfaces* **2015**, *7* (46), 25580–25585.
- (142) Maria-Hormigos, R.; Jurado-Sanchez, B.; Vazquez, L.; Escarpa, A. Carbon Allotrope Nanomaterials Based Catalytic Micromotors. *Chem. Mater.* **2016**, *28* (24), 8962–8970.
- (143) Wang, H.; Zhao, G.; Pumera, M. Beyond Platinum: Bubble-Propelled Micromotors Based on Ag and MnO<sub>2</sub> Catalysts. *J. Am. Chem. Soc.* **2014**, *136* (7), 2719–2722.
- (144) Ye, H.; Sun, H.; Wang, S. Electrochemical Synthesis of Graphene/MnO<sub>2</sub> in an Architecture of Bilayer Microtubes as Micromotors. *Chem. Eng. J.* **2017**, *324*, 251–258.
- (145) Feng, X.; Zhang, Y.; Li, Y.; Huang, Z.; Chen, S.; Ma, Y.; Zhang, L.; Wang, L.; Yan, X. Graphene-Based Highly Efficient Micromotors. *Chem. Lett.* **2014**, *44* (3), 399–401.
- (146) Li, J.; Yu, X.; Xu, M.; Liu, W.; Sandraz, E.; Lan, H.; Wang, J.; Cohen, S. M. Metal–Organic Frameworks as Micromotors with Tunable Engines and Brakes. *J. Am. Chem. Soc.* **2017**, *139* (2), 611–614.
- (147) Mou, F.; Pan, D.; Chen, C.; Gao, Y.; Xu, L.; Guan, J. Magnetically Modulated Pot-Like MnFe<sub>2</sub>O<sub>4</sub> Micromotors: Nanoparticle Assembly

- Fabrication and Their Capability for Direct Oil Removal. *Adv. Funct. Mater.* **2015**, 25 (39), 6173–6181.
- (148) Vilela, D.; Parmar, J.; Zeng, Y.; Zhao, Y.; Sánchez, S. Graphene-Based Microbots for Toxic Heavy Metal Removal and Recovery from Water. *Nano Lett.* **2016**, 16 (4), 2860–2866.
- (149) Uygun, D. A.; Jurado-Sánchez, B.; Uygun, M.; Wang, J. Self-Propelled Chelation Platforms for Efficient Removal of Toxic Metals. *Environ. Sci. Nano* **2016**, 3 (3), 559–566.
- (150) Orozco, J.; Cheng, G.; Vilela, D.; Sattayasamitsathit, S.; Vazquez-Duhalt, R.; Valdés-Ramírez, G.; Pak, O. S.; Escarpa, A.; Kan, C.; Wang, J. Micromotor-Based High-Yielding Fast Oxidative Detoxification of Chemical Threats. *Angew. Chem. Int. Ed.* **2013**, 52 (50), 13276–13279.
- (151) Parmar, J.; Vilela, D.; Pellicer, E.; Esqué-de los Ojos, D.; Sort, J.; Sánchez, S. Reusable and Long-Lasting Active Microcleaners for Heterogeneous Water Remediation. *Adv. Funct. Mater.* **2016**, 26 (23), 4152–4161.
- (152) Orozco, J.; Mercante, L. A.; Pol, R.; Merkoci, A. Graphene-Based Janus Micromotors for the Dynamic Removal of Pollutants. *J. Mater. Chem. A* **2016**.
- (153) Xuan, M.; Lin, X.; Shao, J.; Dai, L.; He, Q. Motion-Based, High-Yielding, and Fast Separation of Different Charged Organics in Water. *ChemPhysChem* **2015**, 16 (1), 147–151.
- (154) Mushtaq, F.; Asani, A.; Hoop, M.; Chen, X.-Z.; Ahmed, D.; Nelson, B. J.; Pané, S. Highly Efficient Coaxial TiO<sub>2</sub>-PtPd Tubular Nanomachines for Photocatalytic Water Purification with Multiple Locomotion Strategies. *Adv. Funct. Mater.* **2016**, 26 (38), 6995–7002.
- (155) Mou, F.; Pan, D.; Chen, C.; Gao, Y.; Xu, L.; Guan, J. Magnetically Modulated Pot-Like MnFe<sub>2</sub>O<sub>4</sub> Micromotors: Nanoparticle Assembly Fabrication and Their Capability for Direct Oil Removal. *Adv. Funct. Mater.* **2015**, 25 (39), 6173–6181.
- (156) Vilela, D.; Stanton, M. M.; Parmar, J.; Sánchez, S. Microbots Decorated with Silver Nanoparticles Kill Bacteria in Aqueous Media. *ACS Appl. Mater. Interfaces* **2017**, 9 (27), 22093–22100.
- (157) Wang, H.; Zhao, G.; Pumera, M. Beyond Platinum: Bubble-Propelled Micromotors Based on Ag and MnO<sub>2</sub> Catalysts. *J. Am. Chem. Soc.* **2014**, 136 (7), 2719–2722.
- (158) Teo, W. Z.; Zboril, R.; Medrik, I.; Pumera, M. Fe<sub>0</sub> Nanomotors in Ton Quantities (1020 Units) for Environmental Remediation. *Chem. – Eur. J.* **2016**, n/a-n/a.
- (159) Wani, O. M.; Safdar, M.; Kinnunen, N.; Jänis, J. Dual Effect of Manganese Oxide Micromotors: Catalytic Degradation and Adsorptive Bubble Separation of Organic Pollutants. *Chem. Eur. J.* **2015**.
- (160) Villa, K.; Parmar, J.; Vilela, D.; Sánchez, S. Metal-Oxide-Based Microjets for the Simultaneous Removal of Organic Pollutants and Heavy Metals. *ACS Appl. Mater. Interfaces* **2018**, 10 (24), 20478–20486.
- (161) Barb, W.; Baxendale, J.; George, P.; Hargrave, K. Reactions of Ferrous and Ferric Ions with Hydrogen Peroxide. *Nature* **1949**, 163 (4148), 692–694.

- (162) Klavarioti, M.; Mantzavinos, D.; Kassinos, D. Removal of Residual Pharmaceuticals from Aqueous Systems by Advanced Oxidation Processes. *Environ. Int.* **2009**, *35* (2), 402–417.
- (163) Sirés, I.; Brillas, E. Remediation of Water Pollution Caused by Pharmaceutical Residues Based on Electrochemical Separation and Degradation Technologies: A Review. *Environ. Int.* **2012**, *40*, 212–229.
- (164) Luo, Y.; Guo, W.; Ngo, H. H.; Nghiem, L. D.; Hai, F. I.; Zhang, J.; Liang, S.; Wang, X. C. A Review on the Occurrence of Micropollutants in the Aquatic Environment and Their Fate and Removal during Wastewater Treatment. *Sci. Total Environ.* **2014**, *473*, 619–641.
- (165) Le-Minh, N.; Khan, S. J.; Drewes, J. E.; Stuetz, R. M. Fate of Antibiotics during Municipal Water Recycling Treatment Processes. *Water Res.* **2010**, *44* (15), 4295–4323.
- (166) Daghri, R.; Drogui, P. Tetracycline Antibiotics in the Environment: A Review. *Environ. Chem. Lett.* **2013**, *11* (3), 209–227.
- (167) Deng, H.; Li, X.; Peng, Q.; Wang, X.; Chen, J.; Li, Y. Monodisperse Magnetic Single-Crystal Ferrite Microspheres. *Angew. Chem. Int. Ed.* **2005**, *44* (18), 2782–2785.
- (168) Dai, Q.; Lam, M.; Swanson, S.; Yu, R.-H. R.; Milliron, D. J.; Topuria, T.; Jubert, P.-O.; Nelson, A. Monodisperse Cobalt Ferrite Nanomagnets with Uniform Silica Coatings. *Langmuir* **2010**, *26* (22), 17546–17551.
- (169) Kendall, K.; Weihs, T. P. Adhesion of Nanoparticles within Spray Dried Agglomerates. *J. Phys. Appl. Phys.* **1992**, *25* (1A), A3.
- (170) Maskara, A.; Smith, D. M. Agglomeration during the Drying of Fine Silica Powders, Part II: The Role of Particle Solubility. *J. Am. Ceram. Soc.* **1997**, *80* (7), 1715–1722.
- (171) Sanchez, S.; Solovev, A. A.; Harazim, S. M.; Deneke, C.; Feng Mei, Y.; Schmidt, O. G. The Smallest Man-Made Jet Engine. *Chem. Rec.* **2011**, *11* (6), 367–370.
- (172) Simmchen, J.; Magdanz, V.; Sanchez, S.; Chokmaviroj, S.; Ruiz-Molina, D.; Baeza, A.; Schmidt, O. G. Effect of Surfactants on the Performance of Tubular and Spherical Micromotors – a Comparative Study. *RSC Adv.* **2014**, *4* (39), 20334–20340.
- (173) Wang, H.; Zhao, G.; Pumera, M. Crucial Role of Surfactants in Bubble-Propelled Microengines. *J. Phys. Chem. C* **2014**, *118* (10), 5268–5274.
- (174) Lechuga, M.; Fernández-Serrano, M.; Jurado, E.; Núñez-Olea, J.; Ríos, F. Acute Toxicity of Anionic and Non-Ionic Surfactants to Aquatic Organisms. *Ecotoxicol. Environ. Saf.* **2016**, *125*, 1–8.
- (175) Yüksel, E.; Şengil, İ. A.; Özacar, M. The Removal of Sodium Dodecyl Sulfate in Synthetic Wastewater by Peroxi-Electrocoagulation Method. *Chem. Eng. J.* **2009**, *152* (2), 347–353.
- (176) Dang, X.; Hu, C.; Wei, Y.; Chen, W.; Hu, S. Sensitivity Improvement of the Oxidation of Tetracycline at Acetylene Black Electrode in the Presence of Sodium Dodecyl Sulfate. *Electroanalysis* **2004**, *16* (23), 1949–1955.
- (177) Barhoumi, N.; Olvera-Vargas, H.; Oturan, N.; Huguenot, D.; Gadri, A.; Ammar, S.; Brillas, E.; Oturan, M. A. Kinetics of Oxidative

- Degradation/Mineralization Pathways of the Antibiotic Tetracycline by the Novel Heterogeneous Electro-Fenton Process with Solid Catalyst Chalcopyrite. *Appl. Catal. B Environ.* **2017**, *209*, 637–647.
- (178) Costa, R. C. C.; Lelis, M. F. F.; Oliveira, L. C. A.; Fabris, J. D.; Ardisson, J. D.; Rios, R. R. V. A.; Silva, C. N.; Lago, R. M. Novel Active Heterogeneous Fenton System Based on  $\text{Fe}_3\text{-xMxO}_4$  (Fe, Co, Mn, Ni): The Role of  $\text{M}^{2+}$  Species on the Reactivity towards  $\text{H}_2\text{O}_2$  Reactions. *J. Hazard. Mater.* **2006**, *129* (1), 171–178.
- (179) He, J.; Yang, X.; Men, B.; Wang, D. Interfacial Mechanisms of Heterogeneous Fenton Reactions Catalyzed by Iron-Based Materials: A Review. *J. Environ. Sci.* **2016**, *39*, 97–109.
- (180) Villa, K.; Parmar, J.; Vilela, D.; Sánchez, S. Core–Shell Microspheres for the Ultrafast Degradation of Estrogen Hormone at Neutral PH. *RSC Adv.* **2018**, *8* (11), 5840–5847.

## Resumen en español

El escaso suministro de agua limpia y el aumento de la contaminación del agua son desafíos globales clave para la sostenibilidad del agua, sobre todo teniendo en cuenta que gran parte del agua residual generada por la actividad agrícola e industrial humana no se trata. Los materiales y sistemas nanotecnológicos han surgido como nuevas herramientas para mejorar la eficiencia del tratamiento de aguas. Entre ellos, los micromotores autopropulsados han mostrado varias características ventajosas. Los micromotores son sistemas de propulsión autónoma que utilizan energía química presente en su entorno o pueden también ser propulsados a través de campos de fuerzas aplicadas externamente. Varios diseños, composición de materiales y mecanismos de propulsión se han sido reportados en el campo de los micromotores. En los últimos años, demostraron muchas aplicaciones de prueba de concepto en campos como la biomedicina, la detección y la remediación ambiental. Entre ellos, principalmente los micromotores propulsados por burbujas, los cuales se mueven debido a la generación y liberación de burbujas de gas de su superficie, se utilizan como una herramienta para aplicaciones de remediación de aguas. Esto se debe a la eficacia añadida de la transferencia de masa a la microescala, que se origina a partir de su movimiento y el movimiento de las burbujas liberadas. La micromezcla tiene una influencia importante en la cinética aparente de las reacciones químicas rápidas, en las que la velocidad de la reacción a menudo está limitada por la difusión. Además, la estructura de los micromotores se puede modificar para dirigirse a una amplia variedad de contaminantes, según los requerimientos. Los micromotores que sintetizamos durante el trabajo de investigación para esta tesis pueden eliminar contaminantes orgánicos y metales pesados, así como exhibir actividad anti bactericida.

Estudiamos micromotores de hierro/platino (Fe/Pt) por su reutilización, efecto de tamaños, su comportamiento durante su movimiento y propiedades catalíticas. Estos micromotores se fabricaron mediante enrollamiento espontáneo de nanomembranas de hierro y platino, depositadas en los patrones prefabricados definidos en una capa

sacrificial fotorresistente. La relajación de la tensión interna presente en las nanomembranas, tras el ataque de la capa de sacrificio, condujo al enrollamiento de las membranas en estructuras tubulares de micromotores. La capa de hierro presente como superficie externa de estos micromotores puede degradar los contaminantes orgánicos a través de la reacción tipo Fenton y la capa interna de platino actúa como el motor, siendo el catalizador que descompone el peróxido de hidrógeno en oxígeno para generar una propulsión por burbujas. Observamos que los micromotores Fe / Pt pueden nadar continuamente durante horas y pueden almacenarse durante semanas antes de volver a ser usados, sin que esto repercuta de manera significativa en su actividad. Se pueden extraer fácilmente del agua después del proceso de limpieza debido a sus propiedades magnéticas (Figura 1A). Los resultados de nuestros experimentos sobre el análisis de superficie de micromotores, estudio de nanoindentación y liberación de hierro sugirieron que los micromotores Fe / Pt actúan como un catalizador heterogéneo debido a las especies de óxido de hierro generadas in situ en la superficie, sin lixiviación de alta concentración de hierro en los medios.

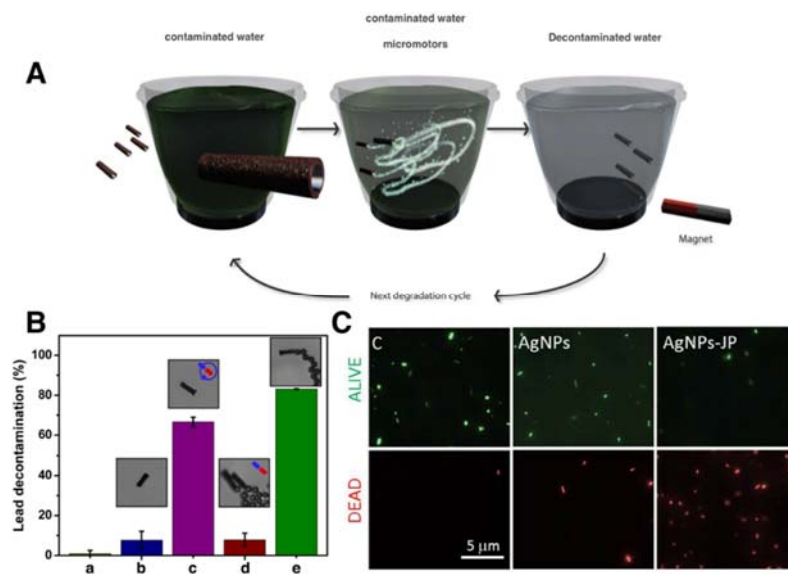


**Figura 1. Eliminación de contaminantes usando micromotores.** (A) Degradación de contaminantes orgánicos a través de una reacción de oxidación avanzada similar a Fenton

catalizada por micromotores de hierro / platino reutilizables. (B) Eliminación mejorada de contaminantes de metales pesados (es decir, iones de plomo) por adsorción en micromotores basados en óxido de grafeno para nado. (C) matar y eliminar bacterias (es decir, *E. coli*) usando micromotores bactericidas que contienen magnesio revestidos con nanopartículas de oro y plata.

Desarrollamos micromotores basados en óxido de grafeno (micromotores GOx) para la eliminación de metales pesados que consisten en multicapas nanométricas de óxido de grafeno, níquel y platino. Estos micromotores pueden capturar, transferir y eliminar metales pesados (es decir, plomo) del agua contaminada. Los micromotores GOx se sintetizan mediante electrodeposiciones de capas de óxido de grafeno, níquel y platino, los cuales son electroreducidos en la parte interior de membranas de policarbonato porosas. Los micromotores tubulares se obtienen después de disolver la plantilla de policarbonato. La capa externa de óxido de grafeno captura el plomo en su superficie, y la capa interna de platino proporciona autopropulsión en presencia de peróxido de hidrógeno, mientras que la capa intermedia de níquel permite el control magnético externo de los micromotores. Observamos que los micromotores móviles GOx pueden eliminar el plomo hasta 10 veces más que los micromotores GOx no móviles (Figura 1B), limpiando el plomo en agua de 1000 ppb a menos de 50 ppb en menos de 60 min. Estos micromotores se pueden reciclar y reutilizar después de la recuperación del metal pesado de su superficie mediante el uso de medios ácidos para la desorción de iones metálicos. Hemos demostrado el control de su movimiento y direccionalidad en un sistema microfluídico como prueba de concepto.

Diseñamos también micromotores tipo Janus decorados con nanopartículas de plata (AgNP) para la desinfección y eliminación de la bacteria *Escherichia coli* (*E. coli*) en agua contaminada. Los micromotores Janus se sintetizaron recubriendo un lado de una micro-partícula de magnesio con capas de hierro y oro, las cuales posteriormente se funcionalizaron con AgNP. El magnesio presente en los micromotores funciona no sólo como estructura principal para conseguir una forma esférica, sino también como fuente de propulsión mediante la producción de

burbujas de hidrógeno al entrar en contacto con el agua. La capa interna de hierro proporciona la funcionalidad requerida para el posterior control magnético externo, mientras que la capa de oro externa decorada con AgNPs promueve la adhesión de bacterias y dota de propiedades bactericidas a los micromotores (Figure 1C).

En nuestro esfuerzo por desarrollar micromotores multifuncionales y métodos de síntesis escalables, desarrollamos dos tipos de micromotores. (i) Micromotores mesoporosos basados en sílice con una capa de dióxido de manganeso ( $\text{MnO}_2$ ) en la superficie interna y recubiertos con nanopartículas  $\gamma\text{-Fe}_2\text{O}_3$  (micromotores  $\text{FeSiMnOx}$ ). Estos micromotores pueden eliminar contaminantes orgánicos y metales pesados, y se sintetizan utilizando solo métodos químicos asistidos por un molde (por ejemplo, una membrana porosa). La degradación de los contaminantes orgánicos se logra gracias a las reacciones fotocatalíticas similares a Fenton catalizadas por nanopartículas de  $\text{Fe}_2\text{O}_3$  y su propulsión es impulsada por  $\text{MnO}_2$  y en parte por nanopartículas de  $\text{Fe}_2\text{O}_3$ , que catalizan la descomposición del peróxido de hidrógeno. Estos micromotores son uno de los micromotores más rápidos que utilizan un catalizador metálico no noble para la descomposición de  $\text{H}_2\text{O}_2$ . (ii) Los micromotores de ferrita de cobalto (micromotores CFO) fueron sintetizados sin necesidad de utilizar ningún molde. Están formados por nanopartículas de ferrita de cobalto agregadas, que actúan como catalizadores para la propulsión y para reacciones tipo Fenton. Medimos cualitativamente la generación de radicales hidroxilos por micromotores CFO y estudiamos el efecto de los tensioactivos sobre la eficiencia de degradación de los micromotores CFO.

Esperamos que la síntesis de micromotores a través de métodos relativamente fáciles empuje la implementación de micromotores en soluciones comercialmente prácticas para el tratamiento del agua. Asimismo, se deben realizar esfuerzos futuros para un mayor desarrollo de métodos de síntesis escalables y el uso de materiales eficientes y económicos en la estructura de micromotores. En general, nuestros resultados muestran que los micromotores autopropulsados

multifuncionales tienen el potencial de convertirse en una herramienta efectiva para la limpieza de aguas en el futuro.